STUDIA UNIVERSITATIS
BABEŞ-BOLYAI

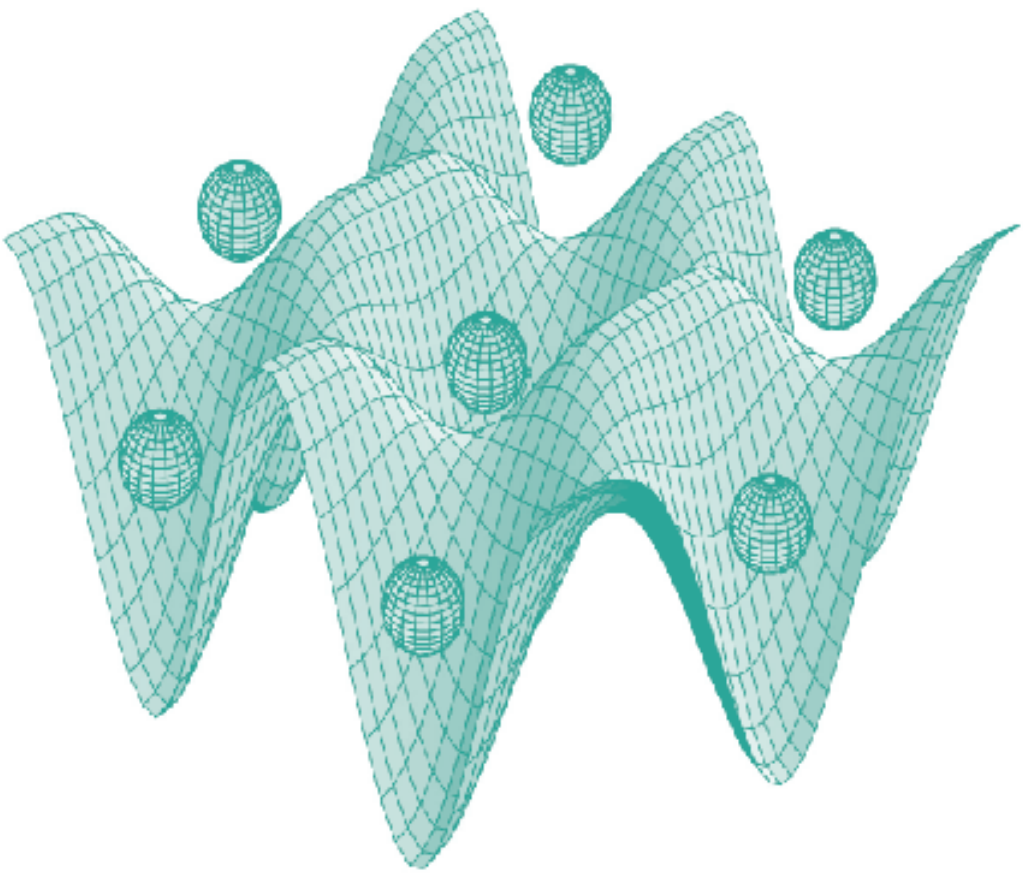

PHYSICA

1/2012

YEAR **Volume 57 (LVII) 2012**
MONTH **JUNE**
ISSUE **1**

S T U D I A
UNIVERSITATIS BABEŞ–BOLYAI
PHYSICA
1

ANNIVERSARY ISSUE DEDICATED TO PROFESSOR IOAN ARDELEAN

Desktop Editing Office: 51st B.P. Hasdeu, Cluj-Napoca, Romania, Phone + 40 264-40.53.52

CUPRINS – CONTENT – SOMMAIRE – INHALT

STUDIA UBB PHYSICA, Vol. 57(LVII), 1, 2012, pp. 3 - 4
(RECOMMENDED CITATION)

Foreword

Professor Ioan Ardelean was born in 1942, Crăciuneşti, Maramureş.

He graduated Babes-Bolyai University Cluj-Napoca in 1966. Between 1967-1968 he worked as physicist at Machine building plant in Reşiţa. Since 1968 Prof. Ardelean worked at Babes-Bolyai University first as physicist (1968-1975) and later as scientific researcher (1976-1994). Prof. Ioan Ardelean earned his PhD in Physics in 1979 under the guidance of Prof. I. Pop. Between 1995-2011 he held the position of professor at the Faculty of Physics, Department of Matter Physics and Advanced Technologies.

His activity continued and in 2012 he was granted the title of honorific consulting professor.

Understanding the importance of modern directions in material science, he introduced new courses. Professor Ioan Ardelean presented the following courses: Physics and Technology of Oxide Materials, Amorphous Solid State, Magnetism and Magnetic Materials, Nondestructive Defectoscopy, Crystalline, Vitreous and Oxide Electronic Materials. In the framework of Master of Science Programme he has been involved in teaching advanced courses in Ceramics and Vitreous Materials, Special Oxide Glasses, Complements on Solid State Physics, Modern Technologies for Synthesis Advanced Materials. At doctoral school presented lectures on Modern Methods in Solid State Physics. In the position of PhD coordinator he supervised 25 doctoral theses in the field.

The scientific activities of Prof. Ioan Ardelean were directed particularly on synthesis and study of structure and physical properties of new oxide materials with vitreous structure and the study of vitro-ceramics with 3d transition elements.

Prof. Ioan Ardelean obtained significant scientific results concerning synthesis of materials, physical properties of new materials, the nature of magnetic interactions, local environment effects, the connection between local structure and magnetic properties, spin and ordered structures in glasses and ceramics. The scientific results of Prof. Ioan Ardelean were published in 550 papers, 253 being in ISI quoted journals. Around 40 papers were published in Proceeding of International Conferences. The scientific results of Prof. Ioan Ardelean are frequently cited in literature (around 1000 citations), particularly for their rigorous presentation of new results related to the properties of new materials.

His theoretical and experimental researches as well as his pedagogic experience were fructified into a series of books focusing on physical properties of solid state. Professor Ioan Ardelean published also four scientific books, and six book frequently used by the students in area of their courses. These are remarkable for their accuracy and clarity as well as scientific level.

Professor Ioan Ardelean is member of many Romanian (Romanian Physical Society, Romanian Society of Biomaterials, Romanian Society of Magnetic Materials, Romanian Society of Materials) and international (European Physical Society, Balkan Physical Society, International Society of Crystallography) scientific societies of physics and materials physics.

He has done extensive research in management sciences, holding several management positions in university (Chairman of Research Council at the University "Babes-Bolyai" between the years 1998-2006) and in different national structures (member of CNCSIS committee no. 1 Mathematics and Natural Sciences; Expert at CNCSIS and ARACIS). Professor Ioan Ardelean has extensive experience in the management of national / international scientific projects, gaining over 60 scientific contracts and grants.

He was Director of Physics Institute Ioan Ursu and Deputy Director of the Centre of Excellence "Science and Technology of Advanced Materials" certified by Romanian scientific authority CNCSIS in 2006.

Professor Ioan Ardelean is member of the Editorial Board of some Romanian Journals (*Studia Universitatis Babeș-Bolyai Physica*, *Annals of the Timișoara University* and *Oradea University-Series Physics*) and Reader to a series of international scientific journals such as: *Materials Chemistry and Physics, Journal of Applied Physics, Physica Status Solidi, Physics and Chemistry of Glasses, Applied Physics Letters, Physica B, Modern Physics Letters B,* etc.

Professor Ioan Ardelean has been awarded by Romanian Academy, University Babes-Bolyai (9 diploma and professor emeritus in 2012), University of Oradea (Doctor Honoris Causa). He was involved in scientific programs with University of Aveiro (Portugal), University Wurzburg, J. Gutenberg University Mainz (Germany), University Tokai (Japan) and Technical University Wien (Austria). He was invited to sustain plenary presentations at many national and international meetings and conferences.

Today, at seventy years old, Prof. Ioan Ardelean is surrounded by researchers which continue his scientific activity.

Professor Aurel POP, Ph.D.
Dean, Faculty of Physics, Babes-Bolyai University

STUDIA UBB PHYSICA, Vol. 57(LVII), 1, 2012, pp. 5 - 14
(RECOMMENDED CITATION)

XPS STUDY OF METHEMOGLOBIN ADSORPTION ONTO GLUTARALDEHYDE FUNCTIONALIZED BIOACTIVE GLASS AT DIFFERENT IONIC STRENGTHS

ZS. BENYEY[1], E. VANEA[1], C. GRUIAN, V. SIMON[1, *]

ABSTRACT. In this study, the surface sensitive spectroscopic method X-ray photoelectron spectroscopy (XPS) was applied to obtain information on methemoglobin adsorption onto sol-gel derived 45S5 bioactive glass surface in solutions of different salt concentrations. The adsorption behavior was also followed by Brunauer-Emmitt-Teller (BET) surface area and pore volume evaluation, before and after protein adsorption. It was found that a low salt concentration has a beneficial effect on the methemoglobin adsorption.

Keywords: biomaterials; surface functionalization; protein adsorption; XPS.

INTRODUCTION

When biomaterials interact with a biological medium, they immediately come in contact with the proteins of the biological fluids. This interaction with the proteins further determines the material affinity for the biological medium [1, 2]. The need to understand protein adsorption to solid surfaces increases with the need for developing new biomaterials. The adsorption process is very common; almost all surfaces get relatively fast coated with proteins when they interact with a biological medium. But despite being common the process is by far not trivial or completely understood. Protein adsorption on biomaterials is influenced by a great variety of factors and differs for each type of protein and substrate [3, 4]. One of the influencing factors of protein adsorption is the ionic concentration of the liquid the protein is dissolved in [5], and implicitly the ionic strength. This is why it is important to study the behavior and the amount of protein adsorbed onto the surface of a sol-gel derived 45S5 bioactive glass. The biocompatibility of this bioactive glass led to an extensively investigation for its use as implant materials to repair and replace diseased or damaged bone [6].

[1] Babes-Bolyai University, Faculty of Physics & Institute of Interdisciplinary Research in Bio-Nano-Sciences, Cluj-Napoca, Romania
* Corresponding author: viosimon@phys.ubbcluj.ro

Horse methemoglobin is considered as a model protein in this study, because it is mostly similar to human methemoglobin, but is more common [7]. Hemoglobin is found in the red blood cells, having a role in wound closing and healing [8]. As structure and properties horse methemoglobin is a medium sized (around 66 KDa) globular protein incorporating four polypeptide subunits. Each of these subunits incorporates a heme group. The heme group's metallo organic center contains iron, coordinated by four N ligands, in its oxidized Fe^{3+} state [9, 10].

To further foster the protein adsorption, the bioactive glass surface was silanized with 3-aminopropyl-triethoxysilane (APTS) and afterwards treated with glutaraldehyde (GA) as protein coupling agent [11, 12].

Protein adsorption is driven by an entropy gain arising from the release of surface adsorbed water molecules and salt ions as well as from structural rearrangements inside the protein [13]. This means that the ionic concentration of the solution can determine what part of the proteins interacts with the substrate. It was shown that this also influences damping distance of the electric potential [14]. With higher ion concentrations, the length of the electrostatic interactions gets shorter. This has a positive effect on protein adsorption only if the protein and the substrate have the same charge, otherwise the protein adsorption is somewhat hindered [15].

Considering all the above presented issues, this study aims to investigate adsorption of horse methemoglobin on glutaraldehyde functionalized bioactive glass, in solutions with two different ionic strengths: low (10 mM of NaCl) and high (500 mM of NaCl).

For this purpose X-ray photoelectron spectroscopy was used to determine the quantity of protein adsorbed onto the bioactive glass surface. X-ray photoelectron spectroscopy (XPS) is a suitable technique for such investigations, because of its capability to accurately measure the elemental composition of the top 10 nm of any surface. The strength of XPS consists on its ability to quantify the surface elemental composition, being well suited to evaluate the adsorption of proteins and other biomolecules. This is due to a number of factors including the range of elements that can be analyzed and due to the fact that the analyzed depth is larger than the thickness of most adsorbed proteins, enabling the detection simultaneously of both the substrate and protein [16].

Single point Brunauer-Emmett-Teller (BET) surface area and pore volume were also determined in order to evaluate the protein adsorption.

MATERIALS AND METHODS

The bioactive glass matrix used in this study was prepared using the sol-gel method, mimicking the molar concentration of the original Bioglass® 45S5 [6]: 45% SiO_2, 24.5% Na_2O, 24.5% CaO and 6% P_2O_5. The precursors used were tetraethoxysilane (TEOS),

$Ca(NO_3)_2.4H_2O$, $(NH_4)_2HPO_4$ and Na_2CO_3. After gelation the sample was aged at room temperature for 30 days, followed by a heat treatment at 310^oC for 1 hour to remove solvents and organic components left in the matrix.

The as prepared bioactive glass was surface functionalized according to [11, 12]. First the silanization process was carried out by immersing the glass in aqueous solution (0.45 mol/L) of 3-aminopropyl-triethoxysilane (APTS) for four hours. The pH of the solution was adjusted to 8 (using HCl 1M) and the temperature was kept at 80 ºC. After silanization the sample was washed with deionized water, than functionalized with glutaraldehyde (GA) [$CH_2(CH_2CHO)_2$] (1mol/L) for one hour, followed by rinsing in deionized water.

For protein adsorption GA functionalized bioactive glass powder was immersed in horse methemoglobin solution for 4 hours. The horse methemoglobin solution was prepared with phosphate-buffered saline solution (pH 7.4, 2 mg/ml) using two different salt concentrations (10 mM NaCl and 500 mM NaCl). For both salt concentrations the amount of horse methemoglobin in the solution was of 25 mg/ml.

To remove the unattached protein from the surface, the samples were washed three times in buffer solutions and then lyophilized.

XPS measurements were carried out on a SPECS PHOIBOS 150 MCD system equipped with a monochromatic Al-Kα X-ray source (1486.6 eV), a hemispherical analyzer, a charge neutralization device and a multichannel detector. The samples were immobilized on the sample holder with help of a double sided carbon tape. During the experiment the X-ray source operated with a power of 250 W, while the pressure in the analysis chamber was kept in the range of 10^{-9}- 10^{-10} mbar.

The binding energy scale was referenced to C 1s (C–C and C-H) peak at 284.6 eV. Elemental composition was determined from survey spectra for each sample, over a binding energy range of 0 – 1200 eV. The average of ten survey scans was acquired at pass energy of 100 eV and resolution of 1 eV/step. High-resolution spectra of C 1s, N 1s and O 1s were average of twenty scans acquired with constant pass energy of 30 eV and 0.05 eV/step resolution.

The CasaXPS software was used to carry out the data analysis. Shirley background was selected for all curve-fitting, along with the Gaussian/Lorentzian product form (70% Gaussian and 30% Lorentzian). Quantitative analysis of the spectral data (surface chemical compositions, expressed as relative atomic concentration (at %)) was obtained from the peak-area ratios.

The surface area and pore volume were determined by measuring nitrogen adsorption/desorption at 77 K with Qsurf Series M1 surface area analyser, on the basis of Brunauer, Emmet and Teller (BET) method. The measurements were performed using one point BET method with 30% N_2, 70% He gas mixtures. The reported values are averages of three distinct measurements.

RESULTS AND DISCUSSION

To evaluate the adsorption of methemoglobin on the bioactive glass surface, XPS measurements were performed on the as prepared bioactive glass (BG), after functionalization with glutaraldehyde (BG-GA) and after immersion in protein solution in low and high salt environment.

Using the survey spectra (Fig. 1) the elemental composition of the top 10 nm of the samples can be precisely determined. The as prepared bioactive glass contains oxygen, silicon, calcium, phosphorus, sodium as expected from the preparation and also small amounts of carbon. The carbon appears on all surfaces exposed to air and can be used to calibrate the charge compensation of the samples [17]. The atomic concentration was calculated with CasaXPS software. From these data (**Error! Reference source not found.**) the evolution of the elements on the surface of the glass can be followed.

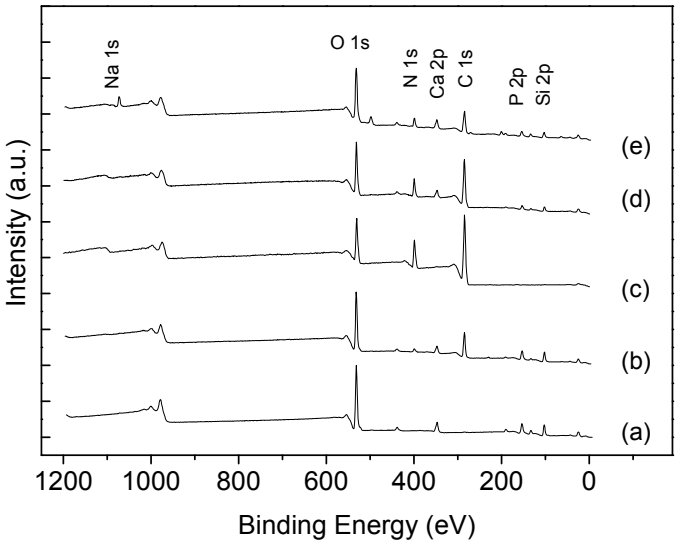

Fig. 1. XPS survey spectra of BG (a), BG with GA (b), lyophilized horse methemoglobin (c), and BG-GA after immersion in protein solution with 10 mM NaCl (d) and 500 mM NaCl (e) respectively.

After silanization and GA treatment, the concentration of the carbon peak increases significantly, also a small nitrogen concentration appears. These are consequentially accompanied by a small decrease in the other components of the BG, meaning that a successful surface modification was achieved. Methemoglobin contains mostly carbon, oxygen and nitrogen [Table 1]. The high concentration of

carbon and nitrogen in both samples immersed in methemoglobin solution proves protein attachment, fact supported by the close C to N ratios in both samples compared to the lyophilized protein. Although from both salt concentrations protein attachment is evident, the effect is more pronounced for the buffer with lower salt content. Both carbon and nitrogen peaks appear almost twice in concentration compared to the samples obtained from high salt solution.

Table 1. Elemental composition of bioactive glass before and after surface modification with methemoglobin in 10 mM and in 500 mM NaCl buffer solutions

Sample	Elemental composition (at %)								
	Si	**Ca**	**P**	**Na**	**C**	**O**	**N**	**S**	**Cl**
BG	32.6	5	2.3	1.4	5.6	53	-	-	-
BG-GA	18	2.9	1.5	-	40.5	33.6	3.4	-	-
MetHb	-	-	-	-	64.8	18.4	16.7	0.1	-
BG-GA MetHb (10 mM NaCl)	5.8	2.1	1	0.1	58.1	21.4	11.5	-	-
BG-GA MetHb (500 mM NaCl)	10	3.5	3	2.6	38	33	7.7	-	2

The high resolution spectra give information about the chemical states of the elements. The C 1s core-level spectra (Fig. 2) recorded for protein loaded samples, compared to the bare sample evidence more intense and asymmetric peaks, confirming the presence of new types of carbon bonds [18, 19]. The deconvolution (Fig. 3) of the carbon core level spectra presents for the non-functionalized substrate one peak at 284.6 eV, corresponding to C-C and C-H bonds for the contamination from the air, as well as one at 289 eV representing the carbon from carbonate that still remains from the precursors in the bioactive glass. For the functionalized and protein covered samples the peak from the carbonates disappears. Additional components arise for the protein containing samples as well as in the protein itself: at 287.5 eV and 285.6 eV attributed to NH–CHR–CO and –C(=O)–NH2 respectively. Because of the charging effect the peaks have a shoulder at lower binding energies (around 281 eV).

The N 1s core level spectrum (Fig. 4) shows no nitrogen present in the bare bioactive glass matrix. The N1s deconvolutions (Fig. 5) of the protein containing samples show two main components around 400 eV and 397.8 eV, which can be attributed to nitrogen in organic matrixes, related to C-N bonds [20]. A smaller peak appears around 395 eV, which appears for protein itself and protein adsorbed from low salt solution.

The O 1s core level spectra (Fig. 6) show a tendency to shift to lower binding energies in the protein containing samples on the account of the oxygen recorded for pure methemoglobin. The peaks around 533 eV correspond to the oxide matrix, while the oxygen present in proteins is situated around 531 eV, suggesting thus that for the protein loaded sample the O 1s photoelectrons correspond significantly to peptidic oxygen from proteins [21].

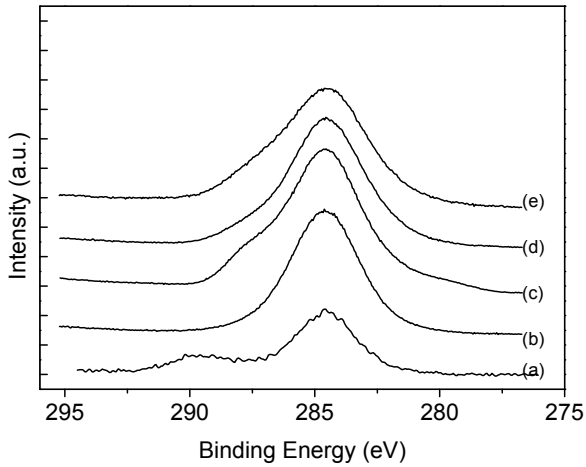

Fig. 2. XPS C 1s high resolution spectra of BG (a), BG with GA (b), lyophilized horse methemoglobin (c), and of BG-GA after immersion in protein solution with 10 mM NaCl (d) and 500 mM NaCl (e) respectively.

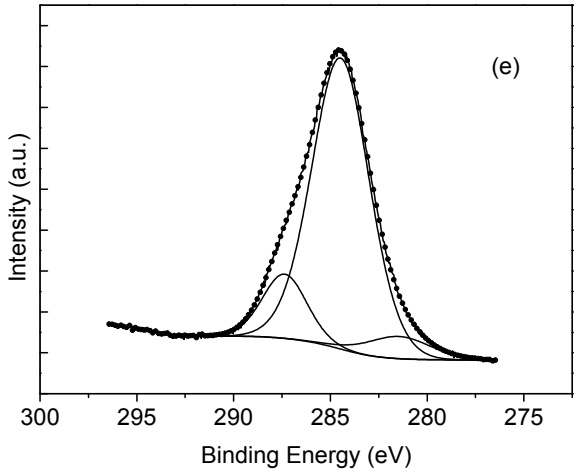

Fig. 3. Deconvolution of XPS C 1s high resolution spectra of BG (a), BG with GA (b), lyophilized horse methemoglobin (c), and of BG-GA after immersion in protein solution with 10 mM NaCl (d) and 500 mM NaCl (e) respectively.

The BET specific surface area and pore volumes are listed in Table 2. The BET surface area of bare bioactive glass was 98.6 m^2g^{-1}, 106 m^2g^{-1} for the GA functionalized BG; the surface area increased significantly after protein adsorption to 133.2 m^2g^{-1} and 121.7 m^2g^{-1} for the samples prepared with low and high salt content, respectively.

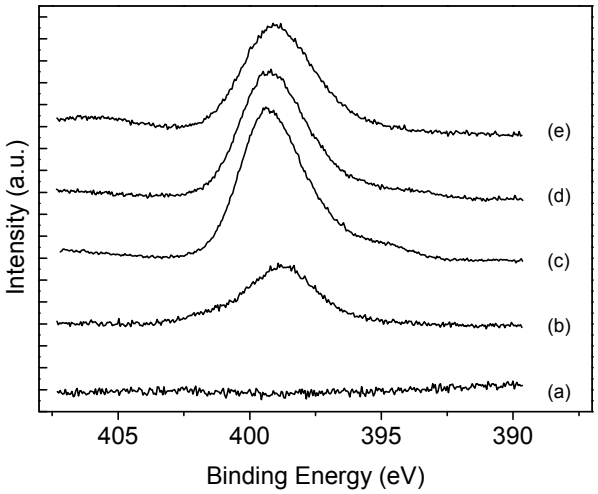

Fig. 4. XPS N 1s high resolution spectra of BG (a), BG with GA (b), lyophilized horse methemoglobin (c), and of BG-GA after immersion in protein solution with 10 mM NaCl (d) and 500 mM NaCl (e) respectively.

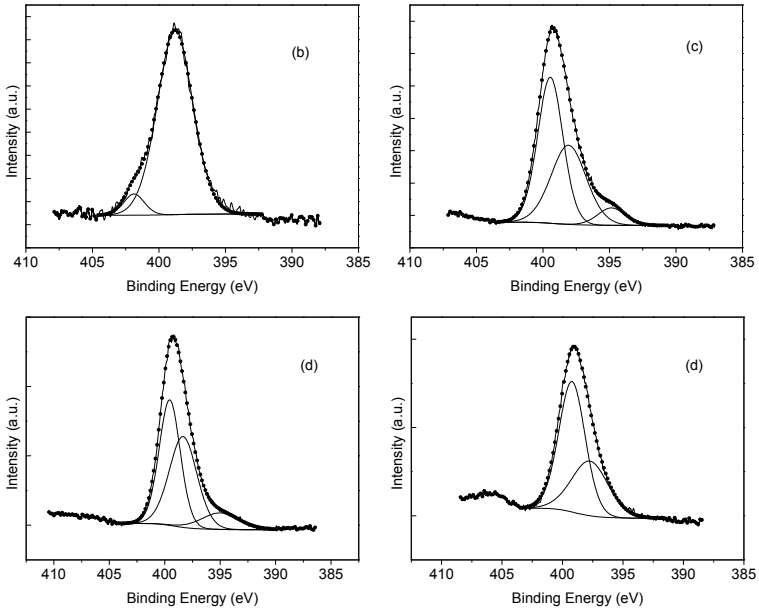

Fig. 5. Deconvolution of XPS N 1s high resolution spectra of BG with GA (b), lyophilized horse methemoglobin (c), and BG-GA after immersion in protein solution with 10 mM NaCl (d) and 500 mM NaCl (e) respectively.

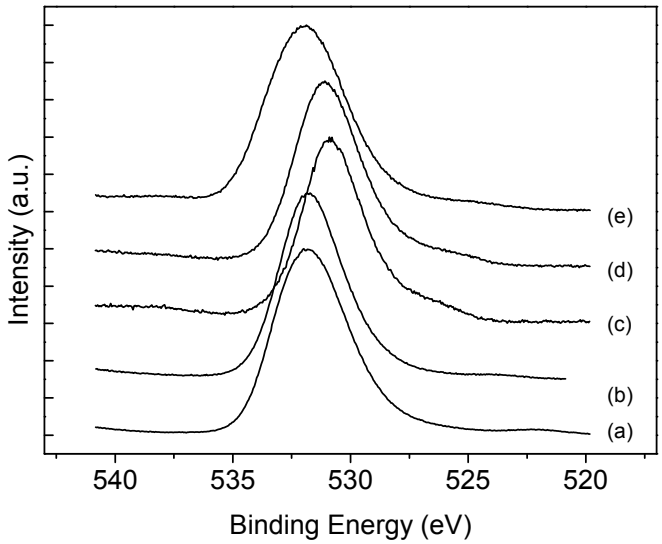

Fig. 6. XPS O 1s high resolution spectra of BG (a), BG with GA (b), lyophilized horse methemoglobin (c), and of BG-GA after immersion in protein solution with 10 mM NaCl (d) and 500 mM NaCl (e) respectively.

Table 2. Specific surface area and pore volume recorded before and after methemoglobin adsorption.

Sample	BET surface area (m^2g^{-1})	Pore volume (ml/g)
BG	98.6	0.46
BG-GA	106.0	0.38
BG GA MetHb (10 mM NaCl)	133.2	0.22
BG GA MetHb (500 mM NaCl)	121.7	0.23

The pore volume decreases once the surface is loaded, this effect being even more pronounced for the sample immersed in low salt protein rich solution. Specific surface area and pore volume measurements suggest a larger amount of adsorbed protein in the case of low salt concentration, which expose a larger surface and enhance the surface porosity.

CONCLUSIONS

XPS has shown to be well suited for quantifying adsorbed hemoglobin on the bioactive glass sample. The XPS experimental data clearly show that both the high and low salt concentration buffer can result in horse methemoglobin adsorption

onto glutaraldehyde functionalized bioactive glass. However, it was found that the lower salt concentration had a beneficial effect on the adsorption. Both carbon and nitrogen peaks from samples immersed in the lower salt buffer solution are almost double of those that were immersed in high salt concentration buffer. These results are supported also by the values obtained for specific surface area and pore volume before and after methemoglobin adsorption on bioactive glass surface.

ACKNOWLEDGMENTS

E. Vanea would like to thank for the financial support provided by the project POSDRU/21/1.5/G/36154 –"Performant doctoral program for the development of highly qualified human resources in the interdisciplinary scientific research".

Zs. Benyey acknowledges the financial support from POSDRU/107/1.5/S/ 76841 project – "Modern Doctoral Studies: Internationalization and Interdisciplinary".

REFERENCES

[1]. Xie J, Riley C, Chittur K, J Biomed Mater Res 57 (2001) 357-65.

[2]. Berry CC, Adams S, Curtis G, J Phys D: Appl Phys 36 (2003) 198-206.

[3]. Oscarsson S, J. Chromatogr 699 (1997) 117-131.

[4]. Michael R, Dorinel V, Stefan S, Adv Coll Interf Sci 162 (2011) 87–106.

[5]. Vendruscolo M, Dobson CM, Nature, 449 (2007) 555.

[6]. Hench LL, West JK, Chem Rev 90 (1990) 33-72.

[7]. Baldwin JM, J Mol Biol 136 (1980) 103-128.

[8]. Costa AM, Mavropoulos E, Mello A, Key Eng Mater 494 (2012) 504-507.

[9]. Cai S, Singh BR, Biochem 43 (2004) 2541-2549.

[10]. Levitt M, Greer J, J Mol Biol 114 (1977) 181-293.

[11]. Dong A, Randolph TW, Carpenter JF, J Biol Chem 275 (2000) 27689–27693.

[12]. Chen QZ, Rezwan K, Françon V, Armitage D, Nazhat SN, Jones FH, Boccaccini AR, Acta Biomater 3 (2007) 551-562.

[13]. Norde W, Biopolymers at interfaces, in Surfactant Science Series, New York (1998) Vol. 75, 27-54.

[14]. Israelachvili J, Intermolecular and surface forces, 2nd Ed. ed.; Academic Press (1992).

[15]. Jones KL, O'Melia CR, J Membr Sci, 165 (2000) 31-46.

[16]. Sally L. McArthur, Surf Interface Anal 38 (2006) 1380–1385.

[17]. Michel R, Pasche S, Textor M, Castner DG, Langmuir, 21 (2005) 12327–12332.

[18]. Browne MM, Lubarsky GV, Davidson MR, Bradley RH, Surf Sci 553 (2004) 155–167.

[19]. Serra J, Gonzalez P, Liste S, Serra C, Chiussi S, Leon B, Perez-Amour M, Ylanen HO, M. Hupa, J Non-Cryst Solids 332 (2003) 20–27.

[20]. Serro AP, Gispert MP, Martins MCL, Brogueira P, Colaco R, Saramago B, J Biomed Mater Res; 78A (2006) 581-589.

[21]. Vanea E, Simon V, Appl Surf Sci, 257 (2011) 2346-2352.

STUDIA UBB PHYSICA, Vol. 57(LVII), 1, 2012, pp. 15 - 24
(RECOMMENDED CITATION)

STRUCTURAL AND ELECTRICAL PROPERTIES OF $In_{5.5+x}Sb_{1.5-3x}W_{2x}O_{12}$ SOLID SOLUTION

L. BIZO[1]

ABSTRACT. $In_{5.5+x}Sb_{1.5-3x}W_{2x}O_{12}$ solid solution ($0 \le x \le 0.45$) has been synthesized and studied from point of view of structural and electrical properties. The latter exhibits an ordered oxygen-deficient fluorite structure with an ordered cationic distribution. The $\rho = f(T)$ curves corresponding to the the four compositions less rich in W(VI) - $x \le 0.20$ - shows a resistivity slightly affected by increasing concentration of W(VI). From composition $x = 0.25$ a significant increase in electrical resistivity was observed, namely one order of magnitude for $x = 0.25$ compared to $x = 0.2$ ($\rho_T = 2 \times 10^{-1}$ and 2×10^{-2} Ω.cm, respectively). The presence of antimony, even in low concentration, allows to obtain high levels of electrical conductivity.

Keywords: transparent conductors, solid solution, indium rich oxides, X-ray diffraction, Rietveld refinement, electrical properties.

INTRODUCTION

Transparent conducting oxides (TCOs) have become an important topic in the field of optoelectronics and numerous investigations have been carried out recently on these materials, in order to discover new n-type or p-type transparent conductors [1-3]. Besides the famous ITO indium-rich oxide, which crystallizes with the bixbyite structure, another oxide was identified for the composition $In_4Sn_3O_{12}$ with M_7O_{12} type structure. Introduction of antimony in the M_7O_{12} structure and the existence of a positive effect on the electrical conductivity have been previously demonstrated. Sb^{5+} can be introduced without difficulty into M_7O_{12} structure of $In_4Sn_3O_{12}$ until the formation of the antimonate $In_{5.5}Sb_{1.5}O_{12}$ [4]. We know that the stability of M_7O_{12} structure of $In_{4+x}Sn_{3-2x}Sb_xO_{12}$ solid solution is strongly affected as the antimony content increases, leading in fact to its transformation into a bixbyite type structure. The electrical conductivity appears to benefit from the introduction of Sb^{5+}. Taking into account the existence of tungstate In_6WO_{12} previously reported [5-7] which shows the significant stabilizing effect due to the introduction of W^{6+} in a M_7O_{12} structure, $In_{5.5+x}Sb_{1.5-3x}W_{2x}O_{12}$ solid solution were prepared [8]. The aim of the paper is to study this solid solution from point of view of structural and electrical properties.

[1] Babes-Bolyai University, Faculty of Chemistry and Chemical Engineering, 11 Arany Janos Str., 400084 Cluj-Napoca, Romania, lbizo@chem.ubbcluj.ro

EXPERIMENTAL

The different compositions ($0 \leq x \leq 0.45$) studied in the series $In_{5.5+x}Sb_{1.5-3x}W_{2x}O_{12}$ were prepared by solid state reactions from mixtures of pure In_2O_3, SnO_2, WO_3 and Sb_2O_3 in alumina crucibles heated in air. At first the mixtures were heated at at 600 °C in order to ensure the full oxidation of Sb(III) into Sb(V) and than succesive 12h annealings followed by air quenching were performed. After each annealing step, air quenching and regrinding was performed. Laboratory XRPD data for phase identification and Rietveld refinement were collected using a Panalytical X'Pert diffractometer (CoKa1 radiation) equipped with an X'Celerator detector. The laboratory powder data were refined with the Fullprof programme [9]. Resistivity data were measured with the four probe method on pellets sintered in air at 1300 °C using a PPMS (Physical Properties Measurements System) device.

RESULTS AND DISCUSSION

Homogeneity range and structure calculation

According to the experimental procedure described above, new compositions of solid solution $In_{4+2x}Sn_{3-3x}W_xO_{12}$ were obtained. Their diffractogrammes are all very similar and also isotypic to $In_4Sn_3O_{12}$ confirming the existence of a complete homogeneity range of this solid solution ($0 \leq x \leq 0.45$). In the case of $In_{5.5+x}Sb_{1.5-3x}W_{2x}O_{12}$ solid solution the presence of Sb^{5+} greatly facilitates the formation of M_7O_{12} structure to the point that a final temperature of 1200 °C is sufficient to obtain a total reaction of precursors. Since this temperature is not enough to ensure a correct sintering of samples prepared for electrical resistivity measurements, we have decide to systematically perform an additional annealing at 1300 °C.

Table 1. Cell parameters (Å) and volume (Å^3) of the hexagonal cell of solid solution $In_{5,5+x}Sb_{1,5-3x}W_{2x}O_{12}$ after 1200 et 1300°C.

Comp. x	0	0,05	0.1	0.15	0.2	0.25
a(Å) 1200°C	9.4545(2)	9.4533(2)	9.4571(2)	9.4595(2)	9.4627(2)	9.4637(2)
1300°C	9.4545(2)	9.4582(2)	9.46(2)	9.4629(2)	9.4645(2)	9.4686(2)
c(Å) 1200°C	8.921(2)	8.9247(2)	8.9315(2)	8.9328(2)	8.9355(2)	8.9361(2)
1300°C	8.921(2)	8.9249(2)	8.9287(2)	8.9304(2)	8.9307(2)	8.9345(2)
V(Å^3) 1200°C	691.1	691.21	692.3	692.75	693.43	693.62
1300°C	691.1	691.94	692.5	693.06	693.32	694.21
Comp. x	0.3	0.35	0.4	0.45	0.5	-
a(Å) 1200°C	9.4655(3)	9.4678(2)	9.4733(2)	9.4751(2)	9.483(2)	-
1300°C	9.4695(2)	9.4736(2)	9.4717(2)	9.4761(2)	9.483(2)	-
c(Å) 1200°C	8.9373(3)	8.9362(2)	8.9396(2)	8.9408(2)	8.9428(2)	-
1300°C	8.9346(2)	8.9375(2)	8.9354(2)	8.9395(2)	8.9428(2)	-
V(Å^3) 1200°C	693.98	694.23	695.3	695.66	696.97	-
1300°C	694.35	695.18	694.75	695.7	696.97	-

Table 1 presents the values of cell parameters, *a* and *c*, and volume *V* of the hexagonal cell obtained after XRPD refinement and Figure 1 shows the variation of these data in terms of x.

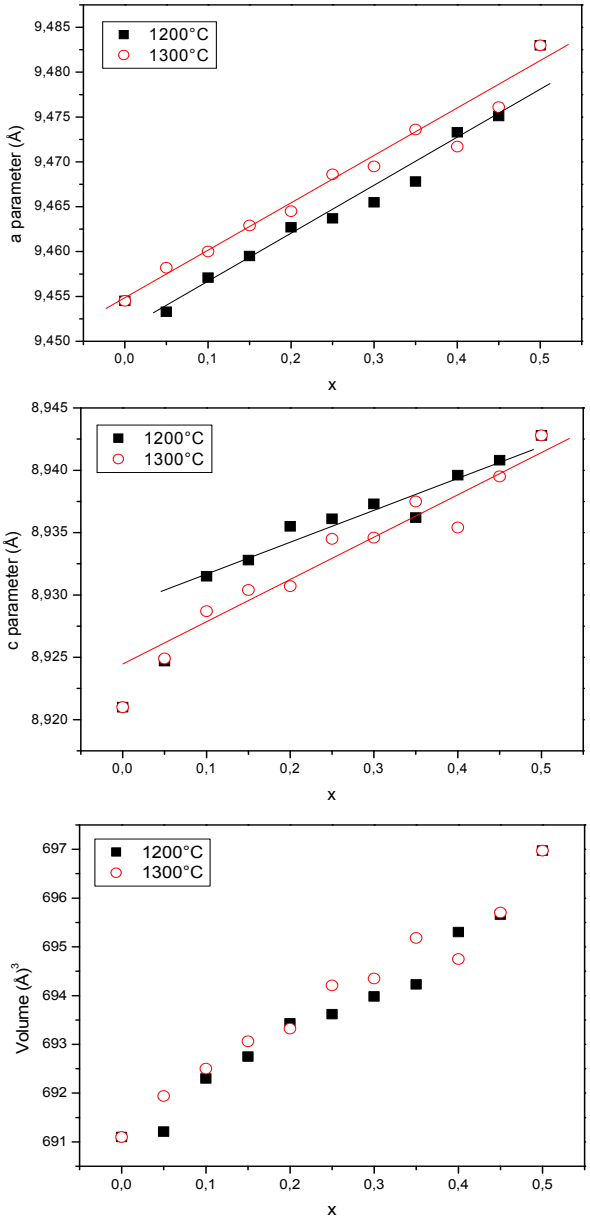

Figure 1. Variation of the hexagonal cell constants in the solid solution $In_{5.5+x}Sb_{1.5-3x}W_{2x}O_{12}$ after heating at 1200°C (black) and 1300°C(red).

An isotropic and overall linear property was observed (Figure 1). Regarding the influence of final preparation temperature, beyond perhaps atypical fluctuations observed for some compositions, the treatment at 1300°C results in sistematic and sligth increase of the value of *a* (0.005 Å) compensated by a decrease of the *c* value, which fades as x increases. The absence of significant variations in the cell volume, especially for values of x < 0.25 where the two-phase nature of the product obtained at 1300 °C has been established, were observed. The overall increase of volume *V* is well correlated with the variation of mean cationic radius during the coupled substitution $3Sb^{5+} \rightarrow 2W^{6+} + In^{3+}$, from 0.60 to 0.67 Å.

Comparison of diffractogrames for samples prepared at 1200 °C and 1300 °C (Figure 2) results into the following observation: for the richest antimony compostitions (x ≤ 0.25) an extra phase is formed at 1300 °C. This phase was identified to a bixbyite type oxide, eventually doped with antimony and (or) tungsten, which is in a significant concentration, more than 5%.

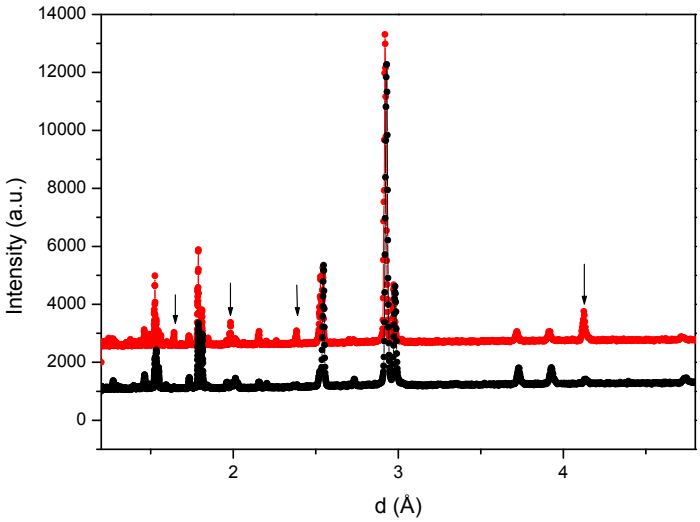

Figure 2. Comparison of diffractograms for x = 0.15 composition of $In_{5,5+x}Sb_{1,5-3x}W_{2x}O_{12}$ solid solution after heating at 1200°C (lower) and 1300°C (upper). The arrows shows the extra phase positions after heating at 1300°C.

Structure calculations have been performed by Rietveld analysis of diffractogrammes in a series of nine compositions. We have considered the two final treatment conditions conducting to two separate sets of structure calculations, corresponding to 1200_°C and 1300 °C, respectively. The structural model of $In_4Sn_3O_{12}$ was used [10], S.G. $R\bar{3}$ with two sets of cationic positions 3(a) and 18(f) and three sets of oxygen 18(f), in the corresponding hexagonal cell. The structural results

including atomic positions and cations distributions gives informations regarding the cationic distribution in the 3(a) and 18(f) sites. The best structure calculations always correspond to total preferential localization of tungsten in octahedral 3(a) site, and cation which accompany W^{+6} in this site is Sb^{5+}. As expected on the basis of its larger size, In^{3+} occupies the distorted sevenfold coordinated site 18(f). For all compositions convergence was obtained without difficulty, leading to values of R_B always close to 5.

For samples prepared at 1200 ˚C the presence of In_2O_3 was detected throughout this series of calculations. The results shows a percentage of bixbyite extra phase still below 4% (wt.). Thus the temperature of 1200 °C must be probably the limit temperature of stability in air of this solid solution. A further treatment at 1300 ˚C, necessary in order to prepare the pellets for electrical measurements, reveal the formation of a significant amount of bixbyite phase on a large compositions range ($x < 0.35$). We give as an example the detailed results for the composition $x = 0.2$, $In_{5,7}W_{0,4}Sb_{0,9}O_{12}$, in terms of atomic parameters (Table 2) and calculated and observed diffractograms (Figure 3 and Figure 4).

Table 2. Atomic parameters of composition $In_{5.7}\ Sb_{0.9}W_{0.4}O_{12}$ after heating at 1200 °C and 1300 °C.

Formula	$In_{5.7}Sb_{0.9}W_{0.4}O_{12}$ 1200˚C	$In_{5.7}Sb_{0.9}W_{0.4}O_{12}$ 1300˚C
Cationic site 3(a) 60 % Sb and 40% W	B $(Å)^2$ 0.86(7)	B($Å^2$) 0.86(7)
Cationic site 18(f) 95% In and 5 % Sb	x 0.2509(2) y 0.2148(2) z 0.3530(3) B$(Å)^2$ 0.73(3)	x 0.2509(3) y 0.21524(2) z 0.35295(3) B($Å^2$) 0.41(4)
O_1 site 18(f)	x 0.1866(14) y 0.1554(26) z 0.1142(13) B $(Å)^2$ 2.4(3)	x 0.1838(19) y 0.1581(30) z 0.1127(15) B($Å^2$) 1.9(3)
O_2 site 18(f)	x 0.1995(20) y 0.9742(21) z 0.3958(11) B$(Å)^2$ 2.4(2)	x 0.1968(25) y 0.9778(26) z 0.3884(15) B($Å^2$) 1.9(3)
Reliability factors	$R_B = 2.7$ $R_p = 11.4$ $R_{wp} = 12.3$	$R_B = 4.6$ $R_p = 13.4$ $R_{wp} = 14.0$

The results of structure calculations for all compositions prepared at 1300°C are presented nextly in conection with electrical resistivity measurements. As deduced from the examination of corresponding diffractogrammes, the presence of an bixbyite extra phase type is certain. First of all this data is critical in order to understand

the results of electrical measurements and to receive more information on the comparison of different aspects concerning both crystal chemistry and TCO properties of bixbyite and M_7O_{12} type oxides.

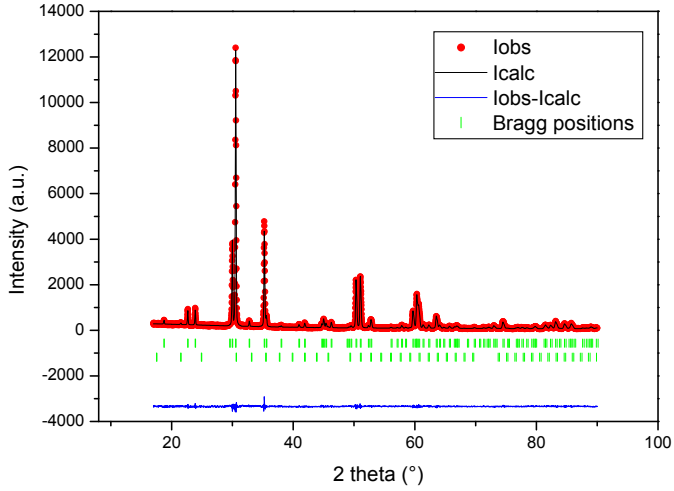

Figure 3. Observed (dots), calculated (lines) and difference XRPD pattern of $In_{5.7}Sb_{0.9}W_{0.4}O_{12}$ treated at 1200°C. Vertical bars indicate the positions of the reflections of the title phase (upper) and In_2O_3 (lower).

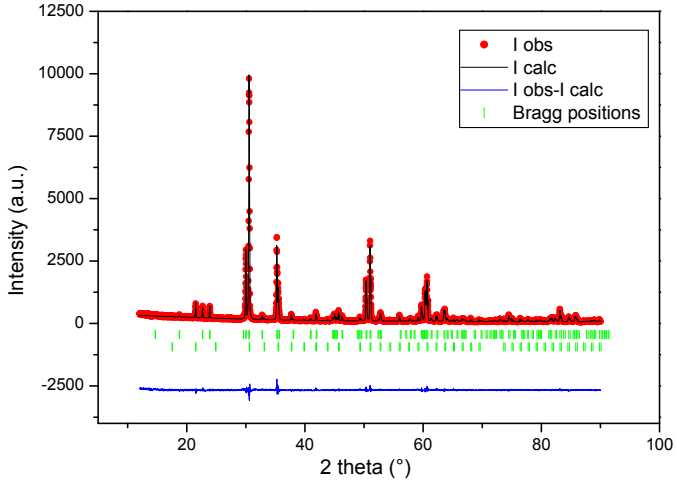

Figure 4. Observed (dots), calculated (lines) and difference XRPD pattern of $In_{5.7}Sb_{0.9}$ $W_{0.4}O_{12}$ treated at 1300°C. Vertical bars indicate the positions of the reflections of the title phase (upper) and In_2O_3 (lower) [8].

The crucial point which shows the difference between the two heating temperatures is concerned by the percentage of the M_7O_{12} and bixbyite phases, respectively. Table 3 presents the results of calculation of these percentages for the nine compositions after heating at 1300°C. There is no doubt that the M_7O_{12} phase is always in a large majority, but is accompanied by a significant amount of bixbyite phase, around 30% for the richest antimony compositions ($x \leq 0.15$). The percentage of bixbyite is at least 15% for $0.2 < x < 0.3$ compositions. Only poor antimony compositions ($x = 0.40$ and $x = 0.45$) contain a small amount of bixbyite phase, around 5%.

Table 3. Percentage of M_7O_{12} and bixbyite phases in $In_{5.5+x}Sb_{1.5-3x}W_{2x}O_{12}$ solid solution after heating at 1300°C (the precision of percentage values is 1%).

Comp. x	0.05	0.1	0.15	0.2	0.25	0.3	0.35	0.4	0.45
M_7O_{12} 1300°C	73	71	68	83	85	86	91	94	95
Bixbyite 1300°C	27	29	32	17	15	14	9	6	5

Electrical measurements

We present here the results of electrical resistivity measurements carried out in the field of temperatures 5-320 K, on pellets treated at 1300 °C. Figure 5 includes the $\rho = f(T)$ curves of the nine compositions of $In_{5.5+x}Sb_{1.5-3x}W_{2x}O_{12}$ solid solution.

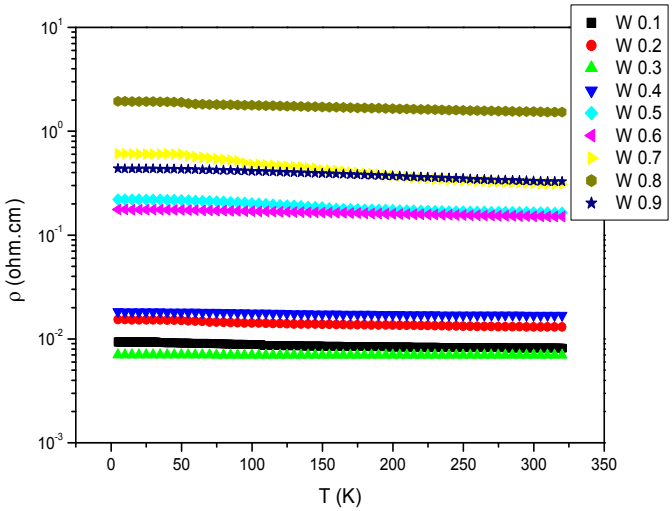

Figure 5. Electrical resistivity(Ω.cm) versus temperature(K) in $In_{5.5+x}Sb_{1.5-3x}W_{2x}O_{12}$ solid solution after heating at 1300°C [8].

The overall increase of electrical resistivity of the $In_{5,5+x}Sb_{1,5-3x}W_{2x}O_{12}$ solid solution as antimony content decreases, more specifically as Sb (V) is replaced by the pair 2/3 W(VI) + 1/3 In(III), takes place in two distinct steps corresponding to the following compositions range, $x \leq 0.20$ (W0, 4) and $x > 0.20$:

- compositions $x \leq 0.20$ (W0.4): $\rho = f(T)$ curves corresponding to the the four compositions less rich in W (VI) shows a resistivity slightly affected by the higher concentration in W (VI) . The value of ρ_T is close or less than 10^{-2} Ω.cm (in the range 8×10^{-3} - 2×10^{-2} Ω.cm, depending on x).

- compositions $x > 0.20$ (W0.4): a significant increase in electrical resistivity from the composition x = 0.25 (W0,5), namely one order of magnitude compared to x = 0.2 ($\rho_T = 2 \times 10^{-1}$ and 2×10^{-2} Ω.cm, respectively), was observed.

In order to establish if the increase of resistivity is due to the introduction of increasing amounts of tungsten, two samples of W doped In_2O_3, IWO 2% and IWO 3%, were prepared and their electrical resistivity were measured on pellets treated at 1300°C. Figure 6 shows an increasing resistivity values for IWO 3%, close to one order of magnitude if compared to IWO 2% and pure In_2O_3. There is no doubt that the introduction of W(VI) in $In_{5.5+x}Sb_{1.5-3x}W_{2x}O_{12}$ solid solution has a negative influence on the electrical conductivity. However, a permanent semi-metallic behaviour (Figure 6), including the highest levels of tungsten, is maintaining. Comparison of electrical resistivities in relation to the presence of Sb(V) in indium rich oxides is well illustrated in the case of electrical properties observed for IWO and $In_{5.5+x}Sb_{1.5-3x}W_{2x}O_{12}$ solid solution (Figure 7). We have grouped the $\rho = f(T)$ curves of IWO 2% and 3% compositions, as well as compositions x = 0.05 and x = 0.1 of the $In_{5.5+x}Sb_{1.5-3x}W_{2x}O_{12}$ solid solution which correspond to very close content of W(VI), 1.4 and 2.9%, respectively.

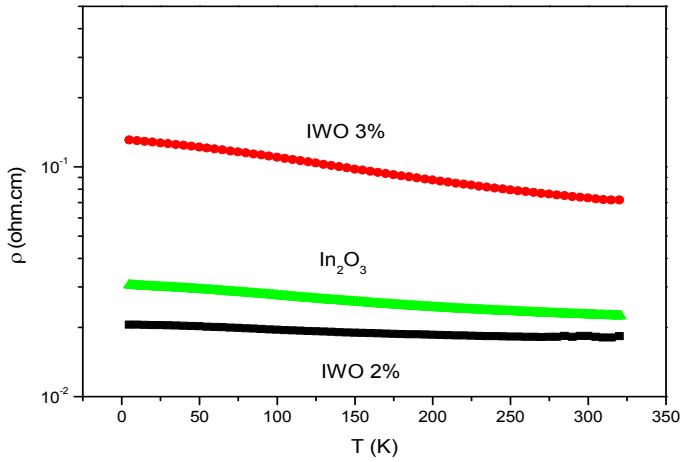

Figure 6. Electrical resistivity(Ω.cm) versus temperature (K) for IWO(2%), IWO(3%) and In_2O_3.

The degradation of the electrical conductivity due to the introduction of increasing amount of W(VI) differs significantly in relation to the presence of Sb(V): in the bixbyite structure, in the absence of Sb(V), the increasing of electrical resistivity is much higher than in the presence of Sb(V). The values of resistivity are at least one order of magnitude higher when the doping rate of tungsten in In_2O_3 is changing from 2 to 3%. A comparable increasing in the level of W(VI) in $In_{5.5+x}Sb_{1.5-3x}W_{2x}O_{12}$ solid solution translates into a very small increase of resistivity, not exceeding one tenth order of magnitude. Moreover the temperature dependence of IWO is practically semi-conducting instead of semi-metallic in $In_{5.5+x}Sb_{1.5-3x}W_{2x}O_{12}$ solid solution.

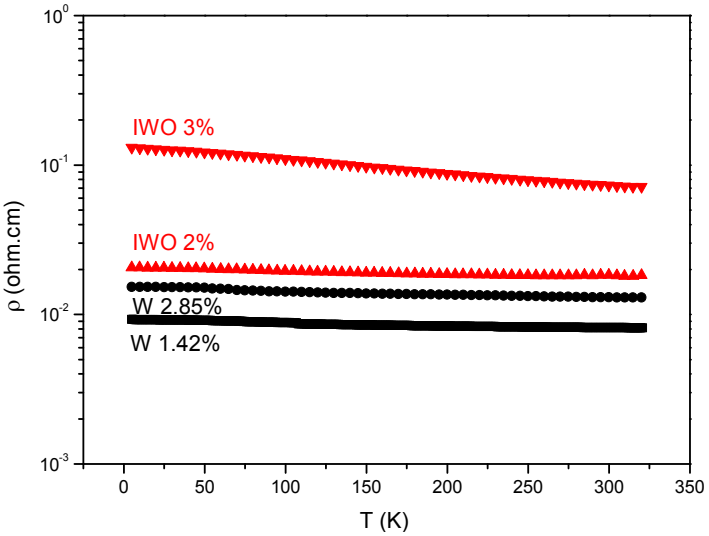

Figure 7. Electrical resistivity (Ω.cm) versus temperature (K) for IWO(2%), IWO(3%) and compositions x=0.05 (W1.42) and x=0.1(W2.85) of $In_{5.5+x}Sb_{1.5-3x}W_{2x}O_{12}$ solid solution.

CONCLUSIONS

$In_{5.5+x}Sb_{1.5-3x}W_{2x}O_{12}$ solid solution was studied from point of view of structural and electrical properties. The structural results shows an ordered cationic distribution. An overall increase of electrical resistivity of the $In_{5.5+x}Sb_{1.5-3x}W_{2x}O_{12}$ solid solution, as antimony content decreases, was observed. Regarding the introduction of W^{6+} in the presence of Sb^{5+} in $In_{5.5+x}Sb_{1.5-3x}W_{2x}O_{12}$ solid solution can be emphasized: presence of Sb^{5+}, even in low concentration, allows to obtain high conductivity levels and to minimize the induced insulating property of an "d" element with the maximum degree of oxidation, as W(VI). We estimate that the exercise of this physical property is directly dependent on the notable chemical property of Sb(V), namely his ability to a partial reduction in degree (III), always effective for treatments in air at 1300 ˚C.

ACKNOWLEDGMENTS

This work was possible with the financial support of the Sectoral Operational Programme for Human Resources Development 2007-2013, co-financed by the European Social Fund, under the project number POSDRU 89/1.5/S/60189 with the title „Postdoctoral Programs for Sustainable Development in a Knowledge Based Society”.

REFERENCES

[1] T. Minami, *MRS Bull.* 8, 38 (2000).

[2] A.J. Freeman, K.R. Poeppelmeier, T.O. Mason, R.P.H. Chang, T.J. Marks, *MRS Bull.* 8, 45 (2000).

[3] H. Kawazoe, H. Yanagi, K. Ueda, H. Hosono, *MRS Bull.* 8, 28 (2000).

[4] J. Choisnet, L. Bizo, R. Retoux, S. Hebert, B. Raveau, *J. Solid State Chem.* 177, 3748 (2004).

[5] T. Gaewdang, J.P. Chaminade, A. Garcia, C. Fouassier, M. Pouchard, P. Hagenmulle, B. Jacquier, *Mat. Letters* 18, 64 (1993).

[6] W.S. Dabney, N.E. Antolino, B.S. Luisi, A.P. Richard, D.D. Edwards, *Thin Solid Films* 41, 192 (2002).

[7] A.P. Richard, D.D. Edwards, *J. Solid State Chem.* 177, 2740 (2004).

[8] L. Bizo, C.I. Anghel, *Revue Roumaine de Chimie*, accepted, (2012).

[9] J. Rodriguez-Carvajal, T. Roisnel, ‘‘Line Broadening Analysis Using FullProf: Determination of Microstructural Properties’’, in: European Powder Diffraction Conference (EPDIC) 8, 2004, Vol. 443, pp 123–126.

[10] N. Nadaud, N. Lequeux, M. Nanot, J. Jove, T. Roisnel, *J. Solid State Chem.* 135, 140 (1998).

STUDIA UBB PHYSICA, Vol. 57(LVII), 1, 2012, pp. 25 - 33
(RECOMMENDED CITATION)

EMPLOYER MOBILITY NETWORK REVEALED FROM SOCIAL SECURITY DATA

N. DERZSY[1]

ABSTRACT The topology of employer networks is analyzed and reported. The networks are generated by the employee mobility and are constructed for 7 consecutive years (2001-2007) based on a social security data from Romania. The networks for each year in particular exhibit similar characteristics: scale-free degree distribution function, small average path length and high clustering coefficient. The scale-free nature of the degree distribution function validates the presence of preferential attachment between employers. The results prove that these economic networks are of Barabási-Albert network type.

Keywords: complex system, econophysics, scale-free network

INTRODUCTION

The end of the twentieth century's research condensed around the study of complex systems. Physicists got involved in research topics on complex systems from various fields, applying statistical physics methods and models aiming to understand their structure and dynamics. Many physicists chose to study systems of economic nature, like trade relations, economic transactions, wealth distributions, company interdependencies, etc. These researches lead to the development of econophysics, a new interdisciplinary research field. In this period of global financial crisis this topic is of great interest for everyone who is preoccupied with understanding the behaviour of these systems and wants to speculate their future outcome. Econophysics researchers try to understand their structure and governing mechanisms aiming to create models that can reproduce the topology and offer the possibility to analyze dynamical processes on these systems. This way the prediction and control of economic systems can be attained. The past few years of research offered numerous results enlightening characteristics that indicated that these systems are not random and unpredictable. This encouraged further investigation in economics by using statistical physics approach. Results revealed certain universal laws that these systems obey, irrespective of the geographical region the analyzed data come from.

[1] Babeş-Bolyai University, Faculty of Physics, 1 Kogălniceanu Str., 400084 Cluj-Napoca, Romania, noemi_derzsy@yahoo.com

Another interdisciplinary field that evolved in this period is the field of Random Networks. This research field studies complex systems through their underlying network structure. In the beginning period of network study it was believed that all complex systems are governed by randomness and have homogeneous structure with approximately same number of edges. Pál Erdős and Alfréd Rényi were the ones who created a network model based on this assumption [1]. Research made on real complex systems from various fields, for example biology [2], internet connection [3], scientific collaboration [4], revealed that this model does not reproduce realistically certain features of real networks. Their structure were not homogeneous, contrarily, it was observed that nodes organize themselves into highly connected groups, so called clusters. In real systems another phenomenon was observed that could not be reproduced by the Erdős-Rényi network model. Few nodes in the network possess a very high number of links (hubs), while the majority of the nodes have only a few connections. Barabási Albert-László and Albert Réka proposed a new network model aiming to complete the shortcoming of previous models. Their model defines a graph with scale-free degree distribution function, high clustering coefficient and small average path length. The key ingredient is the preferential attachment in network evolution, a phenomenon neglected in previous models. Based on the preferential attachment rule, hubs are generated in the system leading to heterogeneous structure. This scale-free model is also called after its founders Barabási-Albert network model [5]. So far, this model reproduces best the topology of real networks, whether it's an artificial or natural system and ensures the most accurate data on the study of the system's structure.

The Networks approach is helpful in understanding a complex system's structure and behaviour from various fields. It also had an important impact on research on economic systems, as well. Studies focusing on complex systems of economic nature are based on the analysis of the underlying network structure, for example the study of the underlying network structure of buyer-supplier relationships [6]. Even more, it is an efficient method for modelling processes on economical complex systems such as bargaining [7], agent trading [8-10] or stock market price prediction [11].

DATA AND AIMS

The goal of the present paper is to study a real social security database from Romania that contains information about a complex economic trade system from the Cluj district. The data set contains monthly information regarding employers with head-offices registered in Cluj district and their employees for years 2001-2007. This is a codified social security data set that offers unique possibility to study a real and complete complex economic system by analyzing its underlying network structure. The annual employee mobility networks are generated for each year (2001-2007) in particular and their topological properties are also studied. The data set results a

bipartite network from which two independent networks derive: employee network and employer network. The employee network can be constructed with nodes being the employees and a connection is established between two individuals whether they have worked for the same employer in the same period for at least one month. This network offers the possibility to study professional connections between individuals and study the information flow at workplace. A popular research topic is the study of virus spread, and since people spend most of their time at work interacting with colleagues, this network study could describe patterns that the virus spread follow based on contacts between fellow workers. Unfortunately, the database contains large firms with several hundreds of employers and companies with more than one working points. In case of large firms with hundreds of employees it is merely possible that they all know each other or to all get in contact with each other. Likewise, employees working at firms with several working points will probably not have the chance to interact at work, thus connecting such individuals to each other would not result a truthful network. Also, no data is available regarding working points within a firm, so a connection that would realistically reflect professional relationships between two employees cannot be made. The present paper focuses only on the study of the employer network. This network is constructed by nodes being the employers and a connection is established between two nodes whether an employee changes its workplace from one to the other. Thus the connection is realized by the mobility of employees, similarly to the Erasmus student mobility network study, where the connections between universities were established by the mobility of their students within the Erasmus framework [12]. While the employee network is a social network showing interaction of individuals at workplace, the employer network is of economic nature reflecting firms' connection through their workers. One can construct several networks from this large database depending on the direction of the links that are considered. The direction is established by the employee mobility: the source node is the previous employer and the target node is the individual's new employer. Based on the direction of the links, two kinds of directed networks can be built: one for the outgoing employees and another one for the incoming employees. Two undirected networks can also be constructed: one for the incoming and outgoing links, considering that there is a connection between two employers if there was at least one employee exchange in both directions, and the incoming or outgoing network, where a connection exists between two nodes if there was at least one employee exchange in any direction. For each of these networks the weighted version can be also constructed. The weight is given by the number of employee mobility between two employers. The present research focuses on the non-weighted version of the networks both for directed and non-directed links, considering that there is a connection between two employers if at least one employee was exchanged between them.

METHODS

The interest of the present paper is to study the topology of the employee mobility generated networks for each year in particular. The original database was transformed into adjacency (connectivity) matrixes correspondent for each year. The adjacency matrix is of size *NxN*, where *N* is the number of nodes the network has, in this case the number of employers in the certain year. The matrix elements' values can be 0 or 1 based on the following rule: a_{ij}=1, if between node *i* and *j* exists a link, a_{ij} = 0, if the two elements are not connected. After constructing the networks, their topological properties are analyzed: the degree distribution function's shape, average path length and clustering coefficient. These are the main characteristics that enlighten the structure of a network. The degree distribution function describes the probability that a randomly selected node in the network has degree *k*. Its calculation requires a simple algorithm that passes through each node and counts its row's non-zero elements in the matrix. Then the degree distribution is calculated by counting the number of vertices having degree *k*.

The average path length is the average of the smallest distances between two randomly selected nodes. Its calculation requires a more complex algorithm. In network study the breadth-first search algorithm is used to find the shortest distance from a node *i* to every other node in the network. The search starts from node *i*, knowing that the distance from itself is 0, then it finds all its neighbours that are by definition at distance 1, and their neighbours that must have distance 2, excluding the nodes already visited, and so on until all nodes in the network have been visited. This algorithm is the fastest and most efficient known for completing this calculation.

The clustering coefficient is defined as *C=(3xtriangles)/triples*, where the triangles is a set of three nodes, each of them connected with the other two, while the triples are three nodes with only one of the nodes being linked to the other two. The calculation of this measure requires a simple algorithm that in the first instance counts the number of links between each pair of neighbours of a node. Adding up the total number of these links for each node and dividing it with the number of connected triples, results the clustering coefficient. The number of connected triples is given by $\sum_i \frac{1}{2} k_i (k_i - 1)$ equation because a node *i* with degree k_i has $\frac{1}{2} k_i (k_i - 1)$ pairs of neighbors.

The above algorithms were implemented in C programming language in order to calculate these characteristics for the employer networks.

RESULTS AND DISCUSSION

The analysis of the degree distribution function is important in understanding the structure of a network. Its shape indicates whether the connections in the system are realized preferentially, randomly or follow a different pattern.

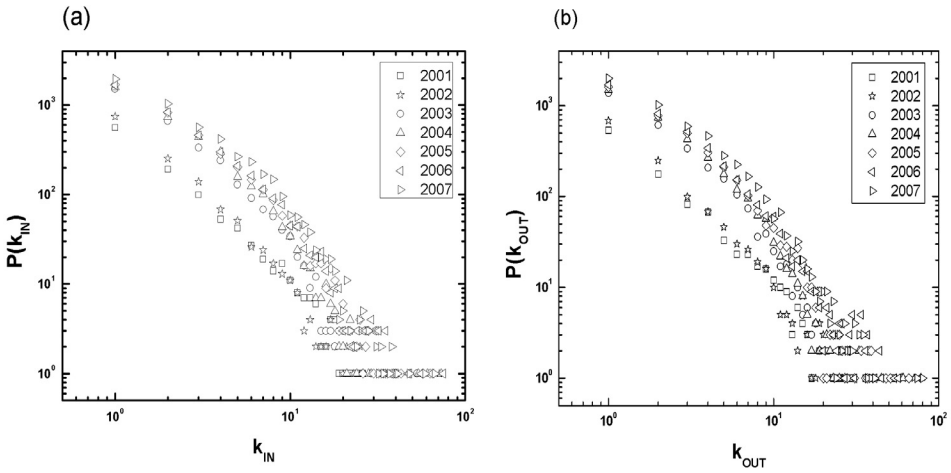

Fig. 1. (a) Cumulative in-degree distribution functions on log-log axis for years 2001-2007. **(b)** Cumulative out-degree distribution functions on log-log axis for years 2001-2007.

In many situations the visualization of the distribution function does not result a clear shape because of the statistical errors. In the case of large networks it is recommended the usage of the cumulative distribution function, defined as the integration of the degree distribution function. This way the noise is reduced in the function. In Figure 1 the cumulative degree distribution functions are plotted for all 7 years, for the directed networks, both for the incoming and outgoing degrees. In Figure 2 the cumulative degree distribution functions are plotted for the non-directed and non-weighted version of the networks.

Unfortunately, the plots still contain fluctuations, which need to be removed in order to obtain a clear shape of the degree distribution. Logarithmic binning is a method often used to produce smoother plots by reducing statistical errors. This is accomplished by varying the width of the bins in the plot in a way that each bin is a fixed multiple wider than the previous one. The number of samples that fall in the width of the bins must be normalized by dividing them with the bin width. The logarithmically binned degree distribution functions constructed in this manner are plotted in Figure 3 for the directed networks.

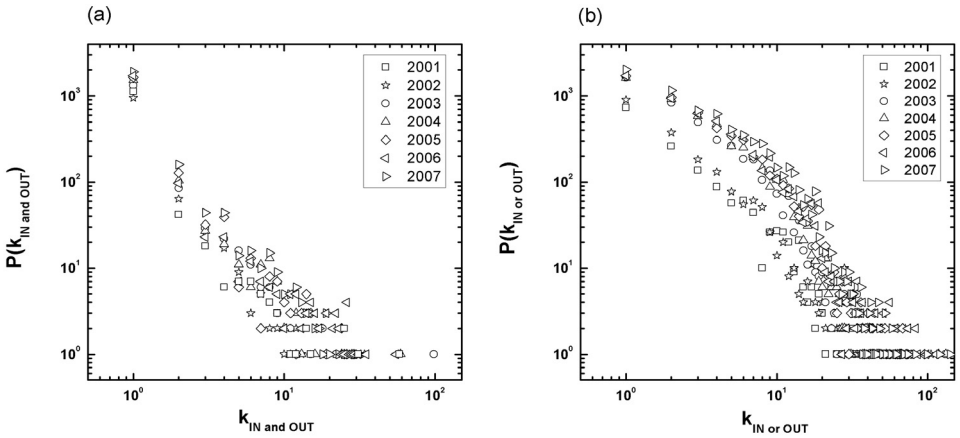

Fig. 2. (**a)** Cumulative in and out-degree distribution functions on log-log axis for years 2001-2007. **(b)** Cumulative in or out-degree distribution functions on log-log axis for years 2001-2007.

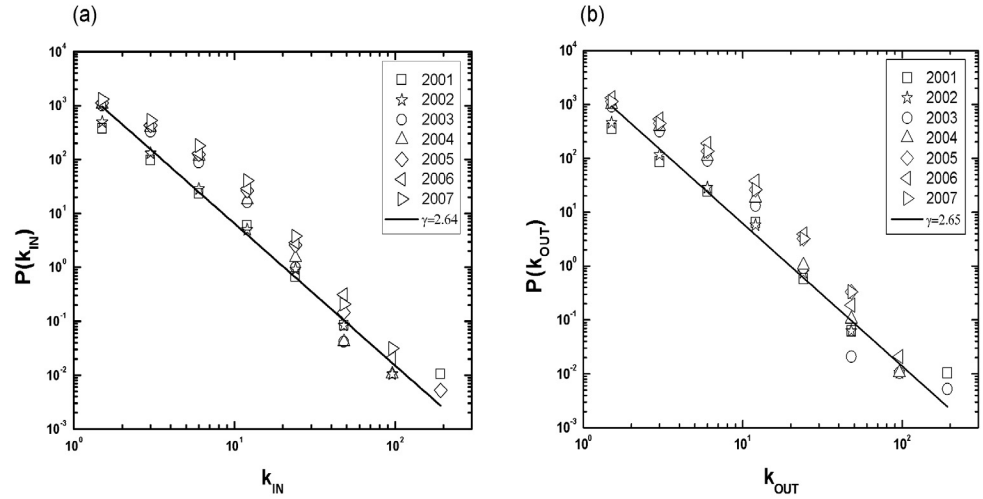

Fig. 3. (a) Degree distribution function constructed by a logarithmic bin for the incoming links on log-log axis. The thick continuous line is a power-law fit of the data points with exponent γ=2.64. **(b)** Degree distribution function constructed by a logarithmic bin for the outgoing links on log-log axis. The thick continuous line is a power-law fit of the data points with exponent γ=2.65.

Figure 4 represents the logarithmically binned degree distribution functions for the non-directed networks. The straight lines in the figures are power-law fits for the global values of the plots. Each year's logarithmically binned degree distribution functions have similar shapes, roughly straight line on log-log axis suggesting scale-free property. Each year's data points were fitted with a power-law function and

their exponents are presented in Table 1. These exponents for each year in particular exhibit values close to each other, thus a global fit of the data points can be a truthful approach to examine the shape of the functions.

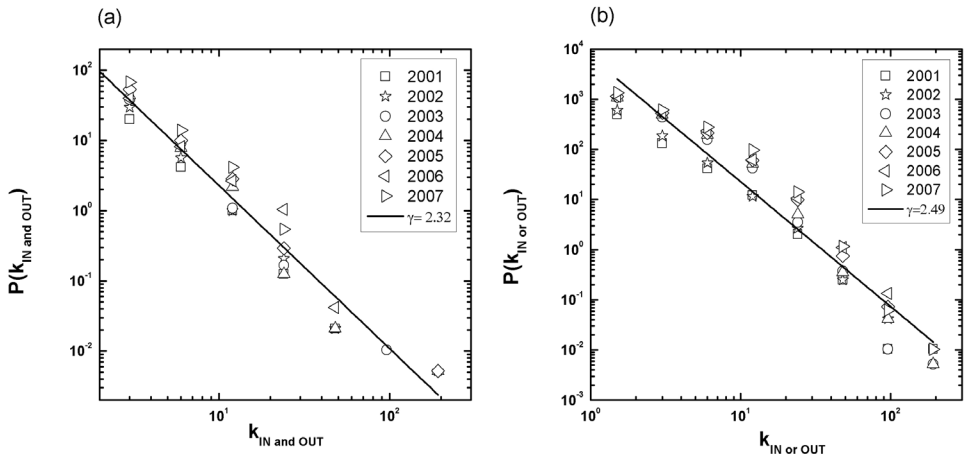

Fig. 4. (a) Degree distribution function constructed by a logarithmic bin for the in- and outgoing links on log-log axis. The thick continuous line is a power-law fit of the data points with exponent γ=2.32. **(b)** Degree distribution function constructed by a logarithmic bin for the in- or outgoing links on log-log axis. The thick continuous line is a power-law fit of the data points with exponent γ=2.49.

The scale-free nature of the degree distribution function suggests a preferential attachment rule between nodes. To further study the topology of these networks, the clustering coefficient and average path length were also analyzed, results being presented in Table 1. The small values obtained for the average path length suggest that the nodes in the system are closely connected, specific feature of social and economical networks. This characteristic allows high communication traffic, consequently a better information exchange in the system.

For each year, the obtained values of the clustering coefficient are relatively high, suggesting that employers are organized into densely connected clusters. This comes as a result of the employer's object of activity. Employees of a certain profession when changing workplace will likely go to a firm with the same object of activity. Unfortunately, the original database does not provide information regarding employer object of activity to test whether these employer communities indeed constituted based on this characteristic.

The degree distribution functions with power-law shape, small average path length and high clustering coefficient confirm that these economical networks, both for the directed and non-directed versions, are of Barabási-Albert network type.

These results are similar to previous research reports on several other networks of economical nature, like the network of company directors [13], land prices [14] and world exchange arrangements web [15]. The results exhibit scale-free characteristics suggesting the existence of preferential attachment in the network.

Table 1. The network characteristics for each year in particular. **N** denotes the network size (number of employers for each year). **γ** is the exponent of the power-law fit of the logarithmically binned degree distribution function, **ℓ** is the average path length in the incoming networks and **C** is the clustering coefficient. The indexes denote the network type (**in**-incoming, **out**-outgoing, **AND**-incoming and outgoing, **OR**-incoming or outgoing networks) that the measures refer to.

Year	N	γ_{in}	ℓ_{in}	C_{in}	γ_{out}	ℓ_{out}	C_{out}	γ_{AND}	ℓ_{AND}	C_{AND}	γ_{OR}	ℓ_{OR}	C_{OR}
2001	11370	2.27	3.28	0.24	2.28	2.71	0.31	2.49	3.15	0.13	2.52	2.44	0.23
2002	9646	2.60	4.11	0.27	2.61	3.42	0.30	2.17	3.44	0.22	2.40	2.87	0.32
2003	13476	2.87	3.06	0.22	2.81	3.32	0.28	2.43	3.28	0.28	2.32	2.56	0.28
2004	15465	2.95	2.98	0.29	2.86	2.98	0.27	2.31	3.22	0.15	2.74	3.04	0.31
2005	16770	2.65	2.75	0.28	2.35	3.10	0.32	2.24	3.32	0.17	2.64	3.21	0.26
2006	17464	2.63	2.88	0.32	2.73	3.63	0.29	2.28	3.31	0.21	2.33	2.68	0.28
2007	19568	2.65	3.42	0.28	2.35	3.22	0.25	2.27	3.56	0.19	2.19	3.02	0.29

CONCLUSIONS

Based on a social security data set some aspects of the complex economic trade system from Cluj district were studied. A special underlying network was generated for each year in particular, as directed and non-weighted networks and as non-directed and non-weighted networks and their topology was analyzed. The results suggested a degree distribution function with power-law shape, relatively small average path length and high clustering coefficients. These features suggest that these economic networks are of Barabási-Albert network type. The results are in agreement with previous studies made on economic networks that also exhibit scale-free properties. The scale-free nature of the networks confirms the presence of preferential attachment in the system. The measure that governs the preferential linking needs further investigation in the future. This study proved once again that the real complex systems of economic nature, are not driven by randomness and the scale-free network model describes well their characteristics.

ACKNOWLEDGMENTS

Financial support was provided by the Sectoral Operational Programme Human Resources Development, Contract POSDRU 6/1.5/S/3 Doctoral Studies: "Through science towards society".

REFERENCES

[1] P. Erdős, A. Rényi, *Publ. Math. Debrecen* 6 (1959).

[2] H. Jeong, B. Tombor, R. Albert, Z. N. Oltvai, A.-L. Barabási, *Nature* 407, 651655 (2000).

[3] M. Faloutsos, P. Faloutsos, C. Faloutsos, *Comput. Commun. Rev.* 29, 251-263 (1999).

[4] A.L. Barabási, H. Jeong, Z. Néda, E. Ravasz, A. Schubert, T. Vicsek, *Phys. A* 311, 590-614 (2002).

[5] R. Albert, A.-L. Barabási, *Reviews of Modern Physics* 74, 47-97 (2002).

[6] E. Atalaya, A. Hortaficsua, J. Roberts, C. Syversonc, *PNAS* 108, 5199-5202 (2011).

[7] T. Chakraborty, M. Kearns, S. Khanna, *ACM Conference on Electronic Commerce - EC*, July 6-10, 2009, California, USA, 159-168.

[8] R. Coelho, Z. Néda, J.J. Ramasco, M.A. Santos, *Phys. A* 353, 515-528 (2005).

[9] F. Schweitzer, G. Fagiolo, D. Sornette, F. Vega-Redondo, A. Vespignani, D.R. White, *Science*, 422-425 (2009).

[10] M. Ebert, W. Paul, arXiv:0905.4815v1 [q-fin.TR]

[11] B. Egeli, M. Ozturan, B. Badur, *3rd International Conference on Business*, June 18-21, 2003, Hawaii, 1-8.

[12] A. Derzsi, N. Derzsy, E. Káptalan, Z. Néda, *Phys. A* 390, 2601-2610 (2011).

[13] G.F. Davis, M. Joo, W. E. Baker, *Strateg. Organ.* 1, 301326 (2003).

[14] C. Andersson, A. Hellervik, K. Lindgren, A. Hagson, J. Tornberg, *Phys. Rev. E* 68, 036124 (2003).

[15] X. Li, Y.Y. Jin, G. Chen, *Phys. A* 343, 573 - 582 (2004).

STUDIA UBB PHYSICA, Vol. 57(LVII), 1, 2012, pp. 35 - 40
(RECOMMENDED CITATION)

COMPARATIVE STUDY BETWEEN PHOSPHATE GLASS SYSTEMS CONTAINING DIFFERENT RATIOS OF COOPER AND VANADIUM OXIDES

D.A. MAGDAS[1,*], N.S. VEDEANU[2], O. COZAR[3], I. ARDELEAN[3]

ABSTRACT. This work presents a comparative study of two phosphate glasses containing both cooper and vanadium oxides in different ratios investigated by IR spectroscopy. The investigated systems are: $x(CuO{\cdot}V_2O_5)$ $(100\text{-}x)[2P_2O_5{\cdot}PbO]$ and $x(CuO{\cdot}2V_2O_5)$ $(100\text{-}x)[2P_2O_5{\cdot}PbO]$ with $0 \le x \le 40$ % mol. The purpose of this study is to investigate the influence of vanadium oxide, added in different ratios in the phosphate network. It was observed that the depolymerization process that appears in the case of the glass system with higher vanadium content is significantly stronger than in the other studied system, showing that vanadium oxide has a strong modifier effect in the phosphate network.

Keywords: Phosphate glasses, vanadium oxide, cooper oxide, FT-IR

INTRODUCTION

Lead-based phosphate glasses are often used in practice especially in nuclear technology as absorbing screens for different radiation or as vitreous matrices used to embed and storing radioactive waste [1]. The introduction of lead in phosphate network increases glass durability by forming new Pb-O-P chemical bonds, but also suppressing the crystallization tendency to re-heating or cooling glass. Although lead oxide is not a vitreous network forming oxide on its own, it can be introduced in glasses together with traditional glass formers oxides like P_2O_5. It can be said that the structural role of PbO in many oxide glass is a special one because it can play a dual role as modifier, but also as former of the vitreous network [2].

On the other hand, V_2O_5 is one of the most studied and used oxide because it is also an un-conventional network former [3]. Lead vanadate phosphate glasses has

[1] National Institute for Research and Development of Isotopic and Molecular Technologies, 71–103 Donath, 400293 Cluj-Napoca, Romania, * alina.magdas@itim-cj.ro
[2] Biophysics Department, Iuliu Hatieganu University of Medicine and Pharmacy, 6 Pasteur Str., 400349 Cluj-Napoca, Romania
[3] Faculty of Physics, Babes-Bolyai University, 400084, Cluj-Napoca, Romania

received greater attention as a new brunch in semi-conducting glasses because of its wider glass forming region in the phase diagram, its possibility in threshold switching, memory switching and optical switching devices [4].

EXPERIMENTAL

The starting materials used in the present investigation were $(NH_4)_2HPO_4$, PbO, V_2O_5 and CuO of reagent grade purity. The samples were prepared by weighing suitable proportions of the components, powder mixing and mixture melting in sintered corundum crucibles at 1250^0C for 5 min. The mixtures were put into the furnace directly at the mentioned temperature. The obtained glass-samples were quenched by pouring the molten glass on a stainless steel plate.

The structure of the studied samples was investigated by means of XRD technique and no crystalline phases were detected (Figure 1).

The Fourier-Transform infrared (FT-IR) absorption spectra were recorded with a BRUKER IFS66/DSP spectrometer, at room temperature, in the range 400–4000 cm^{-1}, using the KBr pellet technique. In order to obtain good quality spectra, the samples were crushed in an agate mortar to obtain particles of micrometer size. This procedure was applied every time to fragments of bulk glass to avoid structural modifications due to ambient moisture.

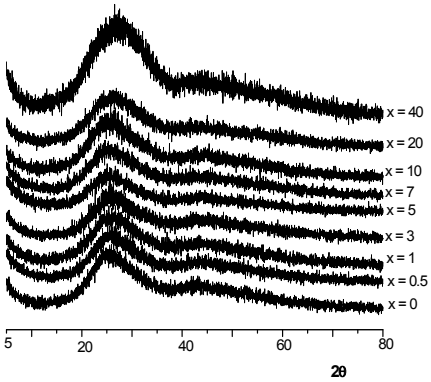

Figure 1. XRD spectra of $x(CuO{\cdot}2V_2O_5)(100\text{-}x)[2P_2O_5{\cdot}PbO]$ with $0 \le x \le 40$ % mol

RESULTS AND DISCUSSION

Two phosphate glass systems: $x(CuO{\cdot}V_2O_5)(100\text{-}x)[2P_2O_5{\cdot}PbO]$ and $x(CuO{\cdot}2V_2O_5)(100\text{-}x)[2P_2O_5{\cdot}PbO]$ with $0 \le x \le 40$ % mol were investigated in this work by mean of IR spectroscopy. The experimental IR spectra of these two systems are presented in Figs. 2 and 3 and the band assignments are given in Table 1.

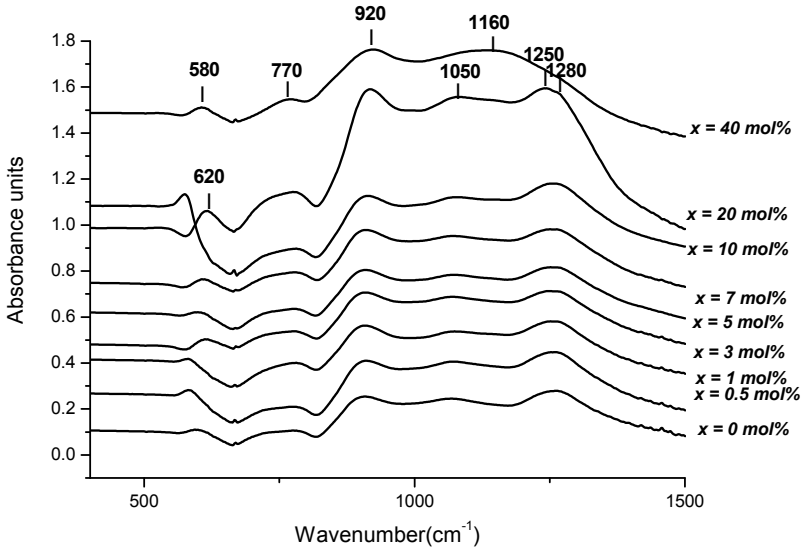

Figure 2. FT-IR spectra of $x(CuO{\cdot}V_2O_5)(100\text{-}x)[2P_2O_5{\cdot}PbO]$ glass system with $0 \le x \le 40$ % mol

At low concentrations of cooper and vanadium oxides, the specific bands of phosphate glasses dominate the spectra (Figs. 2 and 3). On the other hand, the presence of the PbO is observed in FT-IR spectra by the existence of Q^2, Q^1 and Q^0 groups. In the Q^n terminology, "n" represents the number of bridging oxygen atoms (BO) per PO_4 tetrahedron. The addition of PbO at the phosphate network results in the creation of non-bridging oxygen atoms at the expense of the bridging oxygen atoms [5].

Thus, the band around 580- 620 cm^{-1} is assigned to the bending mode of O-P-O in the Q^1 structure [6], while the broad band from 720 - 770 cm^{-1}, having two weak shoulders appears due to symmetric stretching vibrations of P-O-P rings [7-9] and symmetric modes of P-O-P bonds in Q^1 units [10]. The asymmetric stretching vibration of P-O-P bond is present in the spectra as a strong band around 920 cm^{-1} [8]. The band around 1050 cm^{-1} is assigned to asymmetric stretching vibration of PO_3^{2-} ionics group [11]. An increase in intensity of this band by addition of cooper and vanadium oxides is observed due to the replacemend of the long chains of metaphosphate- by small pyrophosphate units. The band from 1100 - 1160 cm^{-1} is attributed to symmetric stretching vibration of PO_4^{3-} tetrahedral groups (PO^- ionic group) [12, 13].

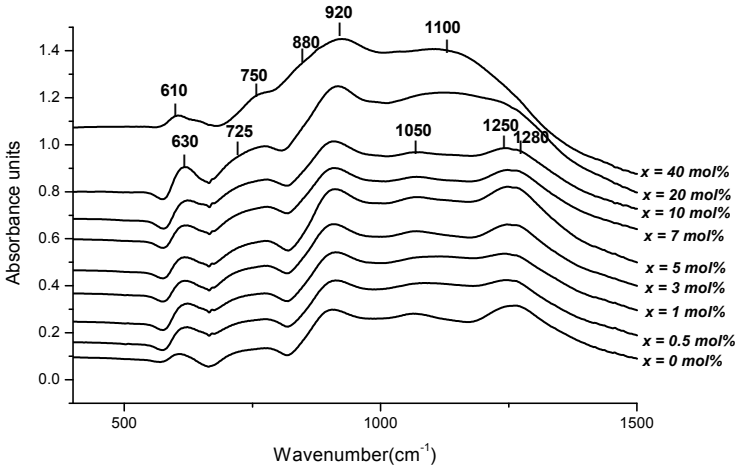

Figure 3. FT-IR spectra of $x(CuO{\cdot}2V_2O_5)(100\text{-}x)[2P_2O_5{\cdot}PbO]$ glass system with $0 \le x \le 40$ % mol

The broad band from 1250-1350 cm^{-1} have been attributed to the asymmetric and symmetric stretching vibrations of the double bonded oxygen (P=O) and to the symmetric stretching vibrations [14, 15]. At higher concentrations of cooper and vanadium oxide ($x \ge 20$ %) this band strongly decreases in intensity in both systems because the P = O double bond is broken with the formation of V-O-P and Cu-O-P in the phosphate network, but it can be observed that the intensity decrease of this band is stronger in the case of $x(CuO{\cdot}2V_2O_5)(100\text{-}x)[2P_2O_5{\cdot}PbO]$ glass system, fact that indicates that the vanadium oxide induced a stronger depolimerization of the glass network.

For high V_2O_5 and CuO content ($x \ge 20$ %) a new broad band in the range 1100 – 1160 cm^{-1} appears due to the simmetric stretching vibration of V=O double bond from the pyramidal groups VO_5 [16, 17]. On the other hand, by increasing the of oxides content the band that dominates the spectra is that around 920 cm^{-1}. This band represents an overlapping of the P-O-P asymmetric vibrations in Q^1 groups with the V-O stretching vibrations [16, 17].

In the case of $x(CuO{\cdot}2V_2O_5)(100\text{-}x)[2P_2O_5{\cdot}PbO]$ glass system a new shoulder around 880 cm^{-1} appears for $x \ge 20$ % which is attributed to symmetric stretching vibrations in V-O-V chains; this fact suggests that at high V_2O_5 concentrations($x \ge 40$ % mol), vanadium oxide would play a formar role in the studied glass network. Similar results in which vanadium oxide at low concentration (usually less than 10 mol %) shows a modifier effect and at high concentration (usually more than 20 mol %) shows a forming effect were lately reported in literature [3,18] leading to the possibility of new phosphate materials production, using non-conventional glass forming oxides like vanadium oxide.

Table 1. Band assignments of inbvestigated glass systems

ν (cm^{-1})	Assignments	
	$x(CuO{\cdot}V_2O_5)$ (100-x)$[2P_2O_5{\cdot}PbO]$	$x(CuO{\cdot}2V_2O_5)(100\text{-}x)[2P_2O_5{\cdot}PbO]$
580 - 630	O – P – O bending vibrations	O– P – O bending vibrations
720 - 770	(P-O-P) symetric stretching vibrations	(P-O-P) symetric stretching vibrations
~880	-	V-O-V symmetric stretching vibrations
~ 920	(P-O-P)asym. stretch. vibrations V-O stretching vibrations	(P-O-P)asym. stretch. vibrations V-O stretching vibrations
~ 1050	asymmetric stretching vibrations in PO_3^{2-} ionics group	asymmetric stretching vibrations in PO_3^{2-} ionic group
1100-1160	asymmetric stretching vibrations in ionics group PO_2^- V= O symmetric stretching vibrations	asymmetric stretching vibrations in ionics group PO_2^- V= O symmetric stretching vibrations
1250-1280	P=O stretching vibration	P=O stretching vibration

CONCLUSIONS

$x(CuO{\cdot}V_2O_5)(100\text{-}x)[2P_2O_5{\cdot}PbO]$ and $x(CuO{\cdot}2V_2O_5)(100\text{-}x)[2P_2O_5{\cdot}PbO]$ with $0 \le x \le 40$ % mol were prepared using conventional method of molten sub-cooling; the samples were found to be insignificant hygroscopic and they present a high degree of chemical durability.

IR spectra reveled that by adding V_2O_5 and CuO the bands that dominate the spectra are those characteristic to vanadium oxide and those specific to small phosphate groups (Q^1). This fact suggest that by addition of these oxides a strong depolymerization of phosphate network appears.

A comparison made between the investigated systems proved that in the case of $x(CuO{\cdot}2V_2O_5)(100\text{-}x)[2P_2O_5{\cdot}PbO]$ glass system a shoulder around 880 cm^{-1} appears in IR spectra for $x \ge 20$ % attributed to symmetric stretching vibrations in V-O-V chains, suggesting that at high V_2O_5 concentrations vanadium oxide would play a formar role in the studied glass network.

REFERENCES

[1]. P.Y. Shih, Mat. Chem. Phys. 80, 299 (2003)

[2]. V. Sudarsan, R. Mishra, S. K. Kulshreshtha, J. Non-Cryst. Solids 342,160-165 (2004)

[3]. G. Tricot, L. Montagne, L. Delevoye, G. Palavit, V. Kostoj, J. Non-Cryst. Solids 345-346, 56-60 (2004)

[4]. Y.B. Saddeek, E.R. Shaaban, K.A. Aly, I.M. Sayed, J. Alloy Comp. 478, 447-452 (2009)

[5]. A.M. Efimov, J. Non-Cryst. Solids 209, 209 (1997)

[6]. Richard K. Brow, J. Non-Cryst. Solids 263&264,1 (2000)

[7]. M. Scagliotti, M. Villa, G. Chiodelli, J. Non-Cryst. Solids 93, 350 (1987)

[8]. A. Moguš-Milanković, A. Šantić, S.T. Reis, K. Furic, D.A. Day, J. Non-Cryst. Solids 342, 97 (2004)

[9]. P. Subbalakshmi, N. Veeriah, J. Non-Cryst. Solids 298, 89 (2002)

[10]. C.G. Granqvist, Handbook of Innorganic Electrochromic Materials, Elsevier, New York, 1995

[11]. G. Le Saout, P. Simon, F. Fayon, A. Blin, Y. Vaills, J. Raman Spectrosc., 33:740-746 (2002)

[12]. K. Nakamoto, Infrared spectra of Inorganic and Coordination compounds, Wiley-Interscience, New-York, 170

[13]. Y.M. Moustafa, A. El-Adawy, Phys. Stat. Sol (a) 179, 83 (2000)

[14]. J.J. Hudgens, S.W. Martin, J. Am. Ceram. Soc. 76, 1691-1696 (1993)

[15]. B.V.R. Chowdari, K.I. Tan, W.T. Chia, R. Gopalakrishnam, J. Non-Cryst. Solids 119, 95-102 (1990)

[16]. M. Sayer, A. Mansingh, Phys. Rev. B, 6, 4629 (1972)

[17]. D. Ilieva, B. Jivov, D. Kovacheva, T. Tsacheva, Y. Dimitriev, G. Bogachev, C. Petrov, J. Non-Cryst. Solids 293, 562 (2001)

[18]. N. Vedeanu, O. Cozar, I. Ardelean, B. Lendl, D.A. Magdas, Vibr. Spectr., 48 (2), 259 (2008)

STUDIA UBB PHYSICA, Vol. 57(LVII), 1, 2012, pp. 41 - 48
(RECOMMENDED CITATION)

STRUCTURAL CHARACTERIZATION OF CuO-TeO_2-Li_2O-GeO_2 GLASSES BY INFRARED AND RAMAN SPECTROSCOPY

I.C. MARCUS[1], R. CICEO LUCACEL[2,*], I. ARDELEAN[2]

ABSTRACT. Glasses following the composition described by expression $xCuO\cdot(1-x)[2TeO_2\cdot Li_2O\cdot 0.2GeO_2]$ were prepared using classical melt quenching technique. Spectroscopic methods, namely FT-IR absorption and Raman scattering, were employed to reveal the structural peculiarities of the synthesized materials. These two complementary techniques are frequently used to obtained detailed information about the structure of the glasses, because are sensitive to local symmetry, character of chemical bonds and other structural properties. The interpretation of the obtained vibrational spectra reveals that the glasses network structure is composed of TeO_4 trigonal bipyramids (tbp), TeO_3 trigonal pyramids (tp), TeO_{3+1} polyhedral units, and also GeO_4 tetrahedral units. Copper oxide addition implies a change in the tellurium atoms coordination from 4 to 3 via intermediate 3+1 units and an increase of non-bridging oxygen (NBO) amount, modifications reflected in studied glasses spectra.

Keywords*:* Lithium-germanium-tellurite glasses, copper ions, FT-IR, Raman

INTRODUCTION

Being interesting materials from theoretical and practical point of view tellurite glasses were studied over the years to establish their structure at medium and short range order. Increasing interest on TeO_2 based glasses during the last decade is due to their properties such as: chemical durability, broad homogeneity range, good thermal stability and strength, corrosion resistance [1, 2], low melting temperature [3, 4], high dielectric constant [4, 5], high thermal-expansion coefficient, thermochromic properties [6 - 8], high density [9], high glass transition temperature [10] and low fusion temperature [11]. Tellurite glasses have important commercial applications in solid state batteries, fuel cells, gas sensors, infrared filters, host materials for laser applications [12, 13], optical fibers, modulators, memories, and laser windows [14].

[1] CEST Center for Electrochemical Surface Technology, A-2700 Wiener Neustadt, Austria
[2] Babes-Bolyai University, Faculty of Physics, 400084, Cluj-Napoca, Romania
* raluca.lucacel@phys.ubbcluj.ro

In order to find a correlation between the physical properties observed in tellurite based glasses and their atomic arrangements, structural characterization were carried out employing several techniques: infrared (IR) spectroscopy [7, 10, 15], Raman scattering [14, 16, 17], nuclear magnetic resonance [18], X-ray absorption [19, 20], X-ray [15, 21] and neutron diffraction [22]. From these studies, was concluded that tellurite network is build up from asymmetric structural units: TeO_4 trigonal bipyramids (tbp), TeO_{3+1} polyhedra and TeO_3 trigonal pyramids (tp). The TeO_4 group has two axial and two equatorial oxygen atoms. The concentration of characteristically structural units and TeO_4 tbp transformation into TeO_{3+1} and TeO_3 tp units is strongly affected by glass composition, network modifier type and concentration, and by other causes [12, 21]. Introduction of a network modifier changes the Te coordination polyhedron from TeO_4 to TeO_3 through breaking Te-O-Te bonds, along with the formation of non bridging oxygen (NBO) atoms.

GeO_2-based glasses structure consists of tetrahedral and octahedral units of germanium connected with oxygen atoms [17, 23, 24, 25]. With the increase of modifier content in glasses the germanium atoms coordination changes from four-fold to six-fold. Germanium oxide was added into tellurite glasses due to its properties and to improve the glass forming ability and thermal stability [23].

Lithium oxide addition into tellurite glasses determines an increase of ionic conductivity [13]. Transition-metal oxide (CuO for example) presence into tellurite glasses gives them specific semiconducting and magnetic properties [26, 27]. Copper addition into GeO_2-TeO_2 system increases their ability to crystallize and decreases glass forming tendency, fact reported by Ligero et al. [28]. The investigation of samples from this system is complicated by the existence of two network formers (TeO_2 and GeO_2) and the fact that both tellurium and germanium are know to have more than one stable coordination. This paper reports the preparation and the structural characterization of litium-germanate-tellurite glasses doped with copper ions.

EXPERIMENTAL

Studied samples were prepared using conventional melt quenching technique, with CuO, TeO_2, Li_2CO_3 and GeO_2 of reagent grade purity as starting materials. The chemicals in the appropriate amounts were melted in air, in sintered corundum crucibles, in an electric furnace at 1200°C and maintained for 30 minutes at this temperature. The mixtures were introduced directly in the preheated furnace at this temperature to avoid losses due to evaporation. Resulting melts were quickly cooled at room temperature by pouring and pressing between two stainless steel plates to obtain good homogeneity.

Infrared spectra were recorded with a FT-IR 6100 Jasco spectrometer. Samples were prepared for these measurements in form of KBr pellets, containing 2 wt % glasses. In order to obtain good quality spectra the samples were crushed

in an agate mortar to obtain particles of micrometer size. This procedure was applied every time to fragments of bulk glass to avoid structural modifications due to ambient moisture. FT-IR absorption spectra were measured immediately after preparing the desired discs. The spectral resolution used to record the FT-IR spectra was 2 cm^{-1}. Raman spectra of prepared samples were measured with a Raman spectrometer (Jobin-Yvon-Horiba, HR LabRam inverse), employing 532 nm excitation line of a frequency-doubled Nd: YAG laser (Coherent Compass). Raman signal wad collected with a charge-coupled-device camera (CCD) operating at 220 K. Raman spectral resolution was 2 cm^{-1} and was used a laser power of 10 mW incident on sample. Bulk glasses were used for Raman measurements. Both FT-IR and Raman measurements were performed at room temperature.

RESULTS AND DISCUSSION

Table I summarize the assignments of the bands detected in the FT-IR spectra (Fig. 1) of prepared samples.

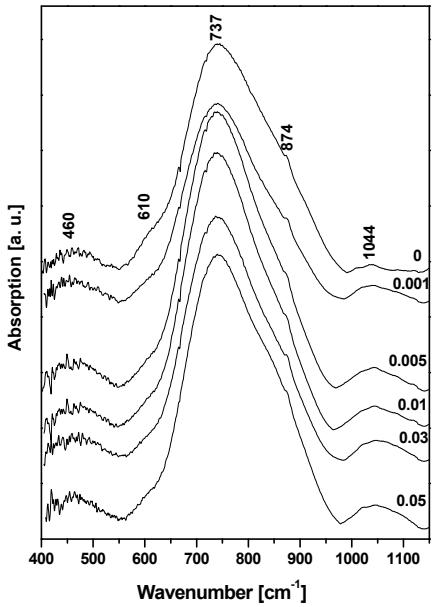

Fig. 1. FT-IR spectra of $xCuO\cdot(1-x)[2TeO_2\cdot Li_2O\cdot 0.2GeO_2]$ glasses

The assignments were made comparing the obtained results with the ones from literature corresponding to crystalline samples [1, 2, 16, 17, 27]. Germanium-oxygen stretches are active in spectral range where the tellurium-oxygen arrangements absorb strongly and this complicates the study of a mixed germanate-tellurate network.

FT-IR spectrum of glass matrix $2TeO_2 \cdot Li_2O \cdot 0.2GeO_2$ presents a relative low number of bands: a weak band at ~ 460 cm^{-1}, a strong band at ~ 737 cm^{-1} and two shoulders at ~ 610 and ~ 874 cm^{-1}, and a weak band situated at ~ 1044 cm^{-1}. The presence of these bands is a proof that the matrix structure is build up from characteristic units for the two network formers: TeO_4, TeO_3 and GeO_4 units. The existence of TeO_{3+1} polyhedral units, where one Te-O axial distance is elongated while the opposite is shortened, was detected and is evidenced by ~ 737 cm^{-1} band presence. Therefore, studied glass network is a mixture of TeO_4, TeO_{3+1}, TeO_3 and GeO_4 units. In a glass structure with mixed glass formers, the connection between structure units could be non-symmetric bridged structure units and/or non-bridged oxygen atoms. Lithium oxide enters in the glass network as an intermediate between the two network formers, increases the number of non-bridging oxygen, and weakness Te-O and Ge-O bonds [29].

Table I. Assignments of FT-IR and Raman bands in $xCuO \cdot (1-x)[2TeO_2 \cdot Li_2O \cdot 0.2GeO_2]$ glasses spectra

Peak positions (cm^{-1})		**Assignments**	
FT-IR	*Raman*	*FT-IR*	*Raman*
~ 460	~ 325	Vibrations of Te-O-Te bridging bond in TeO_4 tbp units; symmetric stretching vibrations of Ge-O-Ge from GeO_4 units	Bending vibrations of TeO_3 tp units with NBOs; Ge-O-Ge bending modes
~ 610	~ 470	Te-O bonds in TeO_4	Bending vibrations of Te-O-Te or O-Te-O linkages in TeO_4 tbp units; symmetric stretching vibrations of Ge-O-Ge
~ 737	~ 560	Stretching vibrations of TeO_3 tp or TeO_{3+1} polyhedra with NBOs; vibrations of GeO_4 units	Ge-O-Ge bending
~ 874	~ 773	Stretching vibrations mode of TeO_3 tp with NBOs; asymmetric stretching vibrations of Ge-O-Ge in GeO_4 units	Vibrations of TeO_3 tp and TeO_{3+1} units; Ge-O^- and Ge-O-Ge symmetric stretching vibrations in GeO_4
~ 1044	~ 1090	Asymmetric stretching vibrations of Ge-O-Ge	Symmetric stretching vibrations of Ge-O^-

Adding CuO in the glass matrix the band situated at ~ 460 cm^{-1}, attributed to vibrations of Te-O-Te bridging bond in TeO_4 tbp units but can come from a small contribution of symmetric stretching vibrations of Ge-O-Ge from GeO_4 units, increase in intensity, meaning that the network connectivity increases [14, 20]. The intensity

of the shoulder situated at ~ 610 cm^{-1} decrease, showing that the Te-O bonds from the TeO_4 units are broken. The position of strongest band in the spectra (~ 737 cm^{-1}) is not shifted with the addition of CuO, only weakly increase in intensity, meaning that TeO_3, TeO_{3+1} and GeO_4 units amount enlarges. The shoulder positioned at ~ 874 cm^{-1} suffers no major changes with CuO addition. The intensity of the weak band positioned at ~ 1044 cm^{-1} increase with the increase of CuO content, denoting that the amount of Ge-O-Ge linkages reaches the highest amount for x = 0.05 content.

With copper oxide addition the intensity of the bands detected in the FR-IR spectra increases, denoting a progressively disorder of the structure of the glass. In all the compositional range the amount of the units where tellurium is 3 coordinated is higher than the one in which is 4 coordinated, fact confirmed by the assignments of the detected bands. With the increases of the CuO content, the cleavage of continuous network leads to an increase of the TeO_{3+1} polyhedra fraction. The elongation of the Te-O bond from TeO_{3+1} and its cleavage finally lead to the formation of the TeO_3 units.

The Raman spectra obtained for the prepared samples are shown in figure 2, while the assignments of the bands detected are revealed in Table I. The Raman spectrum of the glass matrix present three weak bands positioned at ~ 325, ~ 470 and ~ 1090 cm^{-1}, while the one situated at ~ 773 cm^{-1} dominates the spectrum. The existence of these features in the Raman spectrum suggests that a mixed tellurium oxide and germanium oxide glass network has been formed in the sample, where tellurium is mostly in trigonal pyramidal units and germanium in distorted tetrahedral units. The presence of these bands revealed by Raman scattering confirms the existence of the same characteristic units proposed for glass matrix by FT-IR measurements.

The weak band positioned at ~ 325 cm^{-1} is attributed to the bending vibrations of TeO_3 tp units with NBO and also to Ge-O-Ge bending modes. The band at ~ 470 cm^{-1} could come from bending vibrations of Te-O-Te or O-Te-O linkages in TeO_4 tbp units, and also from symmetric stretching vibrations of Ge-O-Ge. The band at ~ 665 cm^{-1} characteristic for TeO_4 units is not present as a well define band in Raman spectra, but is hidden under de broad envelope center at ~ 773 cm^{-1}. The band at ~ 773 cm^{-1} is characteristic for TeO_3 and TeO_{3+1} units and because is the strongest band in the spectrum can be concluded that the predominant coordination for tellurium is 3. The weak band at 1090 cm^{-1} could come from symmetric stretching vibrations of $Ge-O^-$.

Copper oxide addition implies no major shifts for the Raman bands. The weak band positioned at ~ 325 cm^{-1} decrease in intensity with CuO addition. The fact that the ~ 470 cm^{-1} band intensity decrease with increasing cooper amount suggests that doping the glass matrix the Te-O-Te and/or Ge-O-Ge linkages are deformed and/or destructed. Concomitantly the amount of NBO increases fact which is consistent with the conversion of TeO_4 into TeO_3, having one NBO. When copper content reaches 0.05 value a new week band situated at ~ 560 cm^{-1} is observed in

the spectra. This band was assigned by Henderson et al. [24] to Ge-O-Ge bending associated with ring strain. The band from ~ 773 cm^{-1} decreases in intensity but remains the strongest in the spectrum. The amount in which tellurium is 3 coordinated is higher that the one in which is 4 coordinated for all compositional range. Symmetric stretching vibrations of $Ge\text{-}O^-$ and Ge-O-Ge merged under the ~ 773 cm^{-1} band.

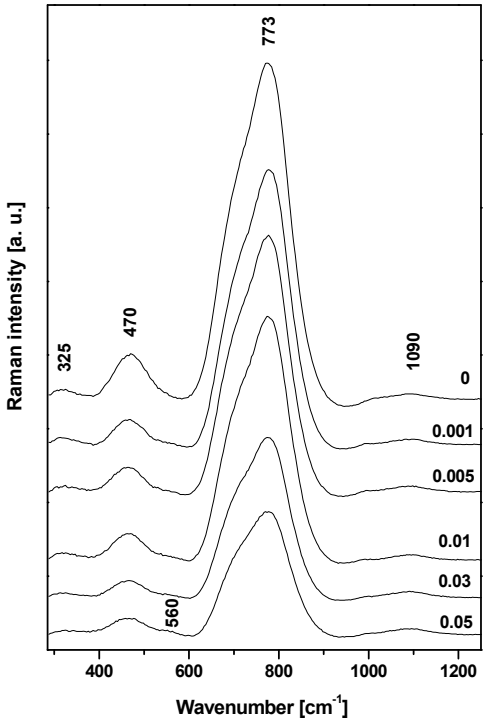

Fig. 2. Raman spectra of $xCuO\cdot(1\text{-}x)[2TeO_2\cdot Li_2O\cdot 0.2GeO_2]$ glasses

With the gradual addition of the copper oxide in the glass composition is observed a gradual decrease of the intensity of the Raman bands, indicating an increase of the vitreous network depolymerization degree. As observed from the FT-IR investigations, Raman results confirm a continuously change of the glass structure and Te coordination from 4 to 3 via intermediate species TeO_{3+1}.

CONCLUSIONS

The structure of the prepared glass samples was investigated by FT-IR absorption and Raman scattering. Characteristic units for tellurium (TeO_4 trigonal bipyramids, TeO_{3+1} polyhedra and TeO_3 trigonal pyramids) and germanium (GeO_4

tetrahedra) atom were detected in the structure of the investigated glasses by both spectroscopic techniques used. The existence of GeO_6 octahedral units characteristic for germanium atom was not detected by any of the two techniques. With copper oxide addition the coordination of tellurium is changing from TeO_4 trigonal bipyramids to TeO_3 trigonal pyramids via intermediate species TeO_{3+1} polyhedra, simultaneously with an increase in the non-bridging oxygen amount. From the changes induced by copper oxide addition in glasses structure can be concluded that it acts as a network modifier, information confirmed by both FT-IR and Raman data.

REFERENCES

[1]. M.D. O'Donnell, C.A. Miller, D. Furniss, V.K. Tikhomirov, A.B. Seddon, J. Non-Cryst. Solids **331**, 48 (2003).

[2]. M. Udovic, P. Thomas, A. Mirgorodsky, O. Durand, M. Soulis, O. Masson, T. Merle-Mejean, J.C. Champarnaud-Mesjard, J. Solid State Chemistry **179**, 3252 (2006).

[3]. P. Charton, P. Armand, E. Philippot, Proc. Int. Congr. Glass. **2**, 378 (2001).

[4]. A. Abd El-Moneim, Mat. Chem. Phys. **73**, 318 (2002).

[5]. C.Y. Wang, Z.X. Shen, B.V.R. Chowdari, J. Raman Spectrosc. **29**, 819 (1998).

[6]. S. Suehara, S. Hishita, S. Inoue, A. Nukai, Phys. Rev. B **58 (21)**, 14 124 (1998).

[7]. J.C. Sabadel, P. Armand, D. Cachau-Herreillat, P. Baldeck, O. Doclot, A. Ibanez, E. Philippot, J. Solid State Chem. **132**, 411 (1997).

[8]. H. Li, Y. Su, S.K. Sundaram, J. Non-Cryst. Solids **293-295**, 402 (2001).

[9]. D.K. Durga, P. Yadagiri, N. Veeraiah, J. of Luminescence **99**, 53 (2002).

[10]. I. Shaltout, Y. Badr, Physica B **381**, 187 (2006).

[11]. M.A.P. Silva, Y. Mesaddeq, S.J.L. Ribeiro, M. Poulin, F. Villain, V. Briois, J. Phys. Chem. Solids **62**, 1055 (2001).

[12]. C. Duverger, M. Bouzaoui, S. Turrell, J. Non-Cryst. Solids **220**, 169 (1997).

[13]. K. Muruganandam, M. Seshasayee, J. Non-Cryst. Solids **222**, 131 (1997).

[14]. P. Charton, P. Armand, J. Non-Cryst. Solids **333**, 307 (2004).

[15]. P. Charton, P. Thomas, P. Armand, J. Non-Cryst. Solids **321**, 81 (2003).

[16]. N. Jaba, A. Mermet, E. Duval, B. Champignon, J. Non-Cryst. Solids **351**, 833 (2005).

[17]. M. Mattarelli, A. Chiappini, M. Montagna, A. Martucci, A. Ribaudo, M. Guglielmi, M. Ferrari, A. Chiasera, J. Non-Cryst. Solids **351**, 1759 (2005).

[18]. V. Sudarsan, R. Mishra, S.K. Kulshreshtha, J. Non-Cryst. Solids **342**, 160 (2004).

[19]. M.A.P. Silva, Y. Mesaddeq, S.J.L. Ribeiro, M. Poulin, F. Villain, V. Briois, J. Phys. Chem. Solids **62**, 1055 (2001).

[20]. P. Charton, P. Armand, J. Non-Cryst. Solids **333**, 307 (2004).

[21]. R.F. Cuevas, L.C. Barbosa, A.M. de Paula, Y. Liu, V.C.S. Reynoso, O.L. Alves, N. Aranha, C.L. Cesar, J. Non-Cryst. Solids **191**, 107 (1995).

[22]. S. Neov, V. Kozhukharov, I. Gerasimova, B. Sidzhimov, J. Non-Cryst. Solids **126 (3)**, 255 (1990).

[23]. Z. Pan, S. H. Morgan, J. Non-Cryst. Solids **210**, 130 (1997).

[24]. G.S. Henderson, R.T. Amos, J. Non-Cryst. Solids **328**, 1 (2003).

[25]. E.I. Kamitsos, Y.D. Yainnopoulos, M.A. Karakassides, G.D. Chryssikos, H. Jain, J. Phys. Chem. **100**, 11755 (1996).

[26]. M.A. Salim, G.D. Khattak, N. Tabet, L.E. Wenger, J. Elect. Spec. **128**, 75 (2003).

[27]. G.D. Khattak, A. Mekki, L.E. Wegner, J. Non-Cryst. Solids **337**, 174 (2004).

[28]. R.A. Ligero, M. Gasa-Ruiza, M.T. Trujillo, A. Grozco, R. Jiménez-Garay, Phys. Chem. Glasses **35**, 115 (1994).

[29]. Z. Pan, D.O. Henderson, S.H. Morgan, J. Chem. Phys. **101**, 1767 (1994).

STUDIA UBB PHYSICA, Vol. 57(LVII), 1, 2012, pp. 49 - 58
(RECOMMENDED CITATION)

TWO-CENTER EFFECTS IN THE IONIZATION OF HETERONUCLEAR MOLECULES

K. NAGY-PÓRA[1], L. CZIPA[1], L. NAGY[1,*]

ABSTRACT. A theoretical study is presented for the ionization of the HeH^+ molecular ion by fast proton projectiles. Interference structures are identified in the ejected electron spectra due to the coherent emission of the electrons from the vicinity of the two nuclei. The observed oscillations are less pronounced than those observed for the hydrogen molecule. The present results are in good agreement with other theoretical calculations.

Keywords: heteronuclear molecules, ionization, interference effect

INTRODUCTION

Interference effects in the ejected electron spectra, for the ionization of diatomic molecules (H_2) by fast charged projectiles, were first observed by Stolterfoht et al [1]. The cause of this interference is obvious from the point of view of quantum mechanics (coherent emission of the waves associated to the electron from the vicinity of the two nuclei), but at that time it was somewhat surprising, that the interference pattern may be observed also for a target with randomly oriented molecules. The interference was evidenced by representing the ratio of the differential cross sections obtained for the hydrogen molecule and two hydrogen atoms as a function of the ejected electron velocity for different ejection angles. There are several theoretical explanations of the effect [2-4], and it was also predicted the dependence of the observed oscillation's frequency on the ejection angle of the outgoing electron [2], confirmed later experimentally [5]. This kind of interference effect was evidenced in the last decade by several experimental groups for the hydrogen molecule [6-10] and also for other homonuclear diatomic molecules [11-13]. Recently other molecules were also studied, such as H_2O [14], where the effect is more complicated, than for diatomic molecules.

[1] Babeş-Bolyai University, Faculty of Physics, 1 Kogălniceanu Str., 400084 Cluj-Napoca, Romania
[*] lnagy@phys.ubbcluj.ro

In order to understand in more detail the interference effects observed in the ionization of molecules, it is of interest the study of heteronuclear diatomic molecules, when the ejection of the electrons from the two atoms is not symmetric. Tachino et al [15, 16] performed theoretical calculations to study the ionization of the HeH^+ molecular ion, a heteronuclear molecule with two electrons.

The authors have compared the observed interference effects to those occurring for the hydrogen molecule. Because the ejection from the vicinity of the helium nucleus dominates, the interference oscillations are less pronounced that in the case of the homonuclear hydrogen molecule, as expected.

In the present paper we generalize our previous model for the H_2 [2], and apply it for studying the interference effects for the ionization of the HeH^+ molecular ion by proton impact. We compare our results with those of Tachino et al [16] and analyze the observed oscillations in the differential cross section ratio as a function of the ejected electron velocity for different ejection angles.

THEORY

For the studied heteronuclear molecule we apply the same method, which was successfully used to describe the interference effects in the ionization of the hydrogen molecule by fast charged ions [2]. In the impact parameter formulation, using first order perturbation theory, the transition probability amplitude for the ionization of the molecule in case of a certain orientation of the molecular axes **D** can be written as

$$a\left(b,\hat{\mathbf{D}}\right)=\frac{iZ_p}{v}\int_{-\infty}^{+\infty}e^{iqZ}\left\langle\psi_k(r)\left|\frac{1}{|\mathbf{r}-\mathbf{R}|}\right|\psi_i(\mathbf{r},\mathbf{D})\right\rangle dZ\,. \tag{1}$$

Here *b* is the impact parameter, *v* the velocity of the projectile, *r* the position vector of the active electron, while $\psi_i(\mathbf{r},\mathbf{D})$ and $\psi_k(r)$ are its initial and the final state wavefunctions, respectively, **k** being the momentum of the ejected electron.

The position of the projectile along its trajectory is $\mathbf{R}=b\mathbf{e}_x+Z\mathbf{e}_z$ with $Z=v\cdot t$. The origin is on the molecular axis, at distance κD from the helium nucleus. In our calculations we apply several different values between 0 and 1 for the factor κ. The well known minimum momentum transfer is $q=\Delta E/v$, where $\Delta E=E_i+k^2/2$ is the energy transfer to the electron, E_i being the ionization energy.

The initial state of the active electron in the molecule is described by a linear combination of two hydrogenlike *1s* atomic orbitals centered at each of the nuclei

$$\psi_i(\mathbf{r},\mathbf{D})=c_1e^{-\alpha_1|\mathbf{r}+\kappa\mathbf{D}|}+c_2e^{-\alpha_2|\mathbf{r}-(1-\kappa)\mathbf{D}|}\,, \tag{2}$$

where the coefficients c_1 and c_2 give the contributions of the atomic orbitals to the molecular orbital, and α_1 and α_2 are the effective charges for the two atoms (He, respective H). Approximating by plane waves the final state wavefunction for the ejected electron with momentum **k**

$$\psi_{\mathbf{k}}(\mathbf{r}) = \frac{1}{(2\pi)^{3/2}} e^{i\mathbf{kr}}, \tag{3}$$

the calculations can be performed as was described in detail for the hydrogen molecule [2]. Using the Bethe integral and applying the peaking approximation [17] valid for large momentum of the ejected electron ($k > 1$), we get for the transition probability amplitude

$$a(b,\hat{\mathbf{D}}) = \frac{iZ_p}{vk^2}\sqrt{\frac{2}{\pi}} e^{-i\mathbf{bk}_\perp} \int_{-\infty}^{+\infty} e^{i(q-k_{||})Z} \psi_i(\mathbf{R},\mathbf{D}) dZ . \tag{4}$$

Here we have decomposed the electron momentum according to

$$\mathbf{kR} = \mathbf{k}_\perp \mathbf{b} + k_{||} Z , \tag{5}$$

where $\mathbf{k}_\perp$ and $k_{||}$ are the perpendicular and parallel components of the final momentum **k**, relative to the *z* axes, respectively. Since we have integrated analytically over the position vector of the electron we note, that in (4) the ψ_i wavefunction depends on the position vector of the projectile **R**.

With the definition $\mathbf{R} = b\mathbf{e}_x + Z\mathbf{e}_z$, the initial state eq. (2) becomes

$$\psi_i(\mathbf{R},\mathbf{D}) = c_1 e^{-\alpha_1\sqrt{(Z+\kappa D_{||})^2 + b_+^2}} + c_2 e^{-\alpha_2\sqrt{(Z-(1-\kappa)D_{||})^2 + b_-^2}} \tag{6}$$

where b_+ and b_- are the impact parameters relative to the two nuclei

$$b_+ = \sqrt{b^2 + \kappa^2 D_\perp^2 + 2b\kappa D_\perp \cos\varphi_D} \tag{7}$$

$$b_- = \sqrt{b^2 + (1-\kappa)^2 D_\perp^2 - 2b(1-\kappa) D_\perp \cos\varphi_D} . \tag{8}$$

Here $D_{||}$ and $D_\perp$ are the parallel and perpendicular components of the internuclear separation vector. φ_D stands for the angle between the impact parameter **b**, chosen here parallel to $\mathbf{e}_x$ and the perpendicular component of the molecular axes, while θ_D used later is the corresponding polar angle. (See Fig. 1)

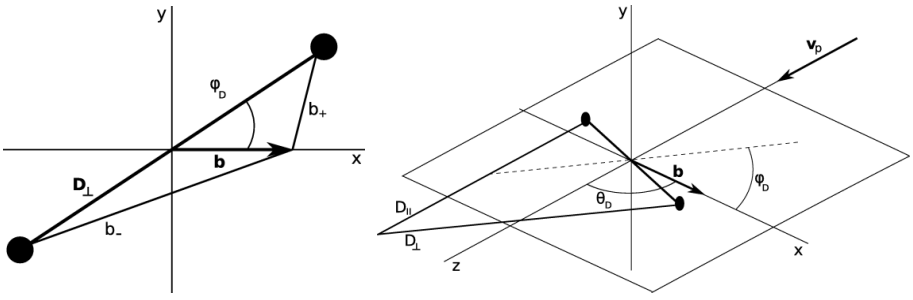

Fig. 1. Definitions of the quantities, distances and angles

The integrations over Z can be performed analytically [17]

$$\int_{-\infty}^{+\infty} e^{iQZ} e^{-\alpha_{1,2}\sqrt{(Z+L_\pm)^2+b_\pm^2}}\,dZ = e^{-iQL_\pm}\,\frac{2\alpha_{1,2}b_\pm}{\sqrt{\alpha_{1,2}^2+Q^2}}\,K_1\left(b_\pm\sqrt{\alpha_{1,2}^2+Q^2}\right) \tag{9}$$

where $K_1(x)$ denotes the modified Bessel function, Q stands for $(q\text{-}k_{//})$, while $L_+=\kappa D_{//}$ and $L_-=-(1-\kappa)D_{//}$. With the notation

$$\gamma_{1,2} = \sqrt{\alpha_{1,2}^2 + \left(q - k_{||}\right)^2}\,, \tag{10}$$

the transition probability for a given impact parameter and orientation of the molecular axes may be expressed by a similar formula to that for the homonuclear H_2 molecule

$$w(b,\hat{\mathbf{D}}) = \frac{8}{\pi}\frac{Z_p^2}{v^2k^4}\left[c_1^2\frac{\alpha_1^2}{\gamma_1^2}\left(b_+K_1(b_+\gamma_1)\right)^2 + c_2^2\frac{\alpha_2^2}{\gamma_2^2}\left(b_-K_1(b_-\gamma_2)\right)^2 + \right.$$
$$\left. + c_1c_2\frac{\alpha_1\alpha_2}{\gamma_1\gamma_2}b_+b_-K_1(b_+\gamma_1)K_1(b_-\gamma_2)\left(e^{-i(k_{||}-q)D_{||}} + e^{+i(k_{||}-q)D_{||}}\right)\right]. \tag{11}$$

For comparison with experiment the probabilities must be averaged over molecular orientation, and integrated over the impact parameter to obtain cross sections

$$w(b) = \frac{1}{4\pi}\int d\varphi_D \int \sin\theta_D w(b,\hat{\mathbf{D}})d\theta_D \tag{12}$$

$$\frac{d\sigma}{d\Omega_k dk} = 2\pi\int bw(b)db\,. \tag{13}$$

The integrations in eqs. (12) and (13) are performed numerically and the results are discussed in the next section. Similarly to the homonuclear molecules [2], the interference pattern can be analyzed analytically, by recognizing that the most significant angular variation in eq. (11) is contained in the fast oscillating factor of the interference term

$$\frac{1}{2}\left(e^{-i(k_{||}-q)D_{||}} + e^{+i(k_{||}-q)D_{||}}\right) = \cos\left[\left(k_{||}-q\right)D\cos\theta_D\right], \tag{14}$$

where we used $D_{//}=D\cos\theta_D$ (cf. fig. 1).

Within this approximation we average only the phase factor over the orientation of the molecular axes, assuming the other variations unimportant

$$\frac{1}{2}\int_0^\pi \cos\left[\left(k_{||}-q\right)D\cos\theta_D\right]\sin\theta_D d\theta_D = \frac{\sin\left[\left(k_{||}-q\right)D\right]}{\left(k_{||}-q\right)D}. \tag{15}$$

The approximated transition probability will be

$$w(b) = c(b) + g(b)\frac{\sin\left[\left(k_{||}-q\right)D\right]}{\left(k_{||}-q\right)D}, \tag{16}$$

and the corresponding cross section (13) may be also written in an analytical form

$$\frac{d\sigma}{d\Omega_k dk} = C + G\frac{\sin\left[\left(k_{||} - q\right)D\right]}{\left(k_{||} - q\right)D}. \quad (17)$$

In order to emphasize the oscillations in the cross sections we calculate the ratio of the cross section relative to the cross section neglecting the interference, which is the first term from (17), denoted by *C*. Thus, the ratio can be written as

$$Ratio = 1 + \frac{G}{C}\frac{\sin\left[\left(k_{||} - q\right)D\right]}{\left(k_{||} - q\right)D}. \quad (18)$$

For small values of the momentum transfer *q* the oscillations as a function of the momentum (or velocity) of the ejected electron has the period $2\pi/\left(D\cos\theta_k\right)$, θ_k being the ejection angle ($k_{//}=k\cos\theta_k$). For higher velocities the momentum transfer *q* increases, modifying the oscillation period. It worth to note, that for $k_{//}$-*q*=0 the cross section ratio (18) has a principal maximum. This maximum coincides with the binary encounter peak.

RESULTS AND DISCUSSION

We have performed calculations for the ionization of the HeH^+ molecular ion by proton impact, for three different energies of the projectile. We have analyzed the obtained differential cross sections as a function of the ejected electron momentum and ejection angle. Because it is our first calculation for a heteronuclear molecule, we have performed the calculations considering the origin both in the geometric and the mass center of the molecule, or in the He nucleus. The calculations showed that the obtained results do not depend on the choice of the origin's location (the value of κ). In order to make visible the interference effect we have calculated the cross section ratio (18), and studied its dependence on the ejected electron momentum.

In order to compare our results with the other theoretical findings we represented in the figures 2-4 the present calculated cross section ratios (18) for 1 MeV/u, 13.7 MeV/u, 100 MeV/u proton projectile energy, for different electron ejection angles (0°, 30°, 90°, 150°) along the results of Tachino et al. [16]. Our simple theoretical model, used previously for the study of the homonuclear H_2 molecule, generalized now for the heteronuclear HeH^+ molecular ion, leads to oscillations in the cross section ratios. We can observe the same dependence of the oscillation's period on the electron ejection angle, as in case of the H_2 molecule [2]. Our results are in good agreement with the ones obtained by Tachino et al. [16]. In Fig. 2 at small ejection angles (0°, 30°) we can observe the principle maximum at the place of the binary encounter peak ($k_{//}=q$). At this projectile energy the place of the binary encounter peak is at *k*=12.38 a.u. in case of forward electron ejection, and decreases

as the ejection angle moves toward the perpendicular direction. For higher projectile energies the binary encounter peak is shifted towards higher electron momenta, this is the reason, why the principal maximum is not visible in Figs 3 and 4. For example for 100 MeV/u projectile energy and forward electron ejection, the place of the binary encounter peak is at k=125.46 a.u., and in our graph the maximum of the electron momentum is 15 a.u.

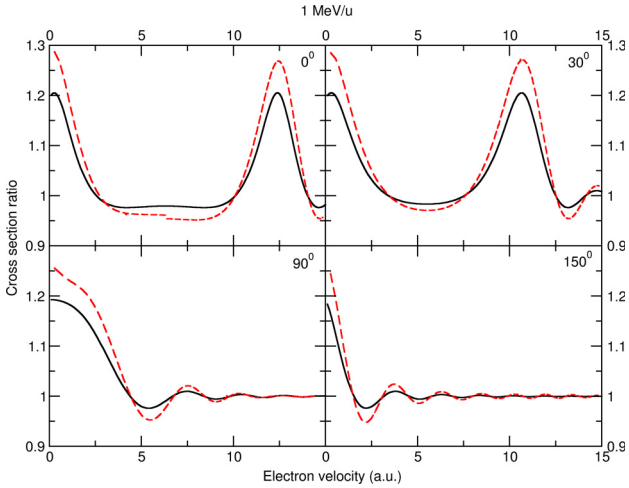

Fig. 2. Cross section ratios as a function of the ejected electron velocity, in case of ionization of the HeH^+ by 1 MeV/u proton, for different electron ejection angles. Solid lines (–) represents our present results, dashed lines (- -) are the results of Tachino et al [16]

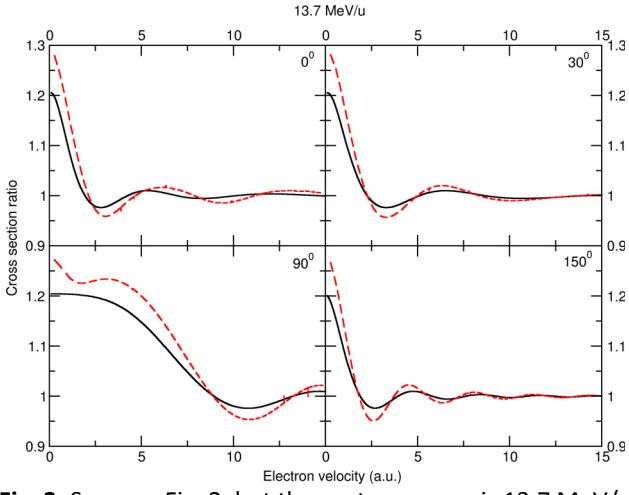

Fig. 3. Same as Fig. 2, but the proton energy is 13.7 MeV/u

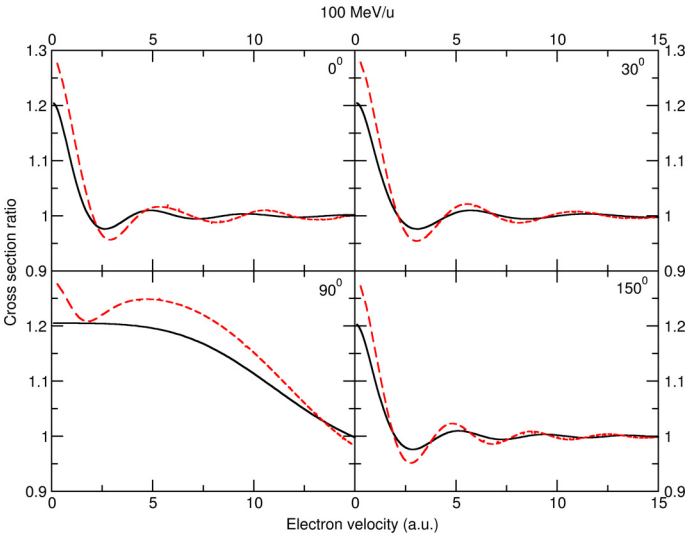

Fig. 4. Same as Fig. 2, but the proton energy is 100 MeV/u

The amplitude of the oscillations, excepting the principal maximum, is much smaller, that in case of the homonuclear H_2 molecule [2]. This was expected, because the electron density is much higher around the helium atom than around the hydrogen, and interference effects between waves of different amplitudes are less pronounced, than for equal amplitudes.

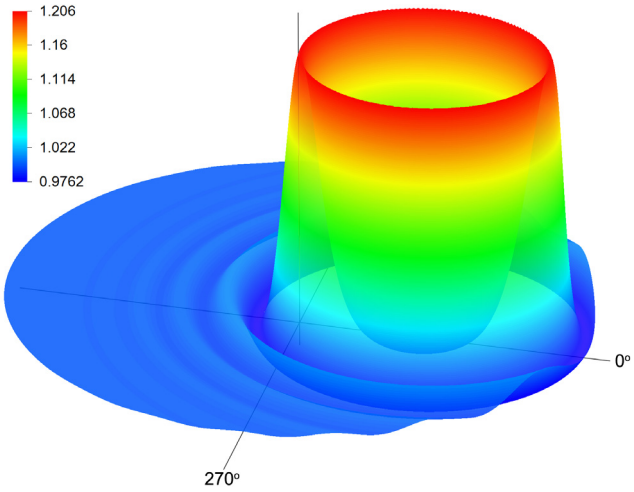

Fig. 5. Present results for the cross section ratio as a function of the ejected electron velocity and ejection angle, where the velocity is used as radial coordinate, in case of ionization of HeH^+ by 1 MeV/u proton. The maximum value of the electron velocity is 15 a.u.

Figures 5-7 are the polar representations of the cross section ratios as a function of the ejected electron momentum as the radial coordinate, and the ejection angle. Since the highest electron momentum on the graphs is 15 a.u., in case of 1 MeV/u proton impact (Fig. 5) the principal maximum, of a circular form, can be observed totally. For higher projectile energy this peak is only partially visible, because the radius of the circle of the binary encounter peak increases with increasing projectile velocity. The secondary oscillations may be observed both inside and outside the binary peak circle.

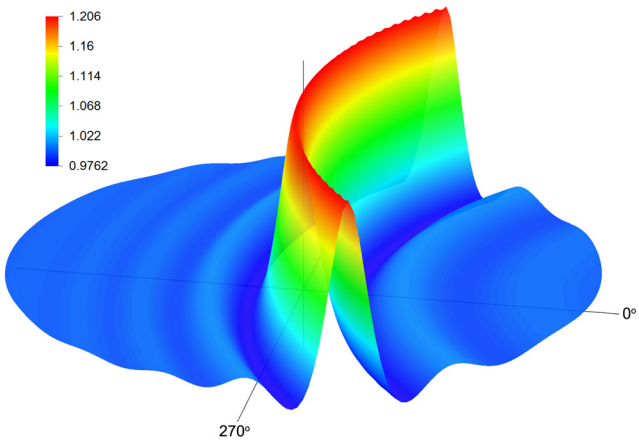

Fig. 6. Same as Fig. 5, but the proton energy is 13.7 MeV/u.

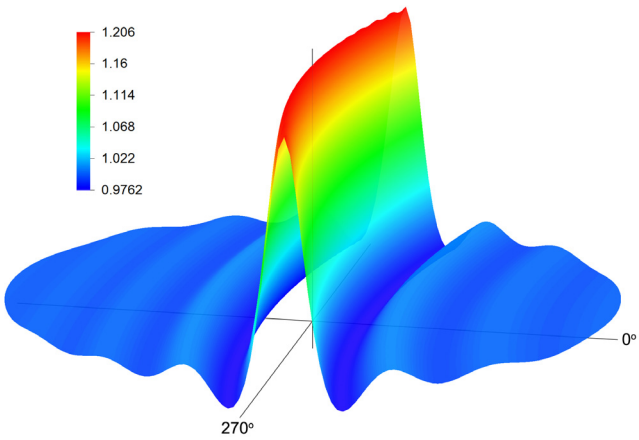

Fig. 7. Same as Fig. 5, but the proton energy is 100 MeV/u

CONCLUSIONS

We have investigated theoretically the ionization of the heteronuclear HeH^+ molecular ion, using our previous model developed for the H_2 molecule [2] generalized now for heteronuclear molecules. Interference effect was evidenced by representing the cross section ratio as a function of the ejected electron momentum. The obtained cross section ratios are in good agreement with the theoretical results of Tachino et al [16]. Both the principal maximum and the secondary oscillations are well observable on our graphs. The oscillations are less pronounced, than in case of the homonuclear diatomic molecules, as expected.

ACKNOWLEDGEMENTS

The authors are grateful to R.D. Rivarola for sending their data in numerical format. This work was supported by a grant of the Romanian National Authority for Scientifc Research, CNCS UEFISCDI, project number PN-II-ID-PCE-2011-3-0192.

REFERENCES

[1]. N. Stolterfoht et al., *Phys. Rev. Lett.* 87, 023201 (2001)

[2]. L. Nagy, L. Kocbach, K. Póra and J.P. Hansen, *J. Phys. B-At. Mol. Opt.* 35, L453 (2002)

[3]. M.E. Galassi, R.D. Rivarola, P.D. Fainstein, N. Stolterfoht, *Phys. Rev. A* 66, 052705 (2002)

[4]. L. Sarkadi, *J. Phys. B-At. Mol. Opt.* 36, 2153 (2003)

[5]. N. Stolterfoht et al., *Phys. Rev. A* 67, 030702 (2003)

[6]. D. Misra et al., *Phys. Rev. A* 74, 060701 (2006)

[7]. D. Misra, A.H. Kelkar, S. Chatterjee, L.C. Tribedi, *Phys. Rev. A* 80, 062701 (2009)

[8]. S. Chatterjee et al., *J. Phys. B-At. Mol. Opt.* 42, 065201 (2009)

[9]. S. Chatterjee, D. Misra, P.D. Fainstein and L.C. Tribedi, *Phys. Scripta* T144, 014040 (2011)

[10]. J.S. Alexander et al., *Phys. Rev. A* 78, 060701 (2008)

[11]. J.L. Baran et al., *Phys. Rev. A* 78, 012710 (2008)

[12]. M. Winkworth et al., *J. Phys. Conf. Ser.* 163, 012044 (2009)

[13]. M. Winkworth et al., *Nucl. Instrum. Meth. B* 267, 373 (2009)

[14]. A. Dubois, S. Carniato, P.D. Fainstein and J.P. Hansen, *Phys. Rev. A* 84, 012708 (2011)

[15]. C.A. Tachino, M.E. Galassi, F. Martín and R.D. Rivarola, *J. Phys. B-At. Mol. Opt.* 42, 075203 (2009)

[16]. C.A. Tachino, M.E. Galassi, F. Martín and R.D. Rivarola, *J. Phys. B-At. Mol. Opt.* 43, 135203 (2010)

[17]. J.P. Hansen and L. Kocbach, *J. Phys. B-At. Mol. Opt.* 22, L71 (1989)

STUDIA UBB PHYSICA, Vol. 57(LVII), 1, 2012, pp. 59 - 66
(RECOMMENDED CITATION)

FTIR AND UV-VIS SPECTROSCOPIC INVESTIGATION OF ERBIUM-ZINC-BORATE GLASS CERAMICS

P. PASCUTA[1,*], R. STEFAN[2], M. BOSCA[1], L. POP[1], E. CULEA[1]

ABSTRACT. Fourier transform infrared (FTIR) and Ultraviolet–Visible (UV-VIS) spectroscopic studies have been employed to investigated the samples from the $(Er_2O_3)_x \cdot (B_2O_3)_{(60-x)} \cdot (ZnO)_{40}$ ($0 \le x \le 10$ mol%) glass ceramic system. FTIR data show that the glass ceramic network structure consists on the BO_3, BO_4 and ZnO_4 structural units, and the conversion among these units mainly depends on the Er_2O_3 content. The optical absorption spectra of studied samples were recorded in the spectral range from 200 to 900 nm at room temperature. The optical band gap energy for the studied glass ceramics were calculated from the optical absorption spectra.

Keywords: Zinc borate glass ceramics; Er_2O_3; FTIR; Optical properties.

INTRODUCTION

Glass ceramics are polycrystalline materials normally obtained by controlled crystallization process of suitable glasses [1]. Most commercial glass ceramic products are formed as glass monoliths by highly automated glass-forming processes and are converted to a crystalline product by the proper heat treatment [2]. This heat treatment typically consists of a low-temperature hold to induce internal nucleation, followed by one or higher temperature holds to promote crystallization and growth of the primary crystalline phase or phases [3]. Glass ceramic are materials with new physical properties, different from parental glass obtained by structural rearrangements induced during the heat treatment [4]. The network of the pure borate glass is built by BO_3 structural units [5] mainly contained in boroxol rings $(B_3O_6)^0$. The addition of a new oxide such as divalent ZnO in the borate glasses induces the appearance of tri- BO_3 and tetra-coordinated BO_4 boron atoms [6, 7]. Subsequently the physical properties i.e.; optical, electrical are changing depending on ZnO concentration together with the response to the thermal treatment [8, 9].

[1] Biophysics Department, Agricultural Science and Veterinary Medicine University, Cluj-Napoca, Romania
[2] Physics Department, Technical University, 400020 Cluj-Napoca, Romania
[*] Corresponding author: petru.pascuta@phys.utcluj.ro

At a specific ZnO concentration threshold, non-bridging oxygen's (NBO) take place and independent pyro- $(B_2O_5)^{4-}$ and ortho-borate $(BO_3)^{3-}$ groups appear within the glass [10]. However ZnO can acting as network modifier and/or former [11] in tetra- ZnO_4 and hexa-coordinated ZnO_6 environment in various glass matrices [12] and binary $xZnO\cdot(100\text{-}x)B_2O_3$ glass due the high polarizability of Zn^{2+} ions are of technological interest for electronic devices industries [13, 14].

Glass ceramic doped with Er^{3+} can be utilized as optical amplifiers these materials have a very good stability and this property provide the ability to be pulled in fibers [4, 15, 16]. Er^{3+} ions are included in different glass and glass ceramic host providing luminescent properties as well as a large cross section of introduced rare earth ions [15].

Rare earth ions are introduced in various vitreous matrixes to improve their optical absorption. They can also provide structural information about the changes in ligand field before and after the heat treatment [17].

The aim of the present work is to investigate the structural and optical properties of erbium-zinc-borate glass ceramics using FTIR and UV-VIS spectroscopies.

EXPERIMENTAL

Glasses of the $(Er_2O_3)_x\cdot(B_2O_3)_{(60\text{-}x)}\cdot(ZnO)_{40}$ ($0 \le x \le 10$ mol%) system were prepared using Er_2O_3, H_3BO_3 and ZnO of high purity (99.9%) in suitable proportion. The mechanically homogenized mixtures were melted in sintered corundum crucibles at 1100 °C in an electric furnace. The samples were put into the electric furnace directly at this temperature. After 10 minutes the molten material was quenched at room temperature by pouring onto a stainless–steel plate. The glass ceramic samples were obtained by heat treatment of the precursor glass samples at glass transition temperature at (560 °C for 2 h) and crystallization temperature (860 °C for 2 h), respectively.

The FTIR absorption spectra were registered at room temperatures using a JASCO FTIR 6200 spectrometer. The IR absorption measurements were done using the KBr pellet technique. In order to obtain good quality spectra, the samples were crushed in an agate mortar to obtain particles of micrometer size. This procedure was applied every time to fragments of bulk glass to avoid structural modifications due to ambient moisture.

The UV–VIS absorption spectra were recorded at room temperature in the 200–900 nm range using a PerkinElmer Lambda 45 UV–VIS spectrometer equipped with an integrating sphere. The method that we used was described in our earlier work [7].

RESULTS AND DISCUSSION

FTIR spectroscopy was used to obtain essential information concerning the arrangement of the structural units of the studied glass ceramics. In order to determine the influence of the heat treatment on the structure of the studied sample we compared the FTIR spectrum of untreated glasses [18] with that recorded for the heat treated samples (Fig. 1). The FTIR spectra for the heat treated samples exhibit changes, namely those illustrated by the narrowing of the previous bands and the appearance of some new bands in the spectra. To get quantitative information about the structural groups in the studied glass ceramics, the spectra have been deconvoluted. This was made using the Spectra Manager program and a Gaussian type function that allowed us a better identification of the absorption bands which appear in these spectra in order to perform their assignment. Fig. 2 shows the deconvolution, in Gaussian bands, of the spectrum for sample containing 3 mol% Er_2O_3. The bands assignments are given in Table 1 for the studied samples.

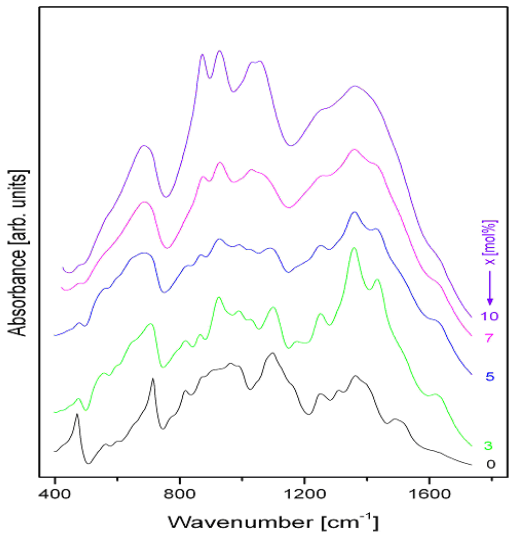

Fig. 1. FTIR spectra of the studied glass ceramics.

The presence of ZnO_4 structural units in the studied samples is confirmed by the appearances in the FTIR spectra of two absorption bands at 433-477 and 574-595 cm^{-1}. FTIR investigations evidenced the presence in the network of the studied samples of BO_3 and BO_4 structural units, but their proportion depends on erbium ions content. To follow the evolution of the triangular and tetrahedral borate units in the studied glass ceramics we used the fraction of four-coordination boron atoms,

N_4, as was defined previously [19, 20]: $N_4=A_4/(A_4+A_3)$ where A_4 and A_3 denote the areas of the BO_4 (the areas of component bands from 815-842 cm^{-1}, 863-873 cm^{-1}, 902-928 cm^{-1}, 967-987 cm^{-1}, 1010-1072 cm^{-1} and 1069-1118 cm^{-1}) and BO_3 units (the areas of component bands from 1169-1181 cm^{-1}, 1239-1258 cm^{-1}, 1301-1306 cm^{-1}, 1348-1362 cm^{-1}, 1397-1439 cm^{-1}, 1485-1515 cm^{-1}). The addition of Er_2O_3 (x = 3 mol% Er_2O_3) in the glass ceramic matrix led to the decrease of in the four-coordination boron atoms (Table 2). A further addition of Er_2O_3 over 3 mol% led to a increasing in the amount of BO_4 which will increase the stability of the glass ceramics. The threefold boron atoms are favored in the investigated glass ceramics system as compared with the fourfold ones in the whole studied concentration range.

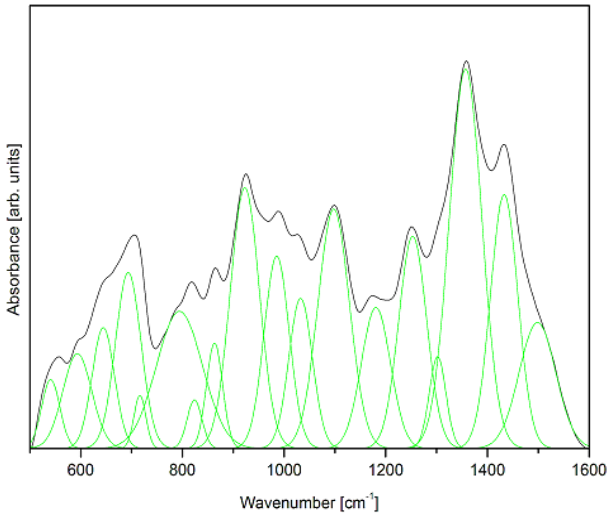

Fig. 2. Deconvoluted FTIR spectra of the glass ceramics containing 3 mol% Er_2O_3 using a Gaussian – type function.

UV-VIS absorption spectra of glass ceramics from the $(Er_2O_3)_x \cdot (B_2O_3)_{(60-x)} \cdot (ZnO)_{40}$ system, with $3 \leq x \leq 10$ mol%, recorded at room temperature in the wavelength region 200-900 nm are shows in Fig. 3. All the absorption spectra show the similar absorption bands except the different absorption intensity. The absorption occurs due to the 4f-4f electric dipole transitions from the ground $^4I_{15/2}$ state to different excited state of Er^{3+} ions. The absorption spectra exhibit 10 absorption peaks which are due to the following electronic transitions [21]: $^4I_{15/2} \rightarrow {}^4D_{5/2}$, $^2K_{15/2}$, $^4G_{9/2}$, $^4G_{11/2}$, $^2H_{9/2}$, $^4F_{5/2}$, $^4F_{7/2}$, $^2H_{11/2}$, $^4S_{3/2}$ and $^4F_{9/2}$. The most intense bands

correspond to the $^4I_{15/2} \rightarrow {}^2H_{11/2}$ and $^4I_{15/2} \rightarrow {}^4G_{11/2}$ transitions of Er^{3+} ions and are centered at 520 and 378 nm respectively.

Table 1. Assignment of the FTIR absorption bands studied glass ceramics.

Wavenumber [cm^{-1}]	Assignment
433-477	Zn-O bonds in ZO_4 units [22, 23]
540-555	B-O-B stretch involving oxygen atoms outside boroxol rings [24, 25]
574-595	Zn-O stretch in ZO_4 units [22, 23]
662-681	O-B-O bend [26, 27]
701-716	B-O-B bend [20]
764-794	$O_3B–O–BO_4$ bend [28, 29]
815-842	B–O stretch in BO_4 units from tri-, tetra- and penta-borate groups [30-33]
863-873	
902-928	B–O stretch in BO_4 units from di-borate groups [30-33]
967-987	
1010-1072	B–O stretch in BO_4 units from tri-, tetra- and penta-borate groups [30-33]
1069-1118	
1169-1181	B-O_{symm} stretch in BO_3 units from pyro- and ortho-borate groups [30-33]
1239-1258	B–O stretch in BO_3 units from boroxol rings [30-33]
1301-1306	B–O stretch in BO_3 units from varied types of borate groups [30-33]
1348-1362	
1397-1439	B-O^- stretch in BO_2O^- units from varied types of borate groups [30-33]
1485-1515	

Optical absorption spectra in solids provide essential information about the optical band gap energy in crystalline and non-crystalline materials. An expression for the absorption coefficient, α(ν), as a function of photon energy, *hν*, for direct and indirect optical transitions was given by Davis and Mott [34] as:

$$\alpha(\nu) = \frac{\alpha_0(h\nu - E_g^{opt})^p}{h\nu}$$

where the exponent p = 1/2 for allowed direct transitions, while p = 2 for allowed indirect transitions, E_g^{opt} is the optical band gap energy in eV (the optical band gap in glasses is closely related to the energy gap between the valence band and conduction band) and α_0 is an energy independent constant.

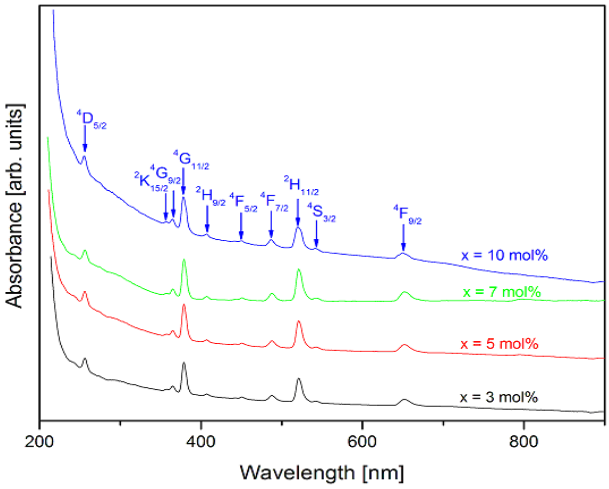

Fig. 3. UV-VIS absorption spectra of studied glass ceramics.

By plotting $(\alpha h\nu)^{1/2}$ as a function of $h\nu$, can be calculated the optical band gap energy for indirect (E_g^{opt}) transitions. The values of E_g^{opt} have been estimated from the linear regions of the curves by extrapolating them to meet the $h\nu$ axis at $(\alpha h\nu)^{1/2} \rightarrow 0$ as shown in Fig. 4. The values obtained for E_g^{opt} are shown in Table 2 for all the studied glass ceramics. The values of the optical band gap energy decrease from 4.88 eV to 4.51 eV when the content of Er_2O_3 increases from 3 to 10 mol%.

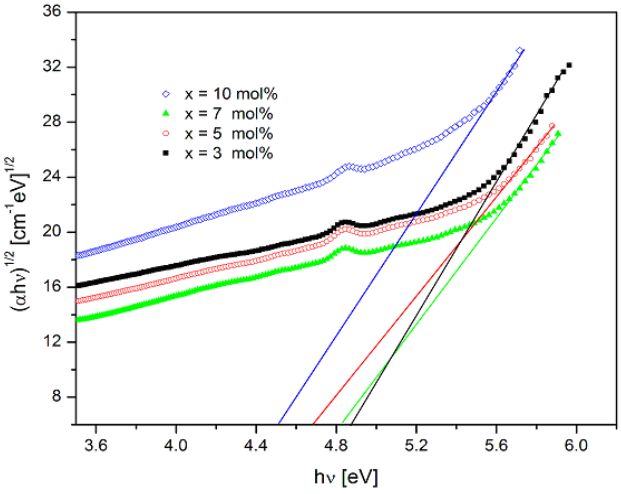

Fig. 4. The variation of $(\alpha h\nu)^{1/2}$ versus $h\nu$ for studied glass ceramics.

Table 2. N_4 and (E_g^{opt}) for studied glass ceramics.

x [mol%]	N_4	E_g^{opt} [eV]
0	0.444	-
3	0.422	4.88
5	0.452	4.68
7	0.465	4.82
10	0.473	4.51

CONCLUSIONS

The structural changes induced by heat treatment in the zinc–borate glasses doped with erbium ions are well reflected in their FTIR spectra. The FTIR data suggest the presence of both the BO_3 and BO_4 structural units, as well as of the ZnO_4 structural units in the studied glass ceramics. For all compositional range the threefold boron atoms are favored in the investigated glass system compared as with the fourfold ones. The UV-VIS absorption spectra of these glass ceramics show 10 absorption peaks which are due to the transitions from the $^4I_{15/2}$ ground state to the different excited state of Er^{3+} ions. From optical absorption spectra the E_g^{opt} have been calculated.

REFERENCES

[1] H.A. Elbatal, Z.S. Mandouh, H.A. Zayed, S.Y. Marzouk, G.M. Elkomy, A. Hosny, J. Non-Cryst. Solids (2012), doi: 10.1016/j.jnoncrysol.2012.05.026.

[2] D.U. Tulyaganov, M.J. Ribeiro, J.A. Labrincha, Ceram. Int., 28, 515 (2002).

[3] L.R. Pinckney, "Encyclopedia of Physical Science and Technology (Third Edition)", Elsevier Science Ltd, 2003, Pages 807-816.

[4] R. Lisiecki, E. Augustyn, W. Ryba-Romanowski, M. Żelechower, Opt. Mater., 33, 1630 (2011).

[5] J. Krogh-Moe, J. Non-Cryst. Solids, 1, 269 (1969).

[6] J. Zhong, P.J. Bray, J. Non-Cryst. Solids, 111, 67 (1989).

[7] R. Stefan, E. Culea, P. Pascuta, J. Non-Cryst. Solids, 358, 839 (2012).

[8] L. Koudelka, P. Mośner, Mater. Lett., 42, 194 (2000).

[9] E. Mansour, G. El-Damrawi, Physica B, 405, 2137 (2010).

[10] G.P. Singh, S. Kaur, P. Kaur, S. Kumar, D.P. Singh, Physica B, 406, 1890 (2011).

[11] S.D. Patil, V.M. Jali, R.V. Anavehar, Bull. Mater. Sci., 31, 631 (2008).

[12] A. Moguš-Milanković, L. Pavić, S.T. Reis, D.E. Day, M. Ivanda, J. Non-Cryst. Solids, 356, 715 (2010)

[13] G. Naga Raju, M. Srinivasa Reddy, K.S.V. Sudhakar, N. Veeraiah, Opt. Mater., 29, 1467 (2007).

[14] L. Zhou, H. Lin, W. Chen, L. Luo, J. Phys. Chem. Solids, 69, 2499 (2008).

[15] S. Tanabe, J. Alloys Compd., 408-412, 675 (2006).

[16] G. Lakshminarayana, J. Qiu, M. G. Brik, G. A. Kumar, I. V. Kityk, J. Phys.: Condens. Matter. 20, 375104 (2008).

[17] I. Jlassi, H. Elhouichet, S. Hraiech, M. Ferid, J. Lumin., 132, 832 (2012).

[18] S. Rada, P. Pascuta, L. Rus, M. Rada, E. Culea, J. Non-Cryst. Solids, 358, 30 (2012).

[19] K. El-Egili, Physica B. 325, 340 (2003).

[20] P. Pascuta, J. Mater. Sci.: Mater. Electron., 21, 338 (2010).

[22] W.F. Krupke, J. B. Gruber, J. Chem. Phys., 41, 1225 (1964).

[23] H.S. Liu, T.S. Chin, S.W. Yung, Mater. Chem. Phys., 50, 1 (1997).

[24] E. Mansour, G. El-Damrawi, Physica B, 405, 2137 (2010).

[25] J.F. Ducel, J.J. Videau, M.Couzi, Phys. Chem. Glasses, 34, 5 (1993).

[26] P. Pascuta, D. Maniu, I. Ardelean, Int. J. Mod. Phys. B, 18, 1651 (2004).

[27] S.G. Motke, S.P. Yawale, S.S. Yawale, Bull. Mater. Sci., 25, 75 (2002).

[28] I. Ardelean, R. Lungu, P. Pascuta, J. Mater. Sci.: Mater. Electron., 18, 837 (2007).

[29] C. Rajyasree, D. Krishna Rao, J. Non-Cryst. Solids, 357, 836 (2011).

[30] I. Ardelean, P. Pascuta, Mater. Lett., 58, 3499 (2004).

[31] E. I. Kamitsos, M. A. Karakassides, G.D. Chyssikos, J. Phys. Chem., 91, 1073 (1987).

[32] M.Abo-Naf, F.H.El. Batal, M.A.Azooz, Mater. Chem. Phys., 77, 846 (2002).

[33] A. Kumar, S.B. Rai, D.K. Rai, Mater. Res. Bull., 38, 333 (2003).

[34] P. Pascuta, L. Pop, S. Rada, M. Bosca, E. Culea, J. Mater. Sci.: Mater. Electron., 19, 424 (2008).

[35] E.A. Davis, N.F. Mott, Phil. Mag., 22, 903 (1970).

STUDIA UBB PHYSICA, Vol. 57(LVII), 1, 2012, pp. 67 - 75
(RECOMMENDED CITATION)

EPITAXIAL TiN THIN FILMS GROWN ON BIAXIALLY TEXTURED Ni-W SUBSTRATES

R.A. PATO[1,*], M.S. GABOR[1], T. PETRISOR Jr.[1], G. NEGREA[1], T. PETRISOR[1]

ABSTRACT. In this paper we present a detailed structural study of epitaxial TiN thin films deposited on biaxially textured Ni- 5%at.W (NiW) substrates by reactive magnetron sputtering. NiW substrates are used as a base material in coated conductors manufacturing. TiN is used as a buffer layer between NiW and YBCO. Structural investigations were carried out using X-ray diffraction. Based on X-rays diffraction analysis it was concluded that the TiN film grew epitaxially on NiW substrates.

Keywords: titanium nitride, thin films, epitaxy, sputtering deposition

INTRODUCTION

Titanium Nitride (TiN) coatings prepared by physical vapor deposition (PVD) are increasingly used in various applications such as cutting tools, microelectronics, artificial jewelry, diffusion barriers etc. Due to their excellent properties, such as extreme hardness (~ 2300 HV), low electrical resistivity, high wear and corrosion resistance, high thermal and chemical stability [1-5]. Moreover, these coatings are of interest because they exhibit a number of properties similar to metals (eg. electrical conductivity), while retaining characteristics found in insulating materials (covalent bonding, hardness, and a high melting point) [6]. In sputtering deposited TiN films, the properties can be largely modulated by varying the sputtering conditions, such as reactive gas pressure, total pressure and substrate temperature.

Therefore, it is interesting to study the effect of the deposition parameters on the properties of the TiN thin films.

In this paper, TiN epitaxial thin films deposited on Ni-W substrates were studied. The TiN buffered NiW substrates are of practical interest for the $YBa_2Cu_3O_7$ (YBCO) based coated conductors fabrication. Lately, many efforts have been focused

[1] Technical University of Cluj–Napoca, Str. Memorandumului 28, 400114, Cluj-Napoca, Romania
* Robert.Pato@phys.utcluj.ro

on YBCO coated conductors because YBCO is the best candidate for the second generation superconducting cables [7].YBCO coated conductors are composed of a bi-axially textured YBCO film deposited on a metallic substrate with intermediate buffer layers. These buffer layers have three essential functions: (i) firstly, to act as a chemical barrier preventing the diffusion of the metallic elements into YBCO; (ii) secondly, preventing the oxidation of the metallic substrate during the YBCO film processing since it involves an annealing at high temperature under oxygen atmosphere; (iii) finally, to transfer the texture from the substrate to YBCO. The bi-axial texture is essential for YBCO in order to have a high critical current density (Jc) capacity that strongly depends on the crystallographic orientation [8].

EXPERIMENTAL DETAILS

The TiN coatings were deposited by the DC-reactive magnetron sputtering method. The system is provided with water cooled circular planar magnetron sputtering sources. The diameter of the Ti target is 50.8 mm and it has a thickness of 3.18 mm. Argon, with a purity of 99.999% was used as sputtering gas, and nitrogen with a purity of 99.999% was used as reactive gas. Both inert argon gas flow and nitrogen reactive gas flow were controlled by Qualiflow AFC 50.00 mass flow controllers. The pressure chamber was monitored by a convection vacuum gauge and measured by InstruTech vacuum gauge controller. Prior to deposition the substrates were ultrasonically cleaned with acetone and isopropyl alcohol.

After mounting the substrate on a resistive heater, the pressure of the sputtering chamber was pumped down to 1.0×10^{-6} Torr. Argon (20 sccm) and nitrogen (1.2 sccm) gas were next introduced into the chamber and the required pressure (2×10^{-2} Torr) was reached. Subsequently, the nitrogen gas flow was shut off and the target was pre-sputtered in argon atmosphere for about 10 min in order to remove the contamination from the target surface. After pre-sputtering, the nitrogen gas was again introduced into the chamber and the reactive sputtering process starts at 2×10^{-2} Torr. The operating pressure, the argon and the nitrogen flow, as well as the cathode current (340 mA) were kept constant during the deposition.

The crystalline structure analysis of the titanium nitride layers was performed by X-Ray diffraction (XRD) using a Brucker D8 High Resolution XRD with a copper anode. A high resolution field emission LEO 1525 scanning electron microscope (SEM) is used for the microstructural characterization. The scanning electron microscope is equipped with an Electron Back Scattered Diffraction (EBSD) system that allows resolving the local crystallographic orientations in the range of 100nm. The AFM measurements were performed on a Veeco Dimension 3100 instrument.

RESULTS AND DISCUSSION

TiN layer thickness determination

The thickness of the films was determined by ex-situ X-Ray reflectometry (XRR) measurements. The experimental curves were tilted with the theoretical ones, using the Leptos (Brucker) software, based on the Parrot formalism. The results indicate a deposition rate of 163 nm in 20 min for our specific growth conditions.

TiN films grown on Biaxially Textured NiW Substrates

The High Resolution X-Ray diffraction patterns recorded for the films deposited between 400-700°C (fig. 1) evidenced only the presence of the (200) reflections belonging to the substrate and the film. This indicates that the film grows with a (h00) type texture. The ϕ-scan type measurement recorded for the (311) substrate and film reflections demonstrate that the film is fully epitaxially grown on the NiW substrate, with the following epitaxial relation TiN[001](100)//NiW[001](100) (shown in fig. 2). Other phases and orientations were not observed in the limit of the measurement accuracy, except for the film deposited at 700 °C forming the (111)TiN polycrystalline peak at 36.5° was identified (fig. 1).

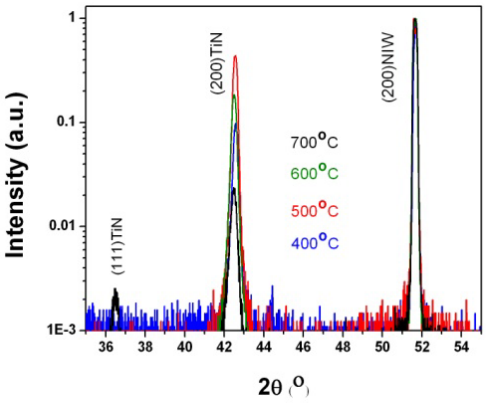

Fig. 1. X-Ray diffraction patterns at different deposition temperatures

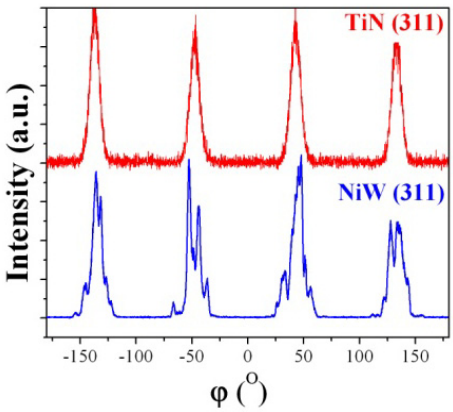

Fig. 2. ϕ-scan around the (311) peak on NiW and TiN

The influence of the deposition temperature on the lattice parameter

The out-of-plane lattice parameter was calculated using the angle position of the (200) TiN peak. The obtained values are close to the bulk one and show a temperature dependence. The increase of the lattice parameter is a consequence of the increase of the deposition temperature (fig. 3). The lattice mismatch between the film and the substrate is calculated using formula

$$f = \frac{a_0(substrate) - a_0(film)}{a_0(substrate)} = -20 \quad (1)$$

The results indicate a negative value for the f, suggesting that the film is under compression.

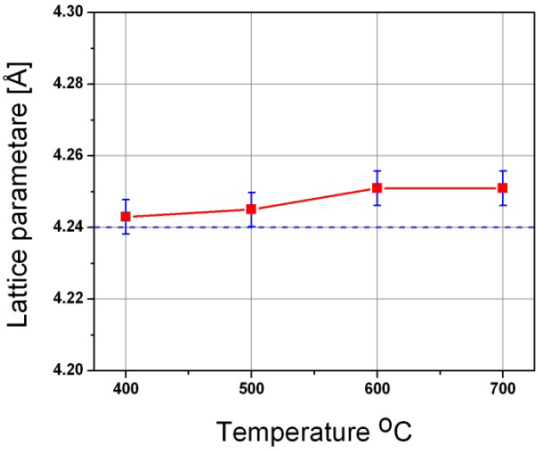

Fig. 3. Lattice parameter dependence on temperature, the dash line represents the TiN lattice parameter (for the bulk form)

The influence on the deposition temperature on the mean grain size

The grain size of the TiN film increases with the increase of temperature up to 600 °C and a temperature higher than 700 °C the grain size decreases (Fig. 4). The mean grain size was evaluated by means of Scherrer formula [1]:

$$D = \frac{0{,}9\lambda}{B\cos\theta} \quad (2)$$

where, D is the grain size [nm] measured in the direction perpendicular to the surface, λ is the wavelength of CuKα radiation, B is the FWHM (full width at half maximum) of the diffraction profile in rad, and θ is the Bragg diffraction angle corresponding to the considered (200) diffraction peak.

The TiN grain size dependence on the NiW substrate temperature is shown in fig. 4. We can observe that at the temperature of 400 and 500 °C, respectively is there a slight increase in the crystallite size. While from 500 °C to 600 °C there is a sharp increase, and then a sudden drop down to 700 °C. It is known that with the increase of the deposition temperature the crystallites size also increases. The temperature limits between epitaxial and polycrystalline growth is registered at 600 °C.

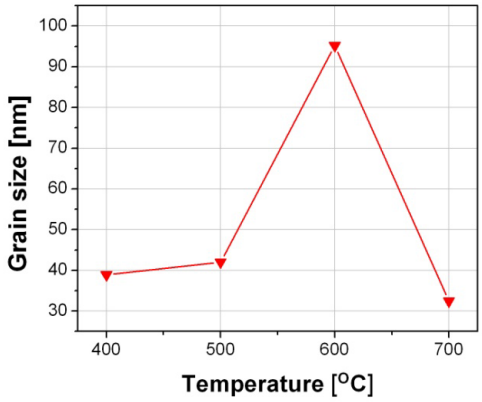

Fig. 4. Grain size versus temperature

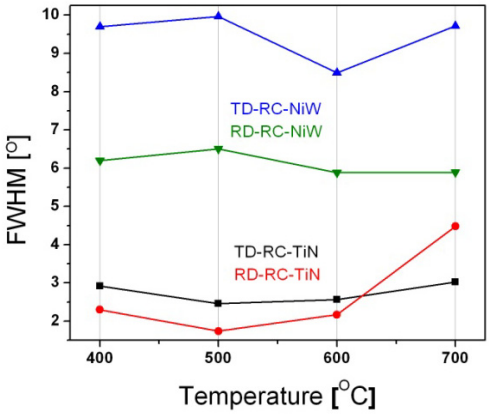

Fig. 5. FWHM of the (200)TiN with respect to the deposition temperature

From the X-ray diffraction pattern presented in fig. 1 results that a polycrystalline phase with the (111)TiN orientation is present at temperature of 700 °C.

The influence of the deposition temperature on epitaxy

In order to characterize the out-of-plane crystallite orientation distribution of the TiN films we have performed Rocking Curve (R.C.) measurements around the (200)TiN reflection. The RC measurements were carried out on two different azimuths corresponding to the substrate rolling direction (RD) and transversal direction (TD). We have performed measurements for these particular orientations because the substrates were cold rolled, and -as a consequence- the crystallites are elongated on the RD. Therefore, the degree of orientation along the RD is much higher than along the TD relative to the TD. The films retain a similar behavior although the overall orientation degree is higher. In fig. 5 it is shown the evolution of the FWHM of the RC with the deposition temperature.

Using the X-Ray diffraction measurements we can conclude that the optimal temperature for the epitaxial deposition of TiN on NiW substrates is 500°C because this is the highest deposition temperature at which the grain size is the smallest and the epitaxial structure is preserved without any other phases and orientations. Also, the film is less compressed at this temperature.

To demonstrate that the TiN film deposited at 500 ºC shows only (h00) type reflections, an EBSD analysis was performed on the film surface, on the rolling direction and transverse on the rolling direction. Electron backscatter diffraction patterns enable the observation of larger areas and the collection of statistically significant data on the crystal orientations.

The EBSD crystallites orientation color key map is presented in fig. 6. Figure 7 presents the EBSD pattern quality map of the TiN film deposited at 500 ºC. The mapping of the crystallographic orientation have revealed that the orientation with the (h00) type reflection assigned to the red color, is dominant in proportion of about 95% of the total scanned area.

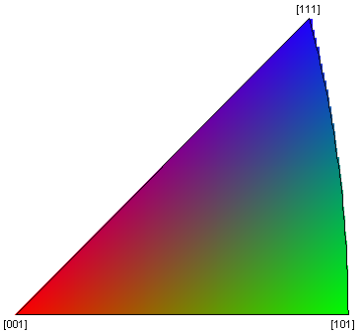

Fig. 6. Orientation color key map

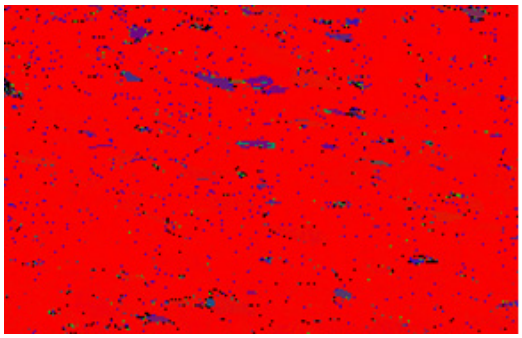

Fig. 7. EBSD pattern quality map of the TiN film deposited at 500 ºC on biaxially textured NiW substrates

Thickness determination for the TiN films deposited on NiW

Following we studied the influence of the thickness on the crystallites properties of the film deposited at the optimized temperature of 500°C. The XRD patterns indicate that the film retains the epitaxial characteristics for thicknesses up to 520 nm. No sign of other phases and orientations were observed (Fig. 8).

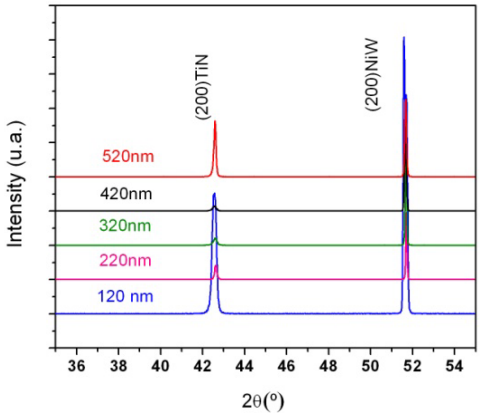

Fig. 8. X-Ray diffraction pattern versus deposition thicknesses of the TiN film

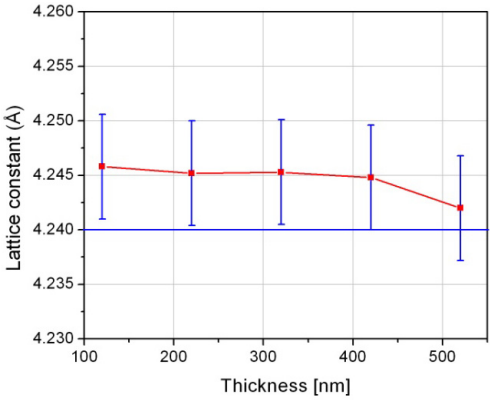

Fig. 9. Lattice constant versus film thickness

The lattice constant shows no evolution with the film thickness and remains close to the bulk value. The lattice parameter values were calculated with error bars that show theoretical lattice parameter values close to the experimental one (Fig. 9). The dependence of the Full Width at Half Maximum (FWHM) of the RC on the film thickness of the deposited TiN film is shown in fig. 10. The films retain a similar behavior although the overall degree orientation is higher.

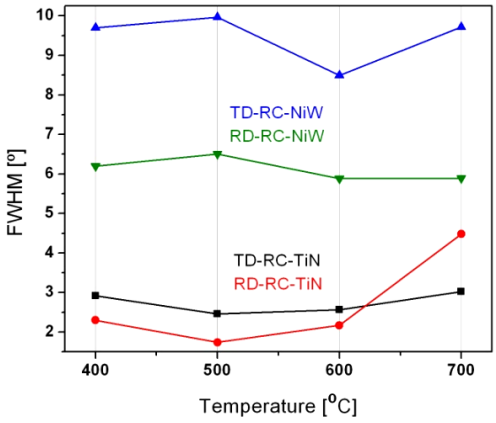

Fig. 10. Out-of-plan orientation versus film thickness

The influence of the temperature on the morphology of the TiN films deposited on NiW substrates

The influence of deposition temperature on the TiN films morphology is presented in fig. 11. The AFM images represent the result of the analyses for the films deposited at 400, 600 and 700 ºC. The right column contains the crystallite profiles of the TiN films, while the topographic images are presented in the left column. From the analyses of these profiles, one can observe the increase of the crystallite size. At the temperature of 400 ºC, the surface roughness is 0.9 nm (RMS).

This film exhibits a lower crystallization degree which can be also associated with the result of the X-Ray diffraction analysis, where one can observe a lower intensity of the (200) peak belonging to TiN, in comparison with the other deposition temperatures of the film. The increase of the crystallite size with a certain orientation, can be associated with the X-Ray diffraction pattern corresponding to the film deposited at 700 ºC, where one can observe the presence of a polycrystalline peak, corresponding to the (111)TiN orientation at 36.5^{o}.

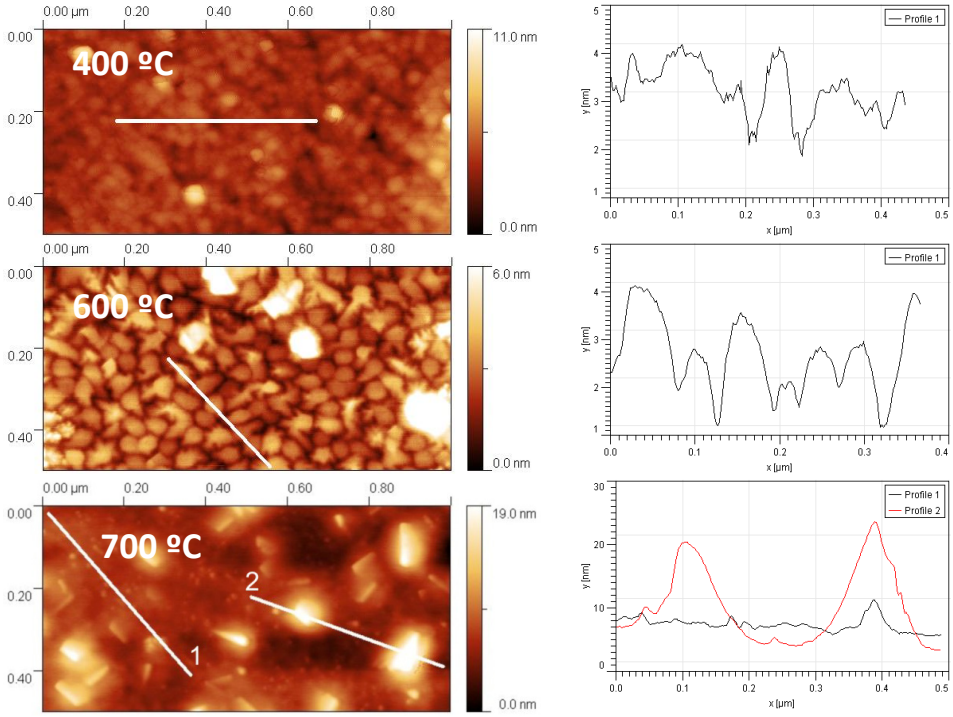

Fig. 11. AFM images of the TiN films deposited at different temperatures

Fig. 12 presents the roughness value and the medium dimension of the crystallites for each deposition temperature. It can be observed that the roughness value and the crystallite dimensions increase with the increase of the deposition temperature. At 700 ºC the roughness has the highest value, mainly because of the (111) oriented crystallites that can be observed in fig. 11 and in the X-ray diffraction pattern shown, as well (fig. 1).

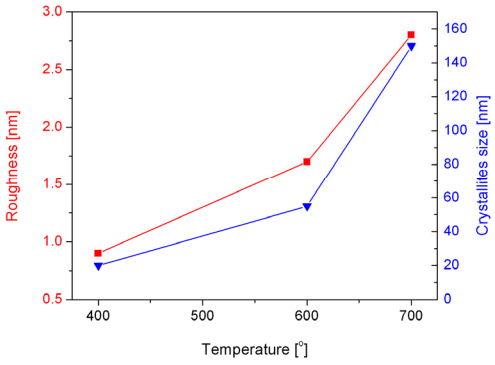

Fig. 12. Roughness and crystallite size dependence on the deposition temperature

CONCLUSIONS

The optimization study regarding the epitaxial deposition by DC sputtering of the TiN films on NiW biaxially textured substrates has revealed the following:

1. The optimal temperature for depositing epitaxial TiN films on NiW substrates is 500°C since the films deposited at this temperature have the best out-of-plane and in-plane orientation with the FWHM of the ω-scan and the φ-scan at about 1.74^{o} and 8.68^{o}, respectively. This is the highest deposition temperature for which the grain size is the smallest and the epitaxial structure is preserved without any sign of other phases and orientations.
2. The epitaxy is preserved for the film thicknesses up to 520 nm.
3. The out-of-plane lattice parameter of the films deposited at temperature higher than 500 ºC is larger for the bulk material, indicating that the film exhibits an in-plane compression.
4. At the optimal deposition temperature of 500 ^{o}C the roughness has the lowest value.
5. The roughness value and the crystallite dimensions increase with the increase of the deposition temperature (400-700 °C).

ACKNOWLEDGMENTS

This work was supported by CNCSIS –UEFISCSU, project number PNII – IDEI code 100/2010.

REFERENCES

[1] Grips WVK, Ezhil Selvi V, Barshilia HC, Rajam KS (2006) Electrochim Acta 51:3461

[2] Souto RM, Alanyali H (2000) Corr Sci 42:2201

[3] Kim TS, Park SS, Lee BT (2005) Mater Lett 59:3929

[4] Dobrzanske LA, Adamiak M (2003) J Mater Process Technol 133:50

[5] Hogmark S, Jacobson S, Larsson M (2000) Wear 246:20

[6]L.E. Toth, Transition Metals Carbides and Nitrides, Vol 7, Academic press, New York, 1971

[7] A.P. Malozemoff, Second Generation HTS Wire: An Assessment, http://www.amsuper.com/products/htsWire/Techpapers1.cfm.

[8] D. Dimos, P. Chaudhari, J. Mannhart, Phys. Rev. B 41 (1990) 4038.

STUDIA UBB PHYSICA, Vol. 57(LVII), 1, 2012, pp. 77 - 85
(RECOMMENDED CITATION)

STRUCTURAL PROPERTIES OF POROUS COMPOSITES BASED ON TiO_2 AND Ag NANOPARTICLES AND THEIR CAPABILITY TO DETECT WATER POLLUTANTS BY SERS

A. RADU[1], I.J. HIDI[1], V. IANCU[1], L. BAIA[*,1,2] AND M. BAIA[1,2]

ABSTRACT. Nanocomposites based on TiO_2 loaded with Ag nanoparticles obtained via sol-gel method were investigated by means of Raman spectroscopy and sorption measurements. Furthermore, the detection capability of trace amounts of congo red and crystal violet molecules from aqueous solutions was also tested by employing Surface Enhanced Raman Spectroscopy (SERS). It was found that upon thermal treatment the crystallinity degree of the samples increases, the surface area and pore volumes decrease which explains the lower detection limits of the annealed samples. More exactly, in the case of untreated sample a concentration of 10^{-7} M for crystal violet and 10^{-5} M for congo red was detected, while after thermal treatment the less porous samples led to the detection of 10^{-5} M for crystal violet and 10^{-4} M for congo red.

Keywords: nanocomposites, Raman spectroscopy, sorption measurements, SERS, water pollutants.

INTRODUCTION

One of the oldest problems of civilized life, still unsolved today is pollution. Among all types of pollution human society is responsible of, water contamination caused by hazardous organic chemicals employed in industry and agriculture is considered nowadays a very serious issue [1-4]. Accordingly, a growing scientific interest has been directed towards both stopping the growth of this phenomena and solving it [5-10]. As the material science developed, steps were made in the direction of nanotechnology and through it to the possibility of fighting pollution [6-7]. That is mostly because manipulation at nano-scale enables the realization of devices

[1] Faculty of Physics, Babeş-Bolyai University, 1 Kogălniceanu str., 400084 Cluj-Napoca, Romania
* lucian.baia@phys.ubbcluj.ro
[2] Institute for Interdisciplinary Research in Bio-Nano-Sciences, Babes-Bolyai University, Treboniu Laurian Street 42, 400271, Cluj-Napoca, Romania

capable of detecting trace amounts of pollutants when correlated with surface-enhanced Raman spectroscopy (SERS) [6-10]. The choice of SERS is based on the fact that it can actually act as a molecular "fingerprint" and allows simultaneous determination of various trace analytes in a complex mixture without extraction and separation steps [5,8]. For the realization of the sensors' matrix the most studied material is titanium dioxide, as this material's properties allow the development of cheap, bio-friendly, nano-structured composites [11]. Finally, the connection between titania matrix and SERS detection is achieved by the incorporation of noble metal nanoparticles into the matrix [8,12].

In this study we propose to prepare porous nanoarchitectures based on TiO_2 aerogel and Ag colloidal particles, to investigate their structural and morphological properties and to test their capability to detect, by SERS, contaminant species adsorbed from an aqueous solution on the metallic nanoparticles surface. The composites detection efficiency was established by using crystal violet and congo red as test molecules.

EXPERIMENTAL

Sample preparation

TiO_2 gels were prepared in accordance with the acid-catalyzed sol–gel method [17-18], using titanium isopropoxide ($Ti[OCH(CH_3)_2]_4$), nitric acid (HNO_3, 70%), ethanol (EtOH, 92%) and distilled water (H_2O) in molar ratio of 1/0.08/21/3.67. The obtained gels were than aged for 21 days [12] and immersed into different volumes of silver colloidal solution.

For the silver colloidal solution preparation the Creighton method [16] was used. That is, 10 ml of 10^{-3} M silver nitrate ($AgNO_3$) was added dropwise, with vigorous stirring, to 30 ml of 10^{-3} M of sodium borohydride ($NaBH_4$). The solution was then cooled to ice temperature. In the next step, the dimensions of the silver nanoparticles in the colloidal solution were evaluated and found to be of 16-20 nm by means of UV–vis spectrophotometry and Transmission electron microscopy (TEM – see **Fig. 1**).

As already mentioned, the aged TiO_2 gels were immersed into two different volumes (50 cm^3 and 300 cm^3) of the as prepared silver colloidal solution and maintained there for three days. Accordingly, two samples of different silver nanoparticle concentration were obtained. They were denoted M1 and M2, respectively. The obtained samples were than washed with ethanol (92%), kept in ethanol (92%) for 12 hours and dried under supercritical conditions, using liquid CO_2 (T = 313K and p = 95.23 atm). In order to remove the organic residues they were further subjected to a two steps thermal treatment. First, the temperature was increased by 1°C/min till 140°C, followed by 4°C/min till 500°C. The samples were then maintained at

500 °C for 30 minutes. This temperature was chosen after a close investigation of the TGA/DTA diagrams of the samples (not shown here). The newly obtained samples were denoted AM1 and AM2.

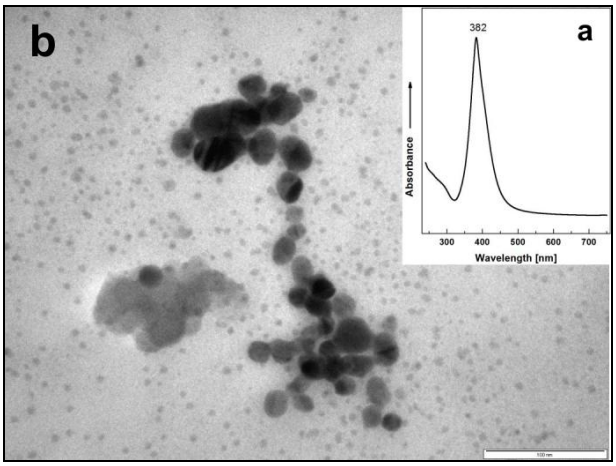

Fig. 1. a) The UV–vis spectrum of the Ag nanoparticle colloidal solution.
b) TEM image selection of the silver colloidal solution - scale of 100 nm.

Sample measurements

The surface area of the as prepared samples was determined by the the Brunauer-Emmett-Teller (BET) 3 parameter method, in a partial pressure range of 0.05<P/P0<0.3. The nitrogen adsorption was carried out at 77 K. Before each measurement the samples were heat cleaned at 333 K for 2 h. The total pore volume (VTP) was obtained from the N_2 adsorption isotherm at a partial pressure of 0.98. The mesoporosity of the samples was required using the Barret-Joyner-Halenda (BJH) treatment.

The optical absorption spectra of the silver colloidal suspension and those of the two pollutants were recorded with a Jasco V-530 UV–Vis spectrophotometer. A JEOL JEM 1010 transmission electron microscope was used to further determine the silver nanoparticles diameter.

The capability of the composites to detect various pollutant species adsorbed on Ag nanoparticles surface was established by means of SERS. The contaminants investigated for this purpose were crystal violet and congo red. Accordingly, aqua solutions of various, predetermined concentrations of the two pollutants were prepared. In a next step, small amounts of each composite were immersed for 2-3 minutes into those aqueous solutions, than left to dry out at room temperature. Finally, SERS spectra were recorded with a Horiba Jobin-Yvon LabRam Raman Confocal Microscope. While performing the measurements the microscope was equipped with

a 50x/0.5 microscope objective and a 300 lines/mm grating. In recording the spectra, the 532 nm laser line with a spectral resolution of around 12 cm^{-1} was employed. The laser power used for recording the spectra belonging to crystal violet was of 0.5 mW, while for the spectra belonging to congo red a power of 1.25 mW was applied. In order to assure the measurements reproducibility SERS spectra were collected from different points located on the composites surface and inside the samples. All spectra was baseline corrected with OPUS 6.5 software.

RESULTS AND DISCUSSION

The final step of the samples obtaining process consisted of a thermal treatment intended to remove the organic residues. Besides this, annealing had yet another purpose, namely, the formation and stabilization of an anatase-like structure. A close investigation of the Raman spectra illustrated in **Fig. 2** reveals information about both stated objectives of annealing. First, analyzing the untreated sample's spectra, one observes the presence of certain bands specific for the organic residues. That is, the bands in the 830–960 cm^{-1} spectral domain are specific for C–N bending vibrations [13], those in the 1020–1160 cm^{-1} wavenumber range are characteristic for C–H bending vibrations [13-14], the one around 1446 cm^{-1} reveals the presence of C–C groups [14] and the signals between 2840 and 2990 cm^{-1} are specific for C–H stretching vibrations [13-14]. It is easy to observe that none of the peaks mentioned above can be identified in the annealed sample's spectra. This implies that the first objective of the thermal treatment was achieved. By further analyzing the spectra in **Fig. 2** one notices that the bands around 144, 186, 386, 512 and 638 cm^{-1} can be observed for both treated and untreated samples. Moreover, they become more intense and well defined for the annealed samples. All those bands are characteristic for the anatase crystalline structure of titania [15-16]. According to the space group classification, anatase belongs to D_{4h} group, having an irreducible representation of six optical modes: E_g, E_g, B_{1g}, A_{1g}, B_{1g} and E_g [15]. Taking into consideration that the Raman band centered at 512 cm^{-1} represents the convolution of the two bands specific for B_{1g} (512 cm^{-1}) and A_{1g} (519 cm^{-1}), all six optical modes belonging to anatase can be identified. The stated observations can be concluded by saying that the second propose of the annealing was also achieved as anatase-like structure is clearly identified in the Raman spectra presented in **Fig 2**.

Further on, the existence of a porous structure is evidenced by the values obtained from the BET surface area measurements presented in **Table 1**. Both the specific surface area and the pore volume reach higher values for the untreated samples. **Fig. 3** shows nitrogen adsorption and desorption isotherms of the investigated samples. According to IUPAC classification [17] the sample exhibit type IV isotherms, characteristic for the samples which contain meso and micro pores with a non-perfect cylindrical shape.

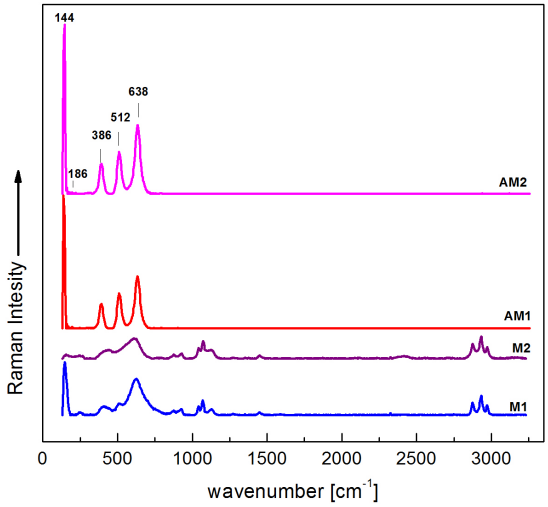

Fig. 2. Selection of Raman spectra belonging to untreated and thermally treated sample.

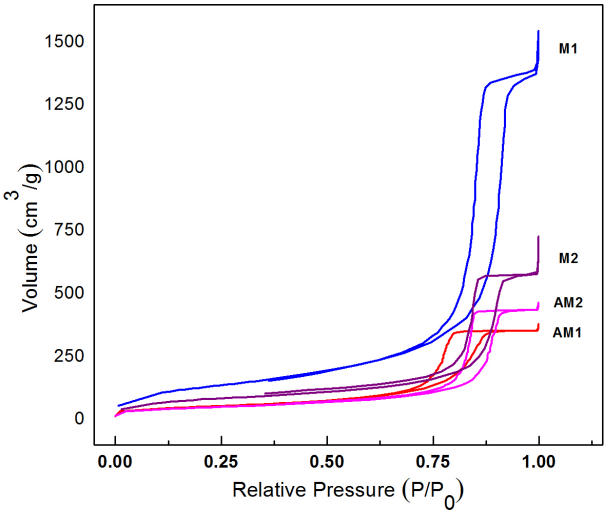

Fig. 3. Nitrogen adsorption isotherms belonging to untreated and thermally treated samples.

The study was further focused on the assessment of the porous composites capability to detect trace amounts of various pollutant species adsorbed on Ag nanoparticles surface. The target pollutants chosen were crystal violet and congo red. **Fig. 4** shows UV-vis spectra recorded on both pollutants. By looking at the UV-vis spectra of the pollutants, one remarks that the one belonging to crystal violet exhibits an intense and broad electron absorption band around 589 nm, while that

belonging to congo red reveals three large peaks. Among them, the smaller peak in the useable ultraviolet–visible range is centered at 340 nm and a larger peak at 496 nm. Considering the one around 496 nm for congo red, crystals' violet absorption peak being around 589 nm and having in mind the laser excitation wavelength used throughout the SERS experiments (532 nm), one can anticipate that pre-resonant and resonant SERS signals (SERRS) will be recorded for the detection of crystal violet and congo red, respectively.

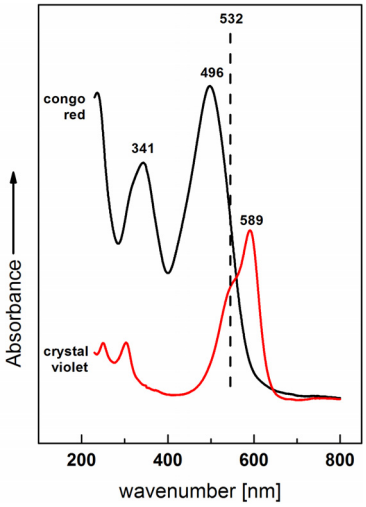

Fig. 4. The UV–vis spectrum of crystal violet and congo red as indicated. The laser excitation line is also indicated.

An inspection of the Raman spectrum of crystal violet in **Fig. 5** led to the choice of three main bands as representative for the further identification of crystal violet's presence in the SERRS spectra: the bands around 1612 cm^{-1}, due to the stretching vibrations of C–C from phenyl rings, and those around 1366 and 1175 cm^{-1}, attributed to the C–N stretching and C–H bending vibrations, respectively [8-9]. As for congo red, the spectra in **Fig. 6** led to the choice of the following fingerprint bands: the bands around 1155 cm^{-1}, due to the stretching vibrations of φ-N_{Azo}, 1353 cm^{-1} and 1593 cm^{-1} attributed to the naphthyl ring and phenyl ring vibrations, respectively [10,18]. Next, aqueous solutions of various, predetermined concentrations of pollutants were prepared and the detection sensitivity of the investigated porous composites was established. The results are presented in **Table 1**. As one can observe, best detection sensitivity belongs to the M1 untreated sample, namely, around 10^{-7} M for crystal violet and 10^{-5} M for congo red. After annealing, the detection limit of both samples were lower. More exactly, both AM1 and AM2 were capable to detect pollutants concentrations around 10^{-5} M for crystal violet and 10^{-1} M for congo red.

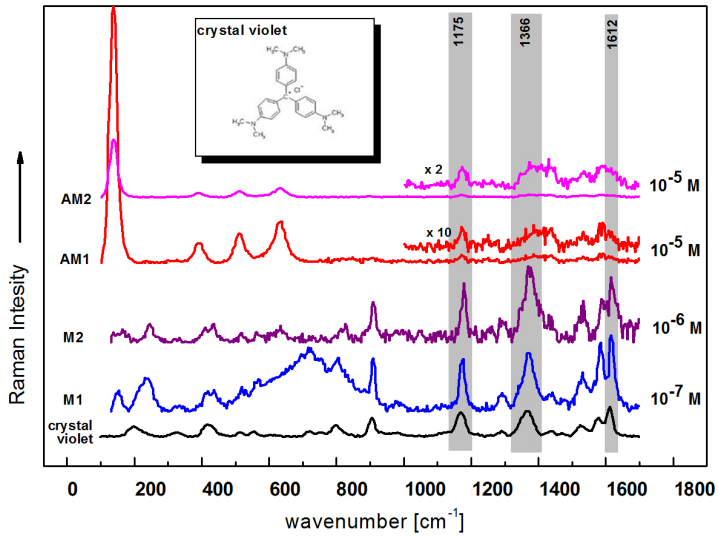

Fig. 5. Raman and selected SERRS spectra obtained after the crystal violet adsorption on the porous composites. The pollutant's concentrations and structural formula are also indicated.

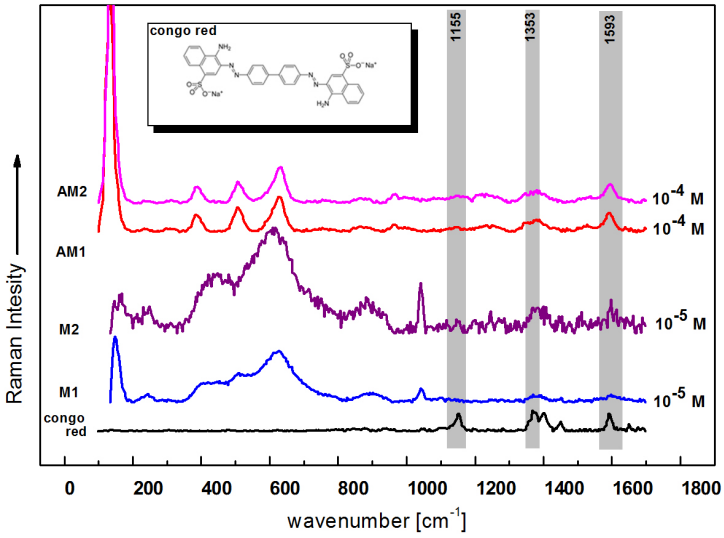

Fig. 6. Raman and selected SERRS spectra obtained after the congo red adsorption on the porous composites. The pollutant's concentrations and structural formula are also indicated.

Table 1. BET surface areas and pollutant detection limit for the investigated samples.

Sample	S_{BET} [m^2/g]	Pore volume (BET) [cm^3/g]	Detection limits [M]	
			Crystal violet	Congo red
M1	478.27	2.0905	10^{-7}	10^{-5}
M1	302.61	0.8838	10^{-6}	10^{-5}
AM1	181.77	0.5603	10^{-5}	10^{-4}
AM2	169.99	0.6779	10^{-5}	10^{-4}

As already mentioned, SERRS spectra were recorded from different points located on the composites surface and inside the samples. This was possible because the sol-gel synthesized materials have two particularly important characteristics: they encapsulate silver nanoparticles into the TiO_2 matrix and they facilitate liquid diffusion and its adsorption inside the porous structure. As the samples were immersed in water diluted pollutants, upon samples drying, the contaminants could be detected at different points inside the material. Analyzing the experiment's results, it was found that the detection limits depend on whether the samples were thermally treated or not. Considering that after annealing the total pore volume and surface area decreases one can conclude that the pore connectivity degrades and as a consequence the pollutants molecules could no longer diffuse and be adsorbed inside the porous structure. Accordingly, the lower values of the detected pollutants' concentration do not come as a surprise. Even so, the fact that they could be detected on the samples' surface and at different points inside it makes this type of sol-gel synthesized materials attractive for water treatment applications. Moreover, the encapsulation of silver nanoparticles in the TiO_2 matrix leads to the realization of composites that are particularly stable in time, which is benefic for the stated applications.

CONCLUSIONS

In the present work various types of porous nanoarchitectures based on TiO_2 aerogels and Ag colloidal particles were studied in terms of their capability of quickly detecting small concentrations of various pollutant species adsorbed on the noble metal surfaces, by means of SERS. The composites prepared presented an anatase-like structure and have great detection efficiency, most probably due to a good dispersion of Ag nanoparticles inside the aerogel matrix. The detection limits were found to be of around 10^{-7} M for crystal violet and 10^{-5} M for congo red, respectively. After heat treatment, even if the composites become less porous, as reported by sorption measurements, they are able to detect contaminant species. However the detection limits were lower: 10^{-5} M for crystal violet and 10^{-4} M for congo red. The obtained results showed the real potential of the prepared porous composites to be used in development of new SERS-based sensors.

ACKNOWLEDGMENTS

This work was supported by CNCSIS-UEFISCSU, project number PN II-RU TE 81/2010. The authors gratefully acknowledge Prof. Dr. J. Popp from the Physikalische Chemie Institut of Jena for providing access to the Raman equipment.

REFERENCES

[1]. L.J. Bao, K.A. Maruya, S.A. Snyder, E.Y. Zeng, *Environ. Pollut.*, 163, 100 (2012).

[2]. C. Barba-Brioso, J.C. Fernández-Caliani, A. Miras, J. Cornejo, E. Galán, *Mar. Pollut. Bull.*, 60, 1259–1269 (2010).

[3]. J. Ma, Z. Ding, G. Wei, H. Zhao, T. Huang, *J. Environ. Manage.*, 90, 1168 (2009).

[4]. R.H. Foy, S.D. Lennox, R.V. Smith, *Water Res.*, 35, 3004 (2001).

[5]. J.C.S. Costa, A.C. Sant'Ana, P. Corio, M.L.A. Temperini, *Talanta*, 70, 1011 (2006).

[6]. L. Zhang, M. Fang, Nano Today 5, 128 (2010).

[7]. B. Sharma, R.R. Frontiera, A.I. Henry, E. Ringe, R.P. Van Duyne, *Mater. Today*, 15, 16 (2012).

[8]. M. Baia, G. Melinte, L. Barbu-Tudoran, L. Diamandescu, V. Iancu, V. Cosoveanu, V. Danciu, L. Baia, *J. Phys. Conf. Ser.*, 304, (2011) 012059 doi: doi:10.1088/1742-6596/304/1/012059.

[9]. A. Kudelski, *Chem. Phys. Lett.*, 414, 271 (2005).

[10]. C.E. Bonancê, G.M. do Nascimento, M.L. de Souza, M.L.A. Temperini, P. Corio, *Appl. Catal., B*,69, 34–42 (2006).

[11]. K. Hashimoto, H. Irie, A. Fujishima, *Jpn. J. Appl. Phys.,* 44, 8269 (2005).

[12]. A. Fujishima, X. Zhang, D.A. Tryk, *Surf. Sci. Rep.*, 63, 515 (2008).

[13]. V. Krishnakumar, N. Jayamani, R. Mathammal, *Spectrochim. Acta, Part A*, 79, 1959 (2011).

[14]. M. Baia, L. Baia, W. Kiefer, J. Popp, *J. Phys. Chem. B*, 108, 17491 (2004).

[15]. Y.H. Zhang, C.K. Chan, J.F. Porter, W. Guo, *J Mater Res*, 13, 2602 (1998).

[16]. L. Baia, A. Peter, V. Cosoveanu, E. Indrea, M. Baia, J. Popp, V. Danciu, *Thin Solid Films,* 511, 512 (2006).

[17]. K.S.W. Sing, D.H. Everett, R.A.W. Haul, L. Moscou, R.A. Pierotti, J. Rouquerol, T. Siemieniewska, *Pure Appl. Chem*., 57, 603 (1985).

[18]. T.E. Sladewski, A.M. Shafer, C.M. Hoag, *Spectrochim. Acta*, *Part A*, 65, 985 (2006).

STUDIA UBB PHYSICA, Vol. 57(LVII), 1, 2012, pp. 87 - 92
(RECOMMENDED CITATION)

SPECTROSCOPIC STUDIES OF LACUNARY POLYOXOTUNGSTATES CERIUM (III) COMPLEXES BASED ON α-B-$[Bi^{III}W_9O_{33}]^{9-}$ UNITS

D. RUSU[1], D. MARE[2], C. BERINDEAN[2], A. UNGUREAN[2], O. BABAN[3], L. DAVID[2,*]

ABSTRACT. Two new large cerium complexes
(**1:** $K_{19}[(BiW_9O_{33})_4WO_2(H_2O)]_2Ce_3(H_2O)_8(Bi_4O_4)].48H_2O$ and
2: $K_{15}[Ce_2(H_2O)_2(BiW_9O_{33})(W_5O_{18})_2].21H_2O$ were synthesized and characterized by chemical analysis, FT-IR and UV-Vis spectroscopy in order to determine the coordination, the ordering of cation electronic levels and the local symmetry. Based on the FT-IR spectra of the complexes we estimated that the coordination take place through the cerium ions, forming trilacunary polyoxoanion compounds. The UV and Vis electronic spectra present bands assigned to the charge transfer metal-ligand. The spectroscopic investigations indicate a sandwich-type structure for the two complexes.

Keywords: polyoxometalates, heteropolyoxotungstates, FT-IR, UV-Vis.

INTRODUCTION

Polyoxometalates (POMs) are a unique class of inorganic metal-oxygen clusters. They consist of a polyhedral cage structure or framework bearing a negative charge which is balanced by external cations or may contain centrally located heteroatom(s) surrounded by the cage framework. Generally, suitable heteroatoms include group III-VI elements such as phosphorus, antimony, silicon and boron [1-3]. The framework of polyoxometalates comprises a plurality of metal atoms (addenda), which can be the same or different, bonded to oxygen atoms. Due to appropriate cation radius and good electron acceptor properties, the framework metal is substantially limited to a few elements including tungsten, molybdenum, vanadium, niobium and tantalum.

[1] University of Medicine and Pharmacy, Physical Chemistry Department, 8 Victor Babes str., 400012 Cluj-Napoca, Romania
[2] "Babes-Bolyai" University, Faculty of Physics, 1 Kogalniceanu str., 400084 Cluj-Napoca, Romania
[3] "Babes-Bolyai" University, Faculty of Chemistry, 11 Arany Janos str., 400028 Cluj-Napoca, Romania
* leontin.david@phys.ubbcluj.ro

Trivacant Keggin fragments of type $[\alpha\text{-B-}X^{III}W_9O_{33}]^{9-}$ (X-As, Sb, Bi) are suitable building blocks for synthesis of large polyoxotungstates. Species consist of two, three, four, six and twelve $[\alpha\text{-B-}X^{III}W_9O_{33}]^{9-}$ units linked by lanthanide cations in order to form new classes of material with a large anion cluster [4-9].

Two large cerium complexes **(1)** $K_{19}[(BiW_9O_{33})_4WO_2]Ce_3(H_2O)_8(Bi_4O_4)]\cdot 48H_2O$ and **(2)** $K_{15}[Ce_2(H_2O)_2(BiW_9O_{33})(W_5O_{18})_2]\cdot 21H_2O$ were synthesized and characterized by chemical analysis, UV-Vis and FT-IR spectroscopy.

EXPERIMENTAL

Physical-chemical measurements

Experimental chemical analysis was made by atomic absorption. The water amount was determined from the difference of initial and heated (at 120 ^{0}C, respectively calcination at 560 ^{0}C, for 30 minute) samples.

FT-IR spectra were taken with a Perkin-Elmer FT-IR 1730 spectrophotometer over KBr solid samples in 4000-400 cm^{-1} range.

UV and visible electronic spectra were recorded in aqueous solutions (bidistilated water), having the $5\cdot10^{-5}$ M concentration for the UV field and the $5\cdot10^{-3}$ M concentration for the Vis analysis, using a Jasco V-670 spectrophotometer.

Synthesis of the complexes

The reaction's mechanism remains obscur, even if worthy results were obtained regarding complexes equilibrium which involves species formation even if a sort of semi-rational synthesis had been performed, starting from lacunary Keggin $[XM_{11}O_{39}]^{(12-n)-}$ or $[XM_9O_{34}]^{(14-n)-}$.

Synthesis of trilacunary polyoxometalates used below as construction units of new complex polyoxometalates with metals from block f, respectively with some organostanic fragments had been performed using components, by acidulation until pH 7-8 was reached, as shown in literature [10].

Synthesis of $K_{19}[(BiW_9O_{33})_4WO_2(H_2O)]_2Ce_3(H_2O)_8(Bi_4O_4)]\cdot 48H_2O$ (1)

Na_2WO_4 (3.3 g, 10 mmol) was dissolved in 30 ml of H_2O upon heating at 95 ^{o}C for 20 minutes. Then to the stirred solution was slowly added a solution of $Bi(NO_3)_3\cdot 5H_2O$ (0.196 g, 0.405 mmol) in 1.54 ml of HCl solution (6 M) and the pH was adjusted to 7.5 by adding KOH (2 M). The mixture was kept at 90 ^{o}C for an additional 20 minutes. Following filtration, was added $Ce(NO_3)_3\cdot 6H_2O$ (0.469 g, 1 mmol) dissolved in 1,8 ml of 1M CH_3COOH. Then we added a solution of KCl (4 g) in 15 mL water. A fine orange precipitate formed immediately, which was isolated by decantation and recrystallized from 5 ml of hot water. Orange needles formed

after a few days. These crystals were stable in the mother liquor but slowely decayed in air and the color was orange.

Anal. Calc.: K: 5.67; Bi: 12.75: W: 53.30; Ce: 3.20; H_2O: 6.59. Found: K: 5.38; Bi: 12.42: W: 53.52; Ce: 3.02; H_2O: 6.42. Yield: 74%.

Synthesis of $K_{15}[Ce_2(H_2O)_2(BiW_9O_{33})(W_5O_{18})_2].21H_2O$ (2)

$Bi(NO_3)_3 \cdot 6H_2O$ (0.43 g, 0.89 mmol) and $Ce(NO_3)_3 \cdot 6H_2O$ (0.67 g, 1.8 mmol) solids were dissolved in 4 mL aqueous 6M HCl with heating (solution 1). H_2WO_4 (4.2 g, 17 mmol) and KOH (2.5 g, 45 mmol) were solved in hot water (60 mL at 80 ^oC) (solution 2). Solution 1 was added to solution 2 with stirring at room temperature. During the addition the pH was kept at ca. 7 by aqueous KOH, and finally adjusted to ca. 7.5. The resulting cloudy solution was filtered and the filtrate was cooled to 5 ^oC in a beaker. After two days was obtained the pale orange microcrystals which were isolated by filtration and recrystallized from 20 ml of hot water. The final color was yellow-orange.

Anal. Calc.: K: 9.63; Bi: 3.43: W: 57.38; Ce: 4.43; H_2O: 6.80. Found: K: 9.00; Bi: 3.52: W: 57.82; Ce: 4.60; H_2O: 6.61. Yield: 60%.

RESULTS AND DISCUSSION

FT-IR spectroscopic results

In the FT-IR spectra of the first complex (Figure 1) can be observed the presence of valence bands characteristic for polyoxowolframate edifice, showing the stabilisation of the trilacunary polyoxoanion by cerium ions coordination [11]. Corresponding bands of valence vibrations of tricentric bonds W-O_c-W and W-O_e-W are splitted in two components. At lower frequencies can be observed the distorsion bands ν_{as} (O_i-P-O_i) and valence bands ν_{as} (W-O_i).

FT-IR data for (1) and (2)

IR frequency (cm^{-1})		Band assignments
Complex (1)	Complex (2)	
933 vs	934	ν_{as}(W=O_t)
871 sh	887 sh	ν_{as}(W-O_e-W)
831 vs	837 vs	ν_{as}(W-O_e-W)
796 sh	781 vs	ν_{as}(W-O_e-W)
700 vs	704 vs	ν_{as}(W-O_e-W)
582 m	581 m	δ(W-$O_{c,e}$-W)
544 m	538 m	δ(W-$O_{c,e}$-W)
486 m	482 m	δ(W-$O_{c,e}$-W)

Abbreviations: vs – very strong; m – medium; sh – shoulder; as – asymmetric deformation; ν - stretching; δ – bending; O_e - edge oxygen atom; O_c – corner oxygen atom; O_t – terminal oxygen atom.

In the IR spectra of the second compound (Figure 1) can also be observed the presence of valence bands characteristic for the polyoxowolframic edifice. The band corresponding to asymmetric vibrations of terminal bonds W-O_t expands and displaces towards bigger frequencies with 16 cm^{-1} suggesting.

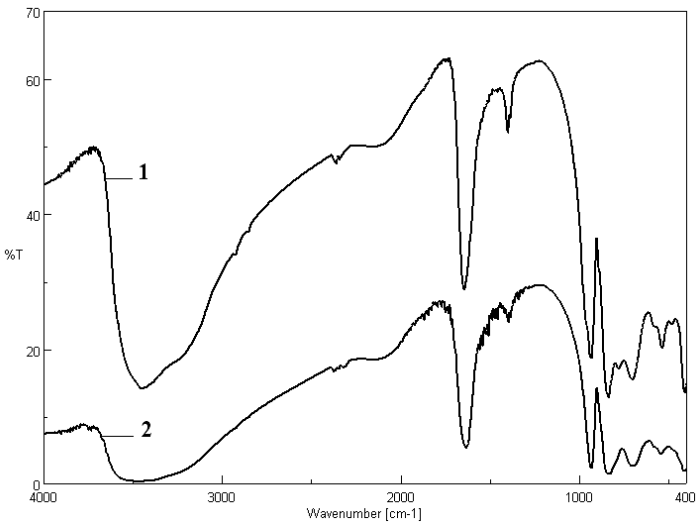

Fig. 1. FT-IR spectra of $K_{19}[(BiW_9O_{33})_4WO_2(H_2O)]_2Ce_3(H_2O)_8(Bi_4O_4)]\cdot 48H_2O$ **(1)** and $K_{15}[Ce_2(H_2O)_2(BiW_9O_{33})(W_5O_{18})_2]\cdot 21H_2O$ **(2)**

In both cerium complexes spectra apear a band situated at 727 cm^{-1} characteristic to sandwich type strucures. Next table presents the position of some important infrared bands and their assignments in case of the two complexes.

UV-VIS spectroscopic results

Electronic spectra of polyoxometalates show charge-transfer bands between 190-400 nm field (Figure 2) and crystallin field bands between 400-1200 nm (Figure 3).

UV electronic spectra of the both complexes (Figure 2) have very similar spectral features. These spectra contain an absorption band characteristic to a charge transfer $p_\pi(O_t) \rightarrow d_\pi(W)$ at ~200nm (194.5 nm for complex **(1)**, 195 nm for complex **(2)**). A charge transfer $p_\pi(O_{c,e}) \rightarrow d_\pi(W)$ is represented in the electronic spectra by two shoulders for each complex: at 244 and 289 nm for complex **(1)** and at 249.5 and 299.5 nm for complex **(2)**.

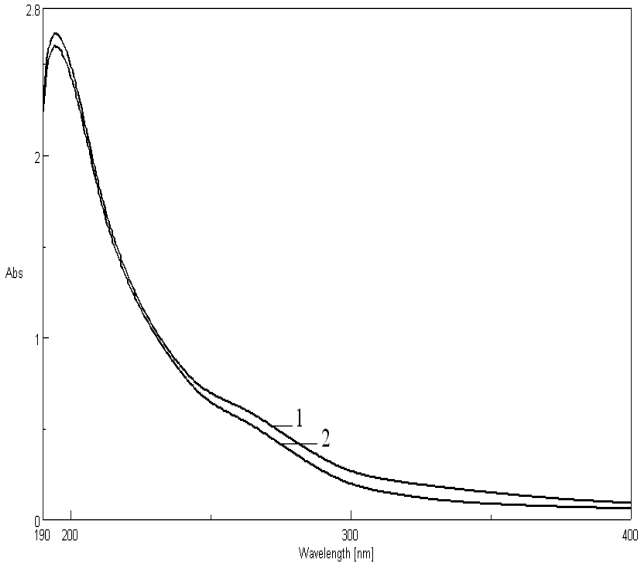

Fig. 2. UV spectra of the polyoxotungstates (**1**) and (**2**) in aqueous solution (10^{-5}M)

In the Vis spectra of the two compounds (Figure 3) a shoulder was observed at ~ 450 nm which was assigned to a metal-to-ligand charge transfer absorption [12]. An increased absorbance was also seen and assigned to a Ce(III)-ligand charge transfer [13].

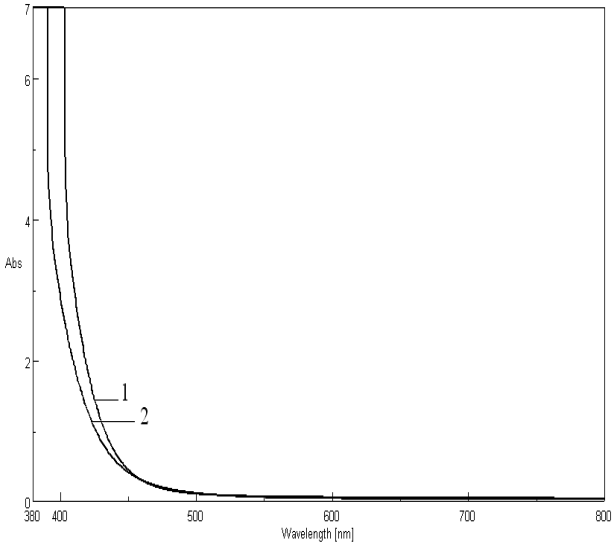

Fig. 3 Vis spectra of the polyoxotungstates (**1**) and (**2**) in aqueous solution (10^{-3}M)

CONCLUSIONS

This work reports the synthesis and characterization of two new Ce(III) complexes. The analysis of the compounds was based on elemental analysis, FT-IT and UV-Vis spectroscopy.

Elemental analysis is in good agreement with calculated values for proposed molecular formula of the complexes.

Both complexes show similar IR spectra indicating similar structures. Compared to the ligand, all of their characteristic stretching vibrations appear shifted in the 1000-700 cm^{-1} range, an indication of the Ce(III) coordination. The IR, UV and Vis spectra are characteristic of this type of polyoxometalates.

REFERENCES

[1] N. Belai, M.T. Pope, *Chem. Commun.,* 5760 (2005).

[2] Z. Kang, C.H.A. Tsang, Z. Zhang, M. Zhang, N. Wong, J.A. Zapien, Y. Shan, S.T. Lee, *J. Am. Chem. Soc.*, 17, 5326 (2007).

[3] A. Muller, F. Peters, M.T. Pope, D. Gatteschi, *Chem. Rev.*, 98, 239 (1998).

[4] M. Pope, A. Muller, "From Platonic Solids to Anti-Retroviral Activity", Kluwer Academic Publishers, Dordrecht, 1994.

[5] Y. Jeannin, *J. Cluster. Sci.,* 3, 55 (1992).

[6] A. Muller, F. Peters, M.T. Pope, D. Gatteschi, *Chem. Rev.,* 98, 239 (1998).

[7] K. C. Kim, M.T. Pope, *J. Chem. Soc. Dalton Trans.,* 986 (2001).

[8] H. Naruke, T. Yamase, *Bull. Soc. Jpn*., 74, 1289 (2001).

[9] H. Naruke, T. Yamase, *Bull. Soc. Jpn*., 75, 1275 (2002).

[10] G. Xue, J. Vaissermann, P. Gouzerh, *J. Cluster Sci.,* 3, 405 (2002).

[11] G. Socrates, "Infrared and Raman Characteristic, Group Frequencies: Tables and Charts", third edition, Wiley, Chichester, 2001.

[12] M.S. Masond, O.H. Abd El-Hamid, *Transit. Met. Chem.*, 14, 233 (1989).

[13] A.R. Tomsa, L. Muresan, A. Koutsodimou, P. Falaras, M. Rusu, *Polyhedron*, 22, 2901 (2003).

STUDIA UBB PHYSICA, Vol. 57(LVII), 1, 2012, pp. 93 - 99
(RECOMMENDED CITATION)

STRUCTURAL INVESTIGATION ON GD_2O_3– ZnO–B_2O_3 VITREOUS SYSTEM

D. SIMEDRU[1,*], R. STEFAN[2], E. CULEA[3], P. PASCUTA[3], M. BINDEA[2]

ABSTRACT. $xGd_2O_3 \cdot (100-x)[45ZnO \cdot 55B_2O_3]$ system was prepared within a range of $0 \le x \le 20$ mol%. XRD and FT-IR were used as tools for investigating the structure of prepared system. The XRD patterns revealed the vitreous nature of the samples for $x \le 15$ mol% and the overlapping of vitreous and crystalline phases for $x = 20$ mol%. The FT-IR spectra suggest a structure formed from $[BO_3]$ and $[BO_4]$ units of which proportion is varying depending on the gadolinium content. The A_r value representing the number of $[BO_4]$ units/$[BO_3]$ units ratio was take into consideration for reveling the deep changes in the structure of investigated glasses with the addition and increasing of gadolinium content. The subunit value of A_r ratio suggests that the number of $[BO_3]$ units is higher than the number of $[BO_4]$ units in all compositional range. The evolution of A_r value function of gadolinium ions concentration reveals the gradual increase within 0÷10 mol% compositional range of the number of $[BO_4]$ units with respect to $[BO_3]$ units. For $x = 15$ mol% the increasing of A_r value is attenuated. These results suggest that Gd_2O_3 is acting as a modifier of the investigated glass samples within 0÷10mol% compositional range. Over these concentrations its role in the investigated glass structure is changing.

Keyword: borate glasses; gadolinium ions; XRD; FT-IR; A_r value.

INTRODUCTION

Along the years, glasses were a subject of continuous investigation because of their unique properties such as: hardness, good strength, transparency and excellent corrosion resistance [1]. As it is well known, B_2O_3 is one of the most common glass formers with high bond strength, lower cation size, and small heat of fusion [2] which promoted the borate glasses between the most studies glasses. In

[1] INCDO-INOE 2000, Research Institute for Analytical Instrumentation, ICIA Cluj-Napoca Subsidiary, Cluj-Napoca, Romania
[2] Agricultural Science and Veterinary Medicine University,3-5 Calea Manastur, 400372 Cluj-Napoca, Romania
[3] Technical University, 400020 Cluj-Napoca, Romania
* dorina.simedru@icia.ro

glasses, the boron atom usually coordinates with either three or four oxygen atoms forming [BO_3] or [BO_4] structural units which can be arbitrarily combined to form different BxOy structural groups like boroxol ring, pentaborate, tetraborate, diborate groups.etc [3-5]. ZnO is a wide band gap semiconductor with applications in electronic and optical devices. If ZnO is properly doped, the material obtained can be used in applications such as transparent conducting electrodes, piezoelectric as well as ferroelectric layers [6, 7]. Glasses containing gadolinium ions are intensively studied due to their optical and magnetic properties which are of great interest in technical applications [8]. These properties are determined by the environment of Gd^{3+} ions, gadolinium concentration and its distribution in the host glass matrix and their micro-environment [3, 8]. Although the local structure of the gadolinium sites seems to be similar in different types of glasses, the correlation between the doping level and clustering depends on the glass type and composition [3, 8, 9].

Following the information above, the purpose of this study was to investigate the structure of $xGd_2O_3 \cdot (100\text{-}x)[45ZnO \cdot 55B_2O_3]$ glass system, within a range of $0 \le x \le 15$ mol%, by XRD and FT-IR spectroscopy in order to obtain structural information regarding $45ZnO \cdot 55B_2O_3$ glass matrix and the changes of its structure with the addition of gadolinium ions.

EXPERIMENTAL

$xGd_2O_3 \cdot (100\text{-}x)[45ZnO \cdot 55B_2O_3]$ system was prepared in $0 \le x \le 20$ mol% compositional range by mixing components of reagent grade purity (H_3BO_3, ZnO and Gd_2O_3) in suitable proportions to obtain the desired compositions. The melted mixtures (at 1250 °C) were quenched at room temperature by pouring onto stainless–steel plates.

The X-Ray diffraction measurements of the as prepared and heat treated samples were performed with a XRD-6000 Shimadzu diffractometer, with a mono-chromator of graphite for Cu-Ka radiation (λ = 1.54060 Å) at room temperature.

The FTIR absorption spectra were registered at room temperatures using a JASCO FTIR 4100 spectrometer. The IR absorption measurements were done using the KBr pellet technique. The FTIR spectra were recorded in the wavenumber range of 400– 4000 cm^{-1}, with a resolution of ~4 cm^{-1}.

RESULTS AND DISCUSSION

X-ray diffraction was used as an investigation tool for determining the vitreous or/and crystalline nature of the prepared samples. The XRD patterns of $xGd_2O_3 \cdot (100\text{-}x)[45ZnO \cdot 55B_2O_3]$ system with $0 \le x \le 20$ mol% are presented in Figure 1. As it can be observed, for $x \le 15$ mol%, the XRD patterns present a large

flat maximum characteristic to the vitreous structure. For x = 20 mol%, the large flat maximum is overlapped by several sharp maximums characteristic to the crystalline structure, which suggests that in this sample the vitreous and crystalline phases coexist. According to the database, the crystalline phase was identified as $GdBO_3$ (PDF#130483).

Due to the fact that this study was intended for investigating the vitreous structure of $xGd_2O_3 \cdot (100\text{-}x)[45ZnO \cdot 55B_2O_3]$ system, the sample with x = 20 mol% will be excluded from further studying.

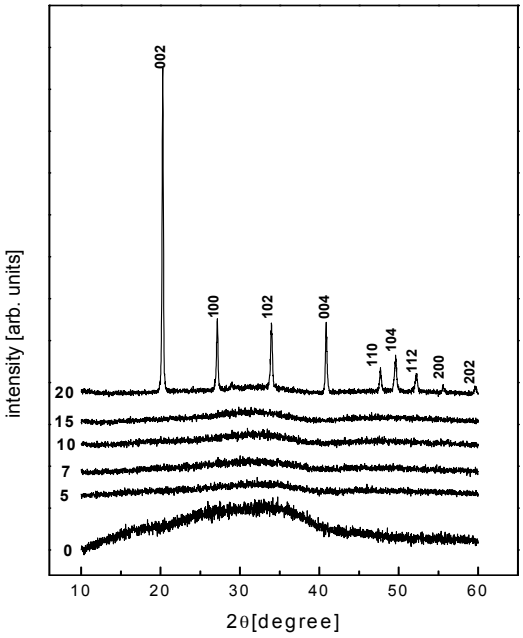

Fig. 1. The XRD patterns of $xGd_2O_3 \cdot (100\text{-}x)[45ZnO \cdot 55B_2O_3]$ system with $0 \leq x \leq 20$ mol%

The structure of $xGd_2O_3 \cdot (100\text{-}x)[45ZnO \cdot 55B_2O_3]$ glass system was investigated by FT-IR spectroscopy within a range of $0 \leq x \leq 15$ mol%. The experimental spectra are presented in Figure 2 and their assignments are summarized in Table 1. The assignments of the absorption bands were performed according to the theory of Croazier and Douglas [10] by comparing the spectra of glasses with the spectra of the analogous crystalline compounds of known structure [11].

The FTIR spectra of the investigated $45ZnO \cdot 55B_2O_3$ glass matrix shows five bands. Locations of the bands (with descriptions) are as follows: at ~688 cm^{-1} due to the bending vibrations of B—O—B bonds [12]; at ~875 cm^{-1} and ~1007 cm^{-1} due to B—O bonds stretching vibrations in $[BO_4]$ units from tri-, tetra- and penta-borate

groups [3] [13]; at ~1213 cm^{-1} due to B—O bonds asymmetric stretching vibrations in [BO_3] units from pyro- and ortho-borate groups [14] and at ~1345 cm^{-1} due to B—O stretch in [BO_3] units from varied types of borate groups [14].

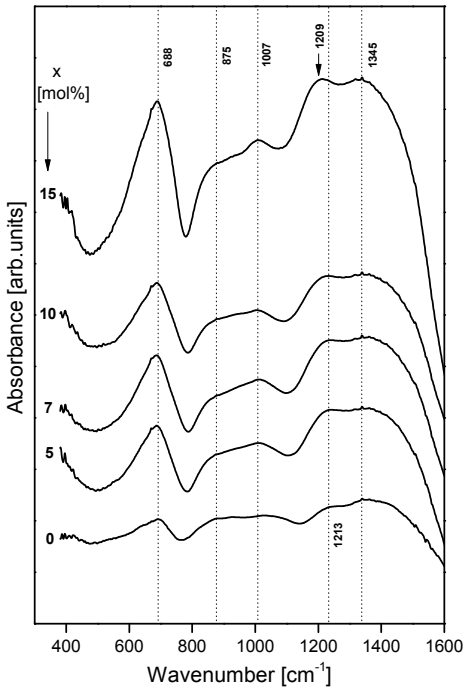

Fig. 2. FT – IR spectra of $xGd_2O_3 \cdot (100-x)[45ZnO \cdot 55B_2O_3]$ glass system with $0 \leq x \leq 15$ mol%

With the addition and increasing of Gd_2O_3, the intensity of the bands observed in $45ZnO \cdot 55B_2O_3$ glass matrix is increasing gradually.

The only deviation from the general aspect is the shifting of the band from ~1213 cm^{-1} to ~1209 cm^{-1} for x=15 mol%. This shift can be due to the altering of B—O bonds length from [BO_3] units into pyro- and ortho-borate groups prior to the formation of the crystalline phases.

As proved before, each B_2O_3 molecule needs one oxygen atom to be converted into two BO_4 tetrahedra [3]. In the structure of $45ZnO \cdot 55B_2O_3$ glass matrix that role of providing oxygen rests with ZnO. The addition of gadolinium ions is leading to an increase of all bands presented in the structure of the glass matrix, suggesting an increasing of the number of both [BO_4] and [BO_3] units. This suggests that the role of the glass modifier is take from this point forward by the Gd_2O_3.

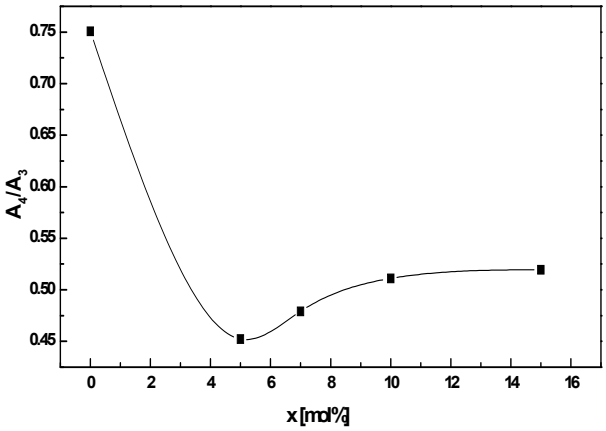

Fig. 3. Relative integrated absorption $A_r = A_4/A_3$ function of Gd_2O_3 content for $xGd_2O_3 \cdot (100\text{-}x)[45ZnO \cdot 55B_2O_3]$ glass system with $0 \le x \le 15$ mol%

In order to obtain more conclusive data regarding the changes that appear in the zinc-borate glass matrix with the increasing of gadolinium ions, the evolution of the triangular and tetrahedral borate units was studied by measuring the report $A_r=A_4/A_3$ where A_4 represents the vibrations involving $[BO_4]$ units and A_3 represents the vibrations involving $[BO_3]$ units. The evolution of A_r ratio function of concentration is presented in Figure 3. Its subunit value suggests that in all compositional range the number of $[BO_3]$ units is higher than the number of $[BO_4]$ units. The maximum value of A_r ratio (0.76) was obtained for the glass matrix suggesting that ZnO have a very important role in obtaining a vitreous structure by breaking the $[BO_3]$ units and modifying the borate network so that the number of $[BO_4]$ units is very close to the number of $[BO_3]$ units. The addition of gadolinium ions is decreasing the value of $[BO_4]$ units to its minimum value (0.46) which suggests that the first action of gadolinium ions is to act upon the $[BO_4]$ units, decreasing their number.

Table 1. Assignment of the FTIR bands of $xGd_2O_3 \cdot (100\text{-}x)[45ZnO \cdot 55B_2O_3]$ glass system with $0 \le x \le 15$ mol%

Wavenumber (cm^{-1})	**Assignment**
~688	B—O—B bonds bending vibrations
~875	B—O stretch in $[BO_4]$ units from tri-, tetra- and penta-borate groups
~1007	B—O stretch in $[BO_4]$ units from tri-, tetra- and penta-borate groups
~1213	B—O_{asymm} stretch in $[BO_3]$ units from pyro- and ortho-borate groups
~1345	B—O stretch in $[BO_3]$ units from varied types of borate groups

With the increasing of gadolinium ions content the ratio $[BO_4]$ units/$[BO_3]$ units is increasing gradually up to 10 mol% suggesting that the gadolinium ions are acting in this range, by increasing the number of $[BO_4]$ units with respect to $[BO_3]$ units and acting as a modifier of the glass structure. For x > 10 mol% the increasing is attenuated, suggesting a relative stability in the glass structure and that, for these concentrations, the role of glass modifier played earlier by the gadolinium ions is no longer valid.

CONCLUSIONS

Glasses from $xGd_2O_3 \cdot (100-x)[45ZnO \cdot 55B_2O_3]$ system were obtain within $0 \leq x \leq 15$ mol% compositional range. Their vitreous nature was confirmed by XRD. For higher concentration of gadolinium ions the XRD patterns shows that the vitreous and the crystalline phase coexists. The crystalline phase observed for x = 20 mol% identified as $GdBO_3$. The FT-IR spectra of the investigated glasses show the presence of $[BO_4]$ and $[BO_3]$ units in all compositional range. Their ratio was measured and evaluated function of gadolinium ions concentration. The subunit value of A_r ratio in all compositional range indicates that the number of $[BO_3]$ units is higher than the number of $[BO_4]$ units. Having in view the evolution of A_r ratio in all compositional range, it can be stated that for $x \leq 10$ mol%, the gadolinium ions is influencing the number of $[BO_4]$ units and $[BO_3]$ units by acting as a modifier of the glass network. Over these concentrations the influence of gadolinium ions on the number of $[BO_4]$ units and $[BO_3]$ units is significantly reduced which is proved by the attenuation of A_r ratio increase. It signifies that the gadolinium ions are starting to make their own network, which is proved by the appearance of $GdBO_3$ crystalline phase for x=20 mol%.

REFERENCES

[1]. M. Pal, B. Roy, M. Pal, J. Mod. Phys., 2, 1062 (2011)

[2]. C.R. Gautam, D. Kumar, O.M. Parkash, 2, Bull. Mater. Sci., 33,145 (2010)

[3]. Y.B. Saddeek, I.S. Yahia, K.A. Aly, W. Dobrowolski, Solid State Sci., 12, 1426 (2010)

[4]. Y.B. Saddek, Mater. Chem. Phys., 83, 222 (2004)

[5]. P. Pascuta, E. Culea, J Mater Sci: Mater Electron., 22, 1060 (2011)

[6]. S.M. Salem, E.M. Antar, A.G. Mostafa, S.M. Salem, S.A. El-badry, J. Mater. Sci., 46, 1295 (2011)

[7]. S. Fujihara, C. Sasaki, T. Kimura, Key Eng. Mater., 181, 109 (2000)

[8]. Y.B. Saddeek, I.S.Yahia, W. Dobrowolski, L. Kilanski, N. Romčević, M. Arciszewska, Optoel. Adv. Mat. – Rapid Commun., 3, 559 (2009)

[9]. S. Simon, R. Pop, V. Simon, M. Coldea, J. Non-Cryst. Solids, 331, 1 (2003)

[10]. D. Crozier, R.W. Douglas, Phys. Chem. Glasses, 6(6), 240 (1965)

[11]. E.A. Saad, F.H. ElBatal, A.M. Fayad, F.A. Moustafa, Silicon, 3, 85 (2011)

[12]. Y. Cheng, H. Xiao, W. Guo, W. Guo, Thermochimica Acta, 444, 173 (2006)

[13]. C.P. Varsamis, E.I. Kamitsos, G.D. Chryssikos, Solid State Ionics, 136–137, 1031 (2000)

[14]. R. Stefan, E. Culea, P. Pascuta, J. Non-Cryst. Solids, 358, 839 (2012)

STUDIA UBB PHYSICA, Vol. 57(LVII), 1, 2012, pp. 101 - 106
(RECOMMENDED CITATION)

STRUCTURAL AND EPR INVESTIGATIONS OF Mn-DOPED ZnO FINE CERAMICS

D. TOLOMAN[1,*], A. POPA[1], O. RAITA[1], M. STAN[1], A. DARABONT[1], L.M. GIURGIU[1] AND I. ARDELEAN[2]

ABSTRACT. Structural, morphological and EPR investigations on $Zn_{1-x}Mn_xO$ fine ceramics (x = 0.01 and 0.03) are reported. XRD studies reveal a wurzite-type structure, while the formation of $ZnMnO_3$ secondary phase was evidenced only for x = 0.03 sample. Both EPR spectra present a hyperfine structure specific to isolated Mn^{2+} ions and for the sample x = 0.03, a new quite broad resonance line arises, which could be attributed to a ferromagnetic phase.

Keywords: fine ceramics, XRD, EPR,

INTRODUCTION

Mn-doped ZnO semiconductors have become a topic of current interest since Dietl *et al.* [1] theoretically predicted the possibility of their room-temperature ferromagnetism. Soon after this work, several efforts were experimentally made [2–10] but the room-temperature ferromagnetic characteristics of these materials were reported in only a few works [2–4]. Notably, ferromagnetic behavior was found to appear only in the Mn-doped ZnO samples processed at low temperatures (T_{an}< 700 °C) [2, 4]. The question of whether the ferromagnetism of these materials originates from the contribution of some secondary phases as manganese oxides or from Mn^{2+} ions in Zn^{2+} lattice sites has been considered but remains unresolved [8–10]. This suggests that the properties of these materials are highly process-dependent and are influenced by the synthesis conditions, crystalline structure, magnetic clustering, doping degree and dimensionality.

New results are required to clarify this controversial situation and electron paramagnetic resonance (EPR) is expected to significantly contribute to their understanding. EPR spectroscopy is well known to be a powerful technique for

[1] National Institute for R&D of Isotopic and Molecular Technologies 400293 Cluj-Napoca, Romania
[2] Faculty of Physics, "Babes-Bolyai" University, 400084 Cluj-Napoca, Romania
* dana.toloman@itim-cj.ro

studying microscopic details of novel multifunctional materials. This spectroscopy is an effective tool to investigate the origin and nature of ferromagnetism observed in diluted magnetic semiconductors (DMS) [11]. For characterization of a ZnO system doped with TM ions (TM = Mn, Fe, Co), EPR spectroscopy offers some interesting advantages over the other methods: it has a higher sensitivity which is required for investigation of magnetic inhomogenity [12], its selectivity to the microscopic structure of the doping ion [13] and its resonant character. These, allow one to easily eliminate undesired contributions and effects of phase inclusions [14]. There are some EPR investigations of micro- and nanostructured $Zn_{1-x}TM_xO$ compounds referring, in principle to the local symmetry and local properties in the vicinity of TM impurities [15], the detection of the ferromagnetic ordering as well as the existence of other magnetic species [16, 17], the incorporation degree of TM ions [18], the influence of the TM concentration on EPR spectra [19] and the identification of paramagnetic and ferromagnetic phases [20].

We present here the results of such an EPR study of $Zn_{1-x}Mn_xO$ (x = 0.01 and 0.03) fine ceramics in order to evidence the magnetic behavior of the samples.

EXPERIMENTAL

A series of ceramic samples of Mn-doped ZnO, having a general formula $Zn_{1-x}Mn_xO$ (x = 0.01 and 0.03), were prepared. Stoichiometric amounts of zinc acetate dehydrate – Zn(CH3COO)2·2H2O (98%) and manganese (II) nitrate tetrahydrate – Mn(NO3)2·4H2O (98.5%), were dissolved in distilled water and stirred until a homogeneous solution was obtained. The reaction mixture was slowly evaporated until dry and the obtained solid mass was decomposed at 250 °C in air. The temperature was gradually raised over 2–3 days. After heat treatment, this mass precursor was ground to give fine powder. Fractions of the obtained powders were calcinated at 600 °C for 2 h in air.

X-ray diffraction measurement was made using high resolution Bruker D8 Advance diffractometer with Cu x- ray tube and incident beam Ge (111) monocromator (λ= 1.54056Å).

Scanning electron microscopy (SEM) was collected at room temperature using a JEOL7000F microscope with a specific resolution of 1.2 nm.

EPR measurements of powder samples were carried out on a Bruker E-500 ELEXSYS X-band spectrometer at variable temperatures. The spectra processing was performed by Bruker Xepr software. The simulations were performed using Bruker XSophe program.

RESULTS AND DISCUSSION

X-ray powder diffraction (XRD) was used to analyze the structural properties of the materials and to identify the phase and the purity of all the samples. Fig. 1 shows the X-ray powder diffraction pattern recorded for the samples with x = 0.01 and 0.03. Results of XRD measurements indicate that the diffractograme for x = 0.01 sample can be indexed to a hexagonal wurzite structure as ZnO. No trace of manganese metal, oxides or any binary zinc manganese phase could be observed. Besides the diffraction peaks from ZnO wurzite structure, weak additional peaks from $ZnMnO_3$ impurity phase have been observed for x = 0.03 sample.

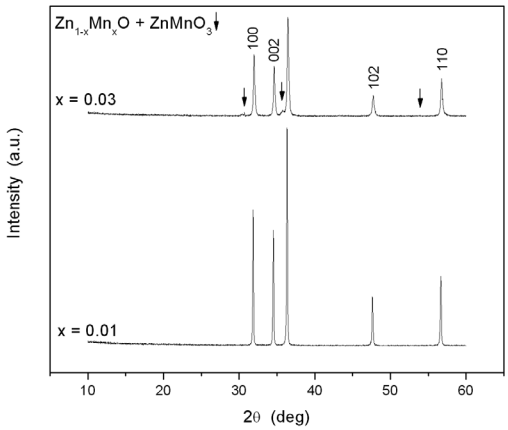

Fig. 1. Powder x-ray diffraction patterns of $Zn_{1-x}Mn_xO$ (x = 0.01 and 0.03)

The particle's size and morphology were characterized by SEM microscopy. The images of $Zn_{1-x}Mn_xO$ (x = 0.01 and 0.03 treated in air atmosphere) are shown in Fig. 2. It could be observed that the individual particles have almost spherical shapes with mean sizes of 110 and 140 nm for x = 0.01 and x = 0.03 samples, respectively. However, an inherent agglomeration of the individual particles was also noticed.

(a) (b)

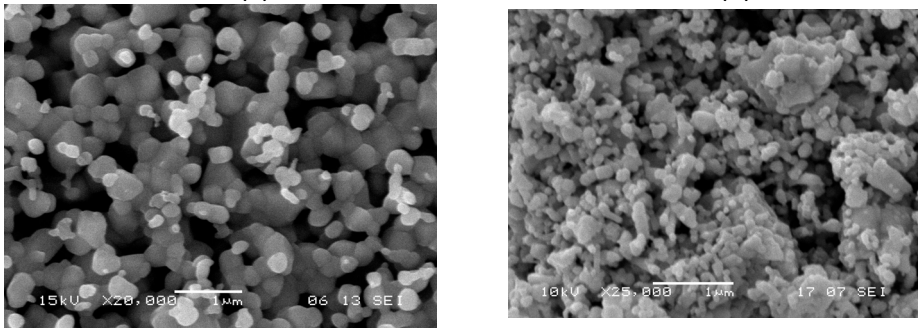

Fig. 2. SEM images of $Zn_{1-x}Mn_xO$ for a) x = 0.01 and b) x = 0.03

For both samples, the EPR spectra (Fig.3) present the fine and hyperfine lines characteristic to the isolated Mn^{2+} ions, which could be analyzed by the following spin Hamiltonian:

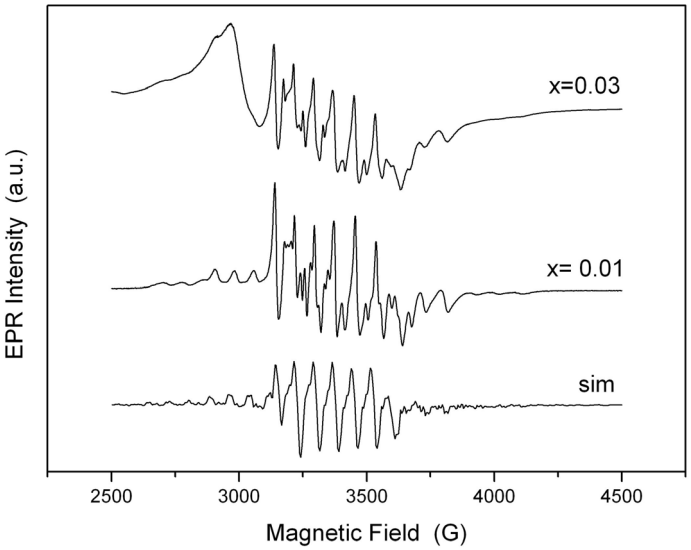

Fig. 3. EPR spectra of $Zn_{1-x}Mn_xO$ with x = 0.01 and x = 0.03 and the simulated spectrum (sim) of Mn^{2+} ions with S=5/2 and I=5/2 in ZnO crystal lattice

$$H = g\mu_b HS + D\left[S_z^2 - \frac{1}{3}S(S+1)\right] + ASI \quad (1)$$

where the first term describes the Zeeman interaction, the second term refers to the axial zero-field splitting due to hexagonal symmetry of the wurzite ZnO and the third term describes the hyperfine interaction between the electron and nuclear spin of manganese ions. Considering the experimental EPR spectrum of x = 0.01 sample, the best simulation is achieved by using the following spin Hamiltonian parameters: A = - 75 G, D = - 220 G and g = 2.01. These values are in accordance with those reported for the Mn^{2+} ions doped in single crystals (A = - 81 G, D = - 232 G, and g = 2.0016) [21,22]. Therefore, the complex resonance spectra evidenced for both samples arises from the paramagnetic moments of isolated Mn^{2+} ions substitutionaly incorporated in the ZnO crystal lattice. Besides the EPR spectrum centered at g = 2.01, in the x = 0.03 sample was evidenced at lower field a quite broad resonance line which could be attributed to ferromagnetic phase in material (see Fig. 3). Similar spectra to those outlined by us were observed by Jayakumar et al [5]. For a better explanation of the origin of this line we plan further EPR investigations.

CONCLUSION

In summary, we have reported a structural, morphological and EPR study on $Zn_{1-x}Mn_xO$ fine ceramics with x = 0.01 and 0.03. From XRD characterization results that both samples presents peaks which are specific to ZnO wurzite structure. Besides these peaks, weak additional peaks due to $ZnMnO_3$ have been observed for x = 0.03. SEM measurements show that the particles size increases with the concentration of the dopant. From the analysis of EPR spectra results that in the both samples, the Mn^{2+} ions are isolated and substitutionally incorporated in the host lattice. For x = 0.03 sample, besides the hyperfine lines characteristic of Mn^{2+} ions, appears at lower field a broad line which could be assigned to the ferromagnetic phase.

ACKNOWLEDGMENT

At National Institute for Research and Development of Isotopic and Molecular Technologies this work was supported by CNCSIS-UEFISCSU, project number PNII-IDEI Nr. 4/2010, cod ID-106.

REFERENCES

[1]. T. Dietl, H. Ohno, F. Matsukura, J. Clibert, D. Ferrand, *Science*, 287, 1019 (2000).

[2]. M.A. Garcia, *Phys. Rev. Lett.* 94, 217206 (2005).

[3]. J.B. Wang, G.J. Huang, X.L. Zhong, L.Z. Sun, Y.C. Zhou, *Appl. Phys. Lett.* 88, 252502 (2006).

[4]. C.J. Cong, L. Liao, Q. Y. Liu, J. C. Li, K.L. Zhang, *Nanotechnology* 17, 1520 (2006).

[5]. O.D. Jayakumar, H.G. Salunke, R.M. Kadam, M. Mohapatra, G. Yaswant, and S.K. Kulshreshtha, *Nanotechnology* 17, 1278 (2006).

[6]. J.B. Wang, H.M. Zhong, Z.F. Li, W. Lu, *J. Appl. Phys*. 97, 086105 (2005).

[7]. E. Chikoidze, H.J. Von Bardeleben, Y. Dumont, P. Galtier, J.L. Cantin, *J. Appl. Phys.* 97, 10D316 (2005).

[8]. A.B. Mahmound, H.J. Von Bardeleben, J.L. Cantin, A. Mauger, E. Chikoidze, Y. Dumont, *Phys. Rev. B* 74, 115203 (2006).

[9]. H.Y. Xu, Y.C. Liu, C.S. Xu, Y.X. Liu, C.L. Shao, R. Mu, *J. Chem. Phys.* 124, 074707 (2006).

[10]. L.W. Yang, X.L. Wu, G.S. Huang, T. Qiu, and Y.M. Yang, *J. Appl. Phys.* 97, 014308 (2005).

[11]. G. Lawes, A.S. Risbud, A.P. Ramirez, R. Seshadriet, *Phys. Rev. B* 71, 045201 (2005).

[12]. M. Bouloudenine, N. Viart, S. Colis, J. Kortus, A. Dinia, *Appl. Phys. Lett.* 87, 052501 (2005).

[13]. J. Hays, K.M. Reddy, N.Y. Graces, M.H. Engelgard, V. Shutthanandan, M. Luo, C. Xu, N.C. Giles, C. Wang, S. Thevuthasan, A. Punnoose, *J. Phys.: Condens Matter* 19, 266203 (2007).

[14]. J.B. Wang, G.J. Huang, X.L. Zhong, L.Z. Sun, *Appl. Phys. Lett.* 88, 252502 (2006).

[15]. B.C. Cheng, Y.H. Xiao, G.S. Wu, L.D. Zhang, *Appl. Phys. Lett.* 84, 416 (2004)

[16]. C. Bundesmann, N. Ashkenov, M. Schubert, D. Spermann, T. Butz, *Appl. Phys. Lett.* 8, 1974 (2003).

[17]. K. Gopinadhan, D.K. Pandya, S.C. Kashyap, S. Chaudhary, *J. Appl. Phys.* 99, 126106 (2006).

[18]. K. Ueda Tabata, T. Kawai, *Appl. Phys. Lett.* 79, 988 (2001).

[19]. H.T. Lin, T.S. Chin, J.C. Shih, *Appl. Phys. Lett.* 85, 621 (2004).

[20]. D.A. Schwartz, D.R. Gamelin, *Adv. Mater.* 16, 2115 (2004).

[21]. P.B. Dorain, *Phys. Rev.* 112, 1058 (1958).

[22]. A. Hausmann, H. Hupertz, *J. Phys. Chem. Solids* 29, 1369 (1968).